2-9-2010

Numerical study of solder joint failure under fast loading conditions

Kiranmaye Aluru

Kiranmaye Aluru
Candidate

Mechanical Engineering Department
Department

This thesis is approved, and it is acceptable in quality and form for publication on microfilm:

Approved by the Thesis Committee:

, Chairperson

Accepted:

Dean, Graduate School

Date

NUMERICAL STUDY OF SOLDER JOINT FAILURE UNDER FAST LOADING CONDITIONS

BY

KIRANMAYE ALURU

B. Tech., Mechanical Engineering, Jawaharlal Nehru Technological University, India, May 2006

THESIS

Submitted in Partial Fulfillment of the
Requirements for the Degree of

Master of Science
Mechanical Engineering

The University of New Mexico
Albuquerque, New Mexico

December, 2009

DEDICATION

This thesis is dedicated to my beloved parents

Venkata Bhaskara Rao Aluru and Bala Tripura Sundari Aluru

ACKNOWLEDGEMENTS

First and foremost, I would like to express my deepest gratitude to Dr.Yu-Lin Shen, my graduate advisor, who was instrumental in my graduate career. He introduced me to this exciting field of Materials science, provided technical guidance, necessary financial support and overlooked my mistakes. I want to thank him for his continuous support and constant encouragement through the years of study and research. I am thankful for his patience. His guidance and professional style will remain with me as I continue my career.

Probably just the pictures in this thesis will catch the eye of the reader. Abaqus is excellent software to perform numerical modeling. While I implemented programs for calculating displacement and reaction force and thus different stress-strain curves. I am grateful to Dr. Shen for introducing me to Abaqus software.

I would like to take this opportunity to thank Dr. Zayd Leseman and Dr. Claudia Luhrs for serving on my advisory committee and for providing their professional expertise.

I would like to thank Dr. Ebrahimi, Graduate Program Director, Mechanical Engineering Department, University of New Mexico, for his support and guidance throughout my graduate career.

Most importantly, my parents deserve much credit for my success who sacrificed their personal fears of being alone and to be away from their daughter to see me graduate. I thank my stars for blessing me with the “Best Parents” in the world. I am very much thankful to my sister Shanthi and her family for their support and encouragement in

everything that I wish in my life. I want to thank her for being the best sister I could ever hope for!

I extend my gratitude to my grandmother for her constant encouragement, unconditional support and genuine love which is the greatest gift of all. I can't imagine my life without her being an important part of it.

I am also very much thankful to all my other family members and relatives for their support and love to reach this point in my life.

Friends are the most important ingredients in the recipe of life. I am grateful to Guanlin Tang for her help with Abaqus software when I was learning software prior to starting my actual thesis work. She is a good friend of mine. In addition, I am also grateful to Prathyusha, Prasanna, Maheshwar Kashamolla, and many more for their help, support and friendship.

Last but not the least; I would like to thank God for being there for me in every step that I took to be here far far away from my home. I want to thank God for everything that I am blessed with in my Life and for giving me this opportunity to learn and answering my prayers at all times.

NUMERICAL STUDY OF SOLDER JOINT FAILURE UNDER FAST LOADING CONDITIONS

BY

KIRANMAYE ALURU

ABSTRACT OF THESIS

Submitted in Partial Fulfillment of the
Requirements for the Degree of

Master of Science
Mechanical Engineering

The University of New Mexico
Albuquerque, New Mexico

December, 2009

NUMERICAL STUDY OF SOLDER JOINT FAILURE UNDER FAST LOADING CONDITIONS

BY

KIRANMAYE ALURU
B. Tech., Mechanical Engineering, Jawaharlal Nehru Technological University, 2006
M.S. Mechanical Engineering, University of New Mexico, 2009

ABSTRACT

A numerical study was undertaken to investigate the solder joint failure under fast loading conditions. The finite element model assumes a lap-shear testing configuration, where the solder joint is bonded to two copper substrates. A progressive ductile damage model was incorporated into the rate-dependent constitutive response of the Sn (tin)-Ag (silver)-Cu (copper) solder alloy, resulting in the capability of simulating damage evolution leading to eventual failure through crack formation. Attention is devoted to deformation under relative high strain rates (1-100 s^{-1}), mimicking those frequently encountered in drop and impact loading of the solder points. The effects of applied strain rate and loading mode on the overall ductility and failure pattern were specifically investigated. It was found that the solder joint can actually become more ductile as the applied strain rate increases, which is due to the alteration of the crack path. Failure of the solder is very sensitive to the deformation mode, with a superimposed tension/compression on shear easily changing the crack path and tending to reduce the solder joint ductility. In addition, cyclic shearing resulted in different failure patterns from those of monotonic loading. The two fatigue cracks, one at (or very close to) each

interface, have both grown to a significant length with one responsible for final failure of the joint.

TABLE OF CONTENTS

LIST OF FIGURES

LIST OF TABLES

CHAPTER 1 INTRODUCTION

A process by which metals may be joined via a molten metallic adhesive (the solder) which on solidification forms strong bonds (usually intermetallic compounds) with the adherents is called soldering. It is the preferred method for attaching microelectronic components to printed circuit boards (PCBs) or chips to substrates [1]. Solders have the great virtue of enabling low-temperature joining of metallic conductors to establish low-resistance ohmic electrical performance at all packaging levels for making permanent interconnections. Solder joints also provide mechanical support of components [2]. When either of the functions is out of service, the solder joint is considered to have failed, which can often threaten a shutdown of the whole electronic system [3]. Figure 1.1 shows a schematic of solder joints connecting a silicon chip to a circuit board.

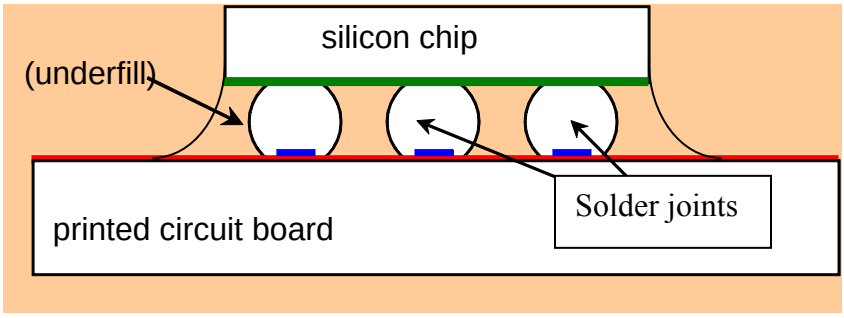

Fig. 1.1 Schematic diagram of a solder electronic package. (In some cases a polymer-based "underfill" material is applied for the purpose of improving solder joint reliability.)

The Sn (tin)-Ag (silver)-Cu (copper) alloy is one of the most promising systems to replace Pb (lead)-bearing solder. It is superior to other Sn-rich alloys because of its

superior mechanical properties, including good yield strength, reasonable ductility, good wetting properties, and relatively low melting temperature, among others [7-10].

Thermo-mechanical stress was an important factor affecting solder reliability [4]. Stresses in solder joints are generated because of the thermal expansion mismatch between the components they connect, as a consequence of cyclic thermal excursions associated with operation and Joule heat. Damage is caused not only by cyclic deformation but also by creep due to the inherent low melting point of solder material. The growth of intermetallic compounds during reflow and high temperature storage can strongly affect the subsequent solder deformability and strength which may result in mechanical failure of the joint [6]. Another reliability concern for future high density microelectronic packaging and power electronic packaging is electromigration in solder joints [5].

In recent years a particular problem, namely failure of solder due to drop, impact and vibration of the components, has emerged to be an important reliability threat to the industry [22-32]. This is different from the traditional thermo-mechanical fatigue problem because the loading rate involved in drop, impact and vibration can be several orders of magnitude faster than the loading rate resulting from thermal cycling. This thesis research is devoted to numerical modeling of failure of solder joint under the fast loading conditions.

The current study is an outgrowth of a previous research [11], which employed finite element modeling to study deformation inside the solder joint during the commonly adopted lap-shear tests [6,12-21]. In Ref. [11], the focus was on using the plastic strain field to explain the fatigue crack path which is frequently observed to be close to, but not right at, the interface between the solder alloy and the bonding material. An example is shown in Fig. 1.2, where the dominant failure path in the Sn-Pb solder is near the interface with the Cu substrate under the relatively low rate cycling shearing. Fracture is entirely within solder, outside of thin intermetallic layer between the solder and copper. Using the simple rate-independent plasticity model for the solder, the evolution of the equivalent plastic strain pattern over the cycles was found to be able to explain the experimental observation [11].

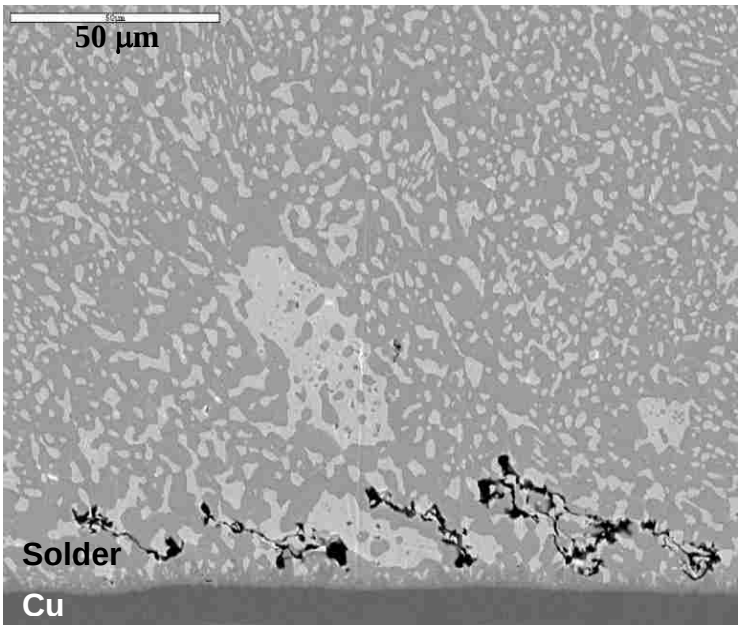

(a)

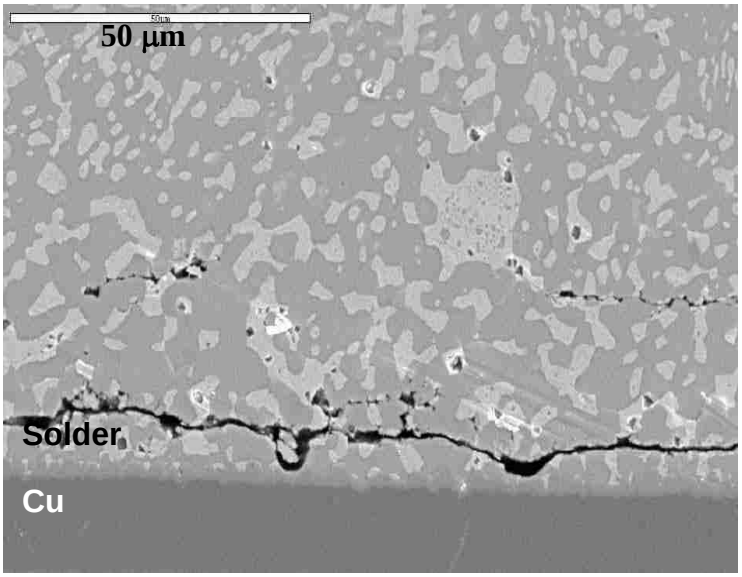

(b)

Fig 1.2 Scanning electron micrographs of fracture patterns in the eutectic Sn-Pb solder bonded to the Cu substrates in a lap-shear set up, after being deformed at room temperature for (a) 500 cycles at 1 Hz with the peak nominal shear strain of 0.08, and (b) 120 cycles at 0.002 Hz with the peak nominal shear strain of 0.10 [11].

In the current study, extensions of the previous numerical model are made to incorporate the following features:

- The rate-dependent (elastic-viscoplastic) response of a Sn-Ag-Cu solder is used in the model to specifically address the loading rate effect, without the incorporation of any microstructural features.
- A ductile damage model is incorporated, which, in conjunction with the element removal process in the explicit finite element analysis, is capable of simulating direct failure of the solder (rather than deformation only).
- The lap-shear model can now include a superimposed tensile and compressive deformation, so their effects on the cracking pattern can be examined.
- Attention of this study is directed to high-rate deformation, for the purpose of laying the foundation for developing predictive modeling capabilities to address the increasing concern of drop and impact reliability.

Chapter 2 Numerical Model

The computational model is schematically shown in Fig. 2.1, with the solder joint bonded to two copper (Cu) blocks (also termed substrates in this thesis). During deformation the x-direction movement of the far left edge of the upper Cu is forbidden, but movement in the y-direction is allowed except that the upper-left corner of the upper copper is totally fixed. The top boundary of the upper Cu block is also fixed in the y-direction. Deformation of the structure is applied by imposing a constant velocity on the boundary of the lower Cu substrate. The right and bottom boundaries of the lower substrate are constrained to remain vertical and horizontal, respectively, during deformation. The arrows in Fig. 2.1 denote a specific loading mode leading to a nominal shear and nominal tension deformation of the solder joint. In this study a possible tensile or compressive loading is also considered, which is achieved by applying a constant velocity in the y-direction on the bottom boundary of the substrate.

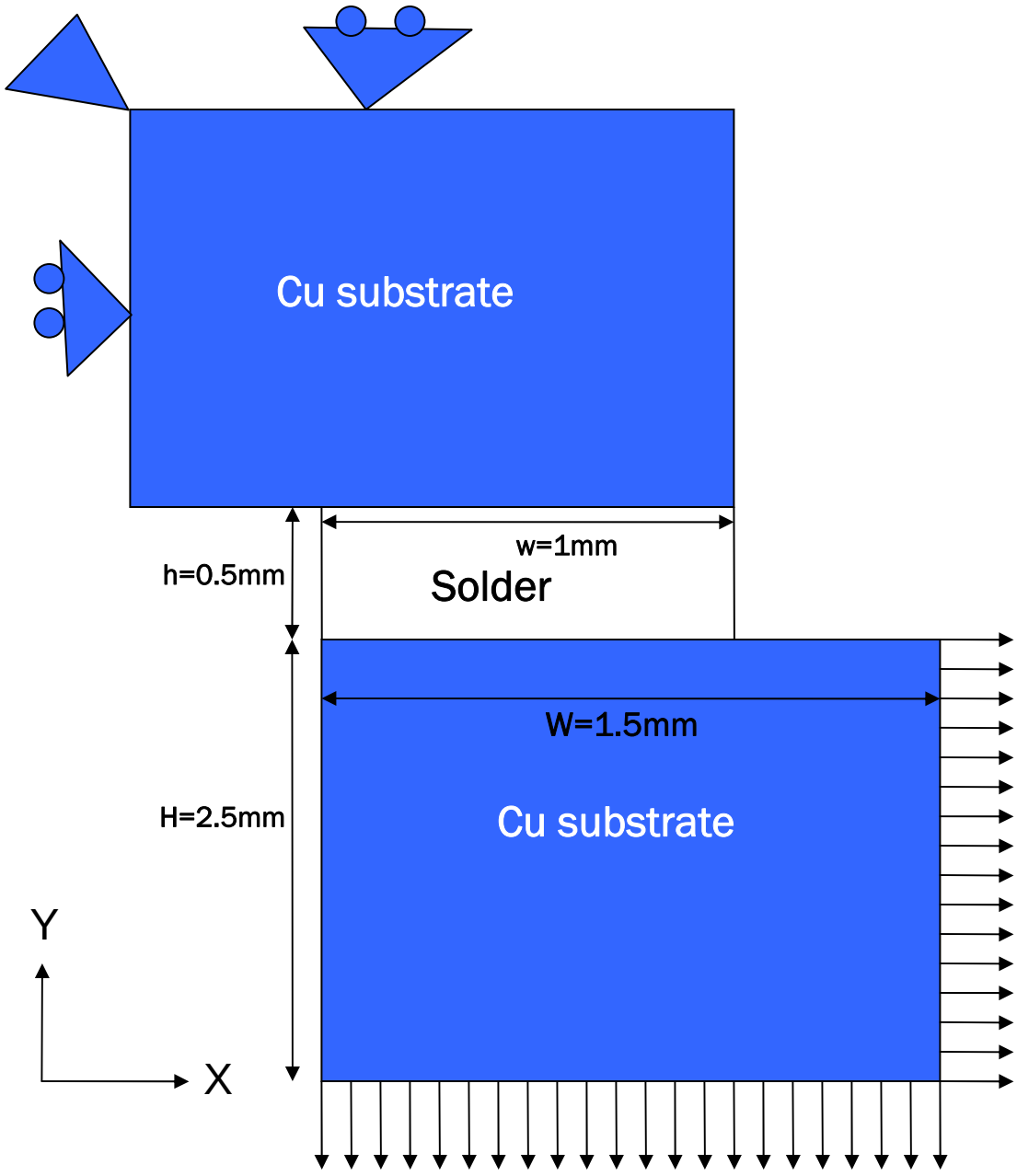

Fig. 2.1 Schematic of solder-substrate assembly used in the finite element analysis (drawing not to scale).

The solder joint has a width w = 1.0 mm and height h = 500 μm. Each Cu substrate has a width W = 1.5 mm and height H = 2.5 mm. At each interface between the solder and the

copper there is a very thin (5 μm) intermetallic layer included in the model (not shown in Fig. 2.1). The solder/intermetallic structure was discretized into 5000 four-noded linear elements. Each Cu substrate was dicretized into 2400 elements. The total number of elements considered in this model is 9800. The calculations were based on the plane strain condition, which effectively simulates the nominal simple shearing mode of the solder. [20]

In the model, Cu is taken to be isotropic linear elastic, with a Young's modulus (E) of 114 GPa, Poisson's ratio (ν) of 0.31 and density of 8930 kg/m^3. The solder, taken to be a Sn-1.0Ag-0.1Cu alloy [33], is assumed to be an isotropic elastic-viscoplastic material with isotropic hardening. The Young's modulus (E) and Poisson's ratio (ν) of the solder are 48GPa and 0.36, respectively, and the yield strength is taken from the experimental stress-strain curves for different strain rates. The density is 5760 kg/m^3.

The intermetallic layer (Cu_6Sn_5) is isotropic linear elastic with Young's modulus (E) of 85.5GPa and Poisson's ratio (ν) of 0.28, and density is 8280 kg/m^3. The explicit solver of the finite element program ABAQUS was employed in the calculations.

The elastic response follows the generalized Hooke's law. Plastic yielding of Al follows the von Mises criterion and the incremental flow theory [34]. In terms of the principal stresses σ_1, σ_2 andσ_3, the von Mises effective stress is expressed as

$$\sigma_e = \frac{1}{\sqrt{2}}\left[(\sigma_1-\sigma_2)^2+(\sigma_2-\sigma_3)^2+(\sigma_3-\sigma_1)^2\right]^{\frac{1}{2}} \qquad (1)$$

Yielding commences when the magnitude of σ_e reaches σ_y, the yield strength of the metal under uniaxial loading. Note $\sigma_e = \sqrt{3J_2} = \sqrt{\frac{3}{2}\sigma'_{ij}\sigma'_{ij}}$, where J_2 is the second invariant of

the deviatoric stress tensor σ'_{ij} with $\sigma'_{ij} = \sigma_{ij} - \frac{1}{3}\delta_{ij}\sigma_{kk}$ (σ_{ij} represents the general stress components and δ_{ij} is the Kronecker delta). Here the indicial notation with the summation convention used in standard continuum mechanics is followed. Upon yielding, the total strain of an elastic-plastic material, ε_{ij}, is the sum of the elastic part ε^e_{ij} and the plastic part ε^p_{ij}. The incremental flow theory relates the increment of plastic deformation to stress in the functional form of

$$\sigma_e = f(\int d\bar{\varepsilon}^p), \tag{2}$$

where *f* is the strain hardening function and $d\bar{\varepsilon}^p$, the effective plastic strain increment, is

$$d\bar{\varepsilon}^p = \sqrt{\frac{2}{3}d\varepsilon^p_{ij}d\varepsilon^p_{ij}} = \frac{\sqrt{2}}{3}\left[(d\varepsilon_1 - d\varepsilon_2)^2 + (d\varepsilon_2 - d\varepsilon_3)^2 + (d\varepsilon_3 - d\varepsilon_1)^2\right]^{\frac{1}{2}}, \tag{3}$$

where $d\varepsilon_1$, $d\varepsilon_2$ and $d\varepsilon_3$ are the principal plastic strain increments. After the material has experienced a plastic deformation history, the equivalent plastic strain (or effective plastic strain) is then

$$\bar{\varepsilon}^p = \int_0^t \frac{d\bar{\varepsilon}^p}{dt}\, dt \tag{4}$$

where t is the time history.

As described above the Sn-Ag-Cu solder is assumed to follow the viscoplastic response. It is based on the static plastic stress-strain relation in Eq. (2), with a scaling parameter to quantify the "strain rate hardening" effect:

$$\sigma_e = f(\int d\bar{\varepsilon}^p) \cdot R(\frac{d\bar{\varepsilon}^p}{dt}), \tag{5}$$

where f (as a function of plastic strain) is the static plastic stress-strain response, and R, a function of plastic strain rate $\frac{d\bar{\varepsilon}^p}{dt}$, defines the ratio of flow stress at nonzero strain rate to the static flow stress (where R =1.0). The rate-dependent experimental stress-strain curves in Fig. 2.2 are used to construct the material model for the simulation following Eq. (5).

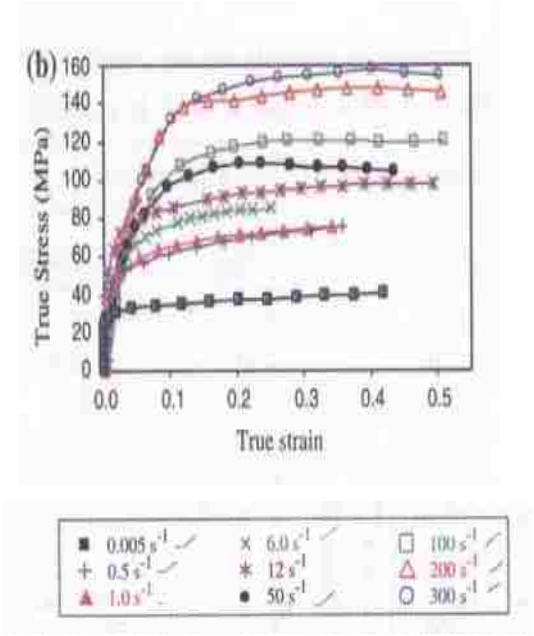

Fig 2.2 Rate-dependent experimental stress-strain curves [33]

To simulate failure of the solder alloy, a progressive ductile damage model is used. Figure 2.3 schematically shows a characteristic stress-strain curve undergoing damage. The solid curve represents the damaged response, and the dashed curve shows the stress-strain curve in the absence of damage. The damage manifests itself in two aspects: softening of the plastic flow stress and degradation of the elasticity. At any time during the damage process, the stress tensor in the material is given by the scalar damage equation

$$\sigma = (1 - D)\bar{\sigma} \tag{6}$$

where D is the damage variable and $\bar{\sigma}$ is the effective stress tensor (undamaged) in the current time increment. A material point loses its load-carrying capability when its D reaches unity. The particular element will then be removed from the mesh and a "crack" (or "void") is thus initiated.

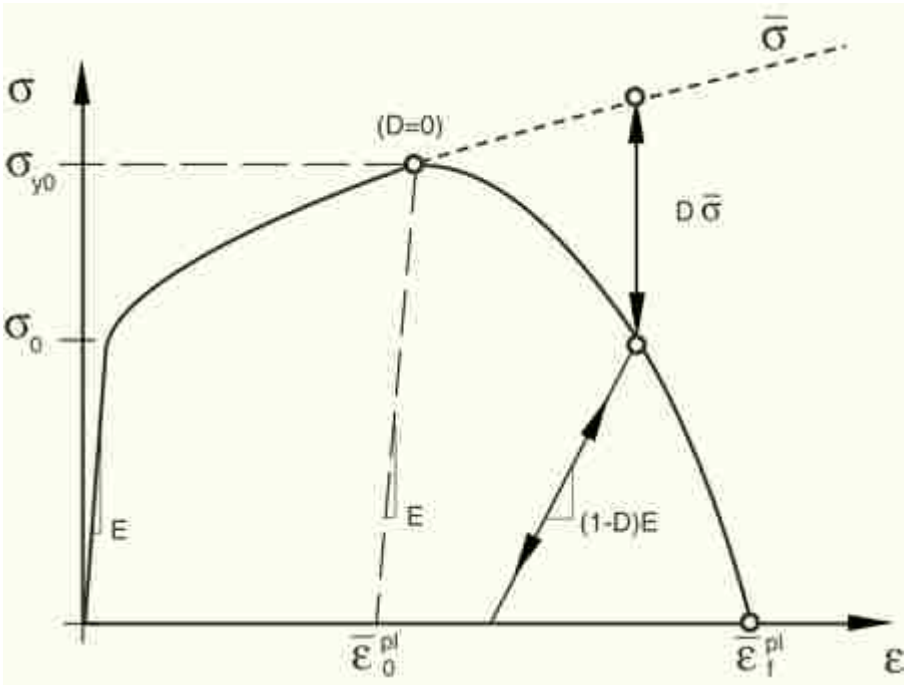

Fig.2.3 Representative stress-strain response with progressive damage.

In Fig. 2.3 σ_{y0} and $\bar{\varepsilon}_0^{pl}$ are the plastic flow stress and equivalent plastic strain at the onset of damage, and $\bar{\varepsilon}_f^{pl}$ is the equivalent plastic strain at failure (at D = 1). In general $\bar{\varepsilon}_0^{pl}$ can be made a function of η and $\bar{\varepsilon}^p$, where $\eta = \dfrac{\sigma_{hyd}}{\sigma_e}$ the stress triaxiality is and $\bar{\varepsilon}^p$

is the equivalent plastic strain defined in Eq. (4). Here $\sigma_{hyd} = \frac{1}{3}(\sigma_1 + \sigma_2 + \sigma_3)$ is the hydrostatic stress and σ_e is the von Mises effective stress. In the present work only the equivalent plastic strain value is specified for $\bar{\varepsilon}_0^{pl}$, due to the lack of systematic experimental data that may be used for defining the functional form. Upon initiation of damage, strain softening of the material commences, leading to strain localization which shows a strong mesh dependency. To alleviate the mesh dependency, a characteristic length is utilized in the model so the softening of the constitutive law is expressed as a stress-displacement relation [35], as detailed below.

The damage evolution law is specified in terms of "equivalent plastic displacement, " $\bar{u}^p$, through the relation

$$\bar{u}^p = L\bar{\varepsilon}^p \qquad (7)$$

where L is the characteristic length defined as the square root of the integration point area in each finite element. Before damage initiation $\bar{u}^p = 0$; after damage initiation Eq. (7) starts to take effect. Failure (and removal) of the element occurs when $\bar{u}^p$ reaches the specified failure value, $\bar{u}_f^p$. The evolution of the damage variable, D, with the equivalent plastic displacement following a linear form in the present study, is given by

$$D = \frac{\bar{u}^p}{\bar{u}_f^p}. \qquad (8)$$

Two sets of damage parameters for the solder alloy are considered in this study. The first one, referred to as the "standard" set, assumes $\bar{\varepsilon}_0^{pl}$ of 0.18 and $\bar{u}_f^p$ of 3 μm. The value of

$\bar{u}_f^p$ roughly corresponds to an equivalent plastic strain at failure of 0.5. These parameters were based on some measured tensile stress-strain curves of bulk pure Sn [36, 37]. It is understood that bulk materials and actual solder joints have significantly different physical sizes and microstructure and thus different constitutive responses. In addition, tensile loading tends to promote microvoid nucleation and coalescence, resulting in easier damage compared to other forms of loading. The present "standard" damage parameters should be viewed only as a lower-limit approximation. Nevertheless, this choice has an advantage that, when simulating cyclic deformation, there is no need to use a prohibitively large number of cycles before failure can be observed, thus enhancing the computational efficiency.

For the purpose of exploring the effect of damage parameters on the failure characteristics, a second set of damage parameters was used. The parameters were arbitrarily chosen to be three times those of the first (standard) set: $\bar{\varepsilon}_0^{pl}$ = 0.54 and $\bar{u}_f^p$ = 9 μm. A much greater deformation is thus needed to trigger solder damage when the second set of parameters is used in the simulation.

In this study we consider three different nominal shear strain rates imposed on the solder joint: 1 s^{-1}, 10 s^{-1} and 100 s^{-1}. In Chapter 3, results of the nominally pure shear loading will be presented. Chapters 4 and 5 are devoted to the effect of superimposed tension and compression on shear failure of the solder joint. In particular, we use the ratio of nominal tensile (compressive) strain rate and nominal shear strain rate to quantify the different modes of loading. The tension (compression)/shear ratios of 1/1, 1/5, 1/10 and 1/20 are

used for the presentation of results in Chapters 4 and 5. The case of cyclic deformation, focusing on the shear loading only, will be treated in Chapter 6. The first set of damage parameters are employed for the simulations in Chapters 3, 4 and 6, and the second set in Chapter 5. The general conclusions of this study will be given in Chapter 7.

Chapter 3 Shear Loading

In this chapter the modeling results on the nominal shear loading of the solder joint are presented. The first set of damage parameters defined in Chapter 2 is utilized. Attention is devoted to the evolution of stress/deformation fields as well as the failure pattern under different shearing rates.

Figure 3.1 shows the shear stress-shear strain curves of the solider joint, obtained from the finite element analysis with the nominal shear strain rates of 1, 10 and 100 s^{-1}. Here the shear stress is defined to be the applied load (reaction force in the x-direction) divided by the solder joint area (the initial area of the solder/substrate interface), and the shear strain is defined to be the applied displacement divided by the initial height of the solder. It can be seen that the cases of the 1 and 10 s^{-1} strain rates result in a well defined elastic-plastic-damage-failure sequence. The sharp drop of flow stress at the end of the plastic deformation is caused by the development of a major crack, as will be presented below. The stress-strain curve of the case of 100 s^{-1}, however, is less well defined and shows a large degree of fluctuation. This is due to the very fast loading rate which interferes with the propagation of stress waves inside the solder/substrate assembly. Despite the uncertainty in the stress-strain behavior in the case of 100 s^{-1}, the general trend of increasing plastic flow stress with increasing strain rate can still be seen in Fig. 3.1. This is consistent with the strain-rate hardening effect of viscoplasticity employed in the numerical model. Also observed in Fig. 3.1 is that the final failure strain in the case of

1 s^{-1} strain rate is much smaller compared to the other two cases. This will be discussed later in the chapter.

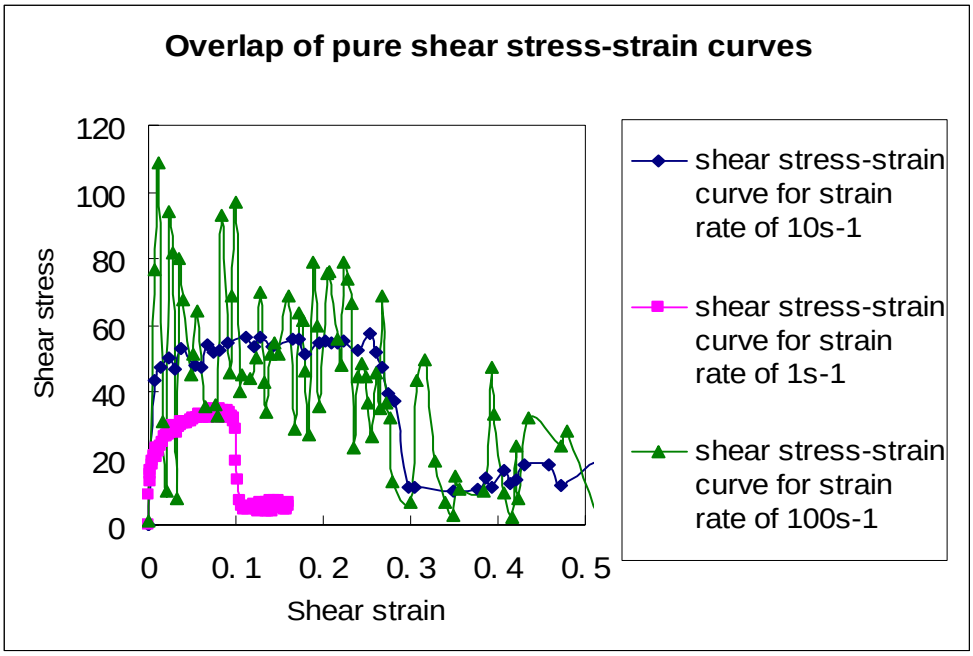

Fig. 3.1 Shear stress-strain curves for the case of $1s^{-1}$, $10s^{-1}$ and $100s^{-1}$ strain rates.

Figures 3.2(a), (b) and (c) show the contour plots of von Mises effective stress, shear stress σ_{xy} and equivalent plastic strain, respectively, at a nominal shear strain of 0.05 in the case of the 1 s^{-1} shear strain rate. For clarity only a small portion of the copper substrate adjacent to the solder is included in the figures. The corresponding plots for the strain rates of 10 s^{-1} and 100 s^{-1} are shown in Figs. 3.3 and 3.4, respectively. It can be seen from Figs. 3.2(a), 3.3(a) and 3.4(a) that relatively high von Mises stresses exist in the intermetallic layers and the copper substrates close to the joint. The stress in solder increases as the strain rate increases under the same overall shear strain, due to the viscoplastic effect. The same trend can be observed for the magnitude of shear stress σ_{xy}

(part (b) in Figs. 3.2, 3.3 and 3.4). It is noted that, although the solder joint in under nominally pure shear loading, the shear stress field insider the solder is far from uniform. In these figures damage in solder has not been initiated, but extensive plastic yielding has occurred. The equivalent plastic strain contours in Figs. 3.2(c), 3.3(c) and 3.4(c) show very different patterns. Plastic deformation is localized near the interface region when the applied shear strain rate is small (Fig. 3.2(c)). In the other two cases, however, high plastic strains are seen around the four corners, and there is a tendency for the relatively high-strain regions to form a band parallel to the interface but inside the solder. This will have implications for the damage evolution as will be shown below.

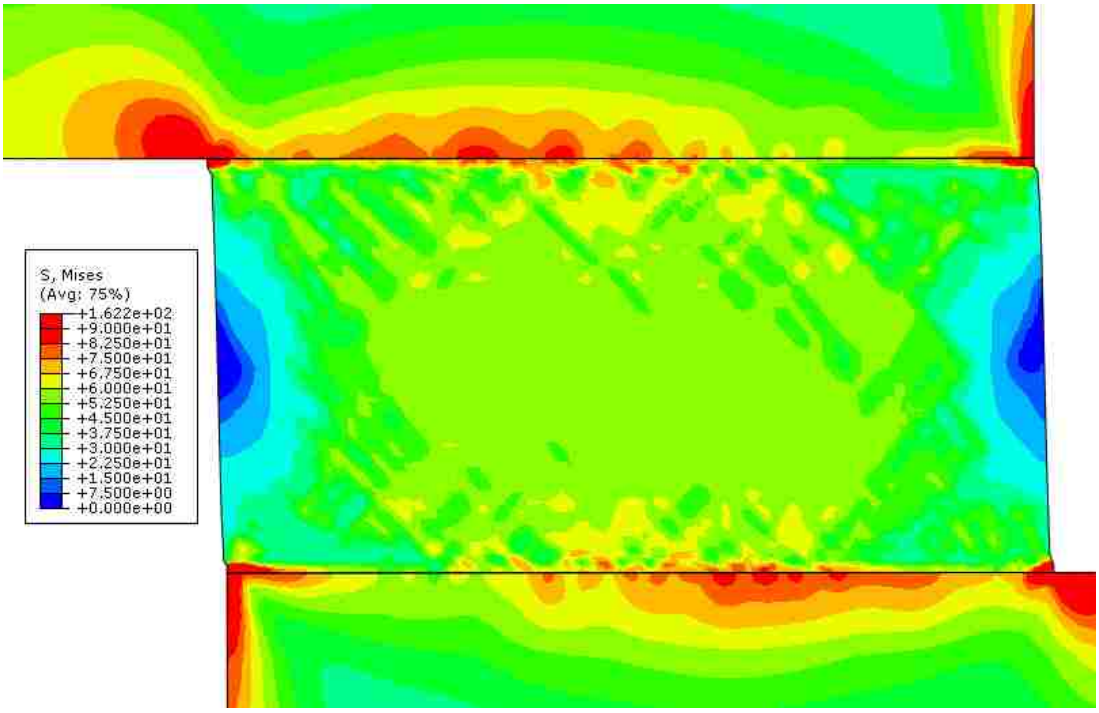
S, Mises
(Avg: 75%)
+1.622e+02
+9.000e+01
+8.250e+01
+7.500e+01
+6.750e+01
+6.000e+01
+5.250e+01
+4.500e+01
+3.750e+01
+3.000e+01
+2.250e+01
+1.500e+01
+7.500e+00
+0.000e+00

3.2(a)

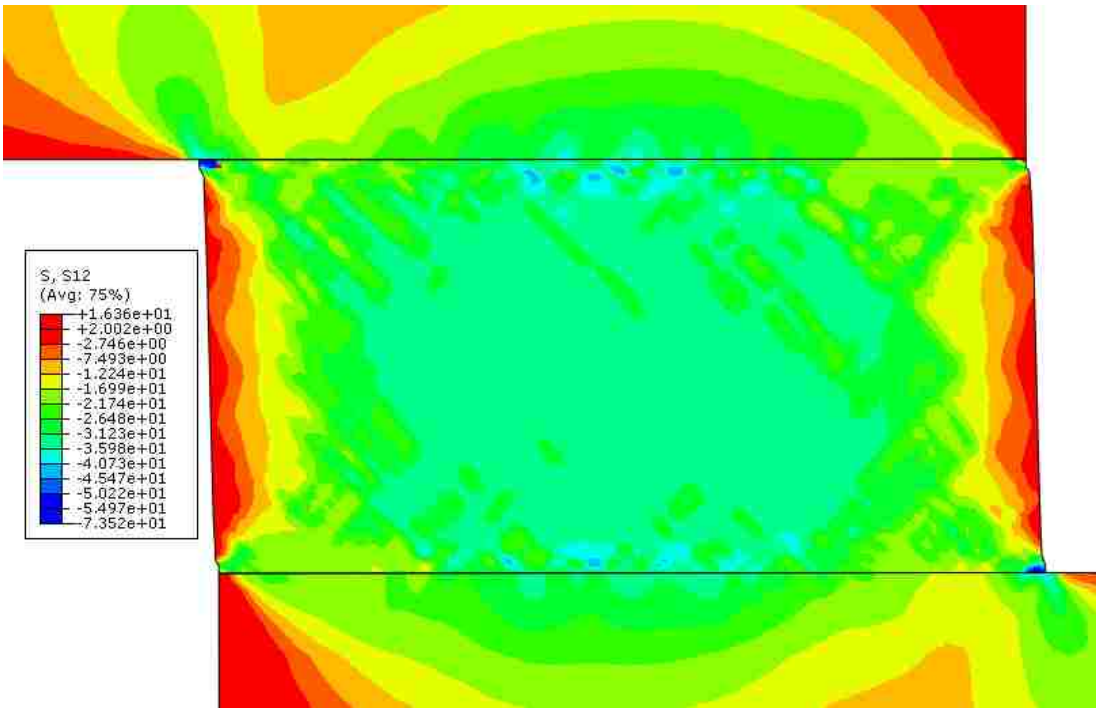
S, S12
(Avg: 75%)
+1.636e+01
+2.002e+00
-2.746e+00
-7.493e+00
-1.224e+01
-1.699e+01
-2.174e+01
-2.648e+01
-3.123e+01
-3.598e+01
-4.073e+01
-4.547e+01
-5.022e+01
-5.497e+01
-7.352e+01

3.2(b)

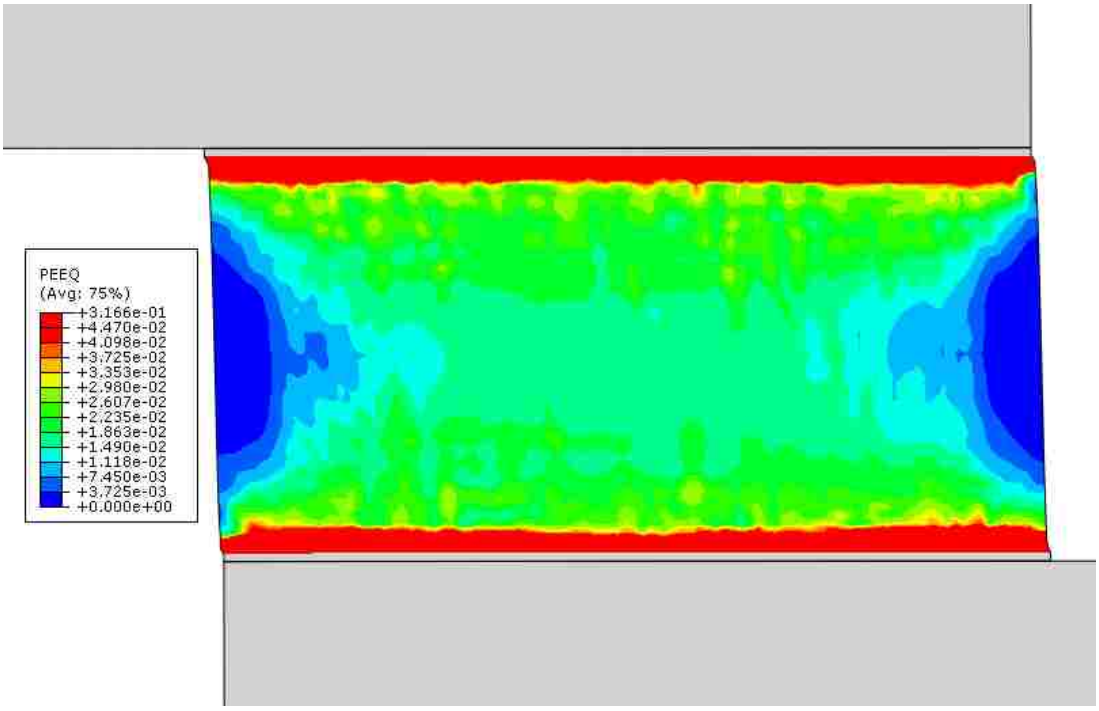

3.2(c)

Fig. 3.2 Contour plots showing (a) von Mises effective stress, (b) Shear stress and (c) equivalent plastic strain in the case of $1s^{-1}$ shear strain rate.

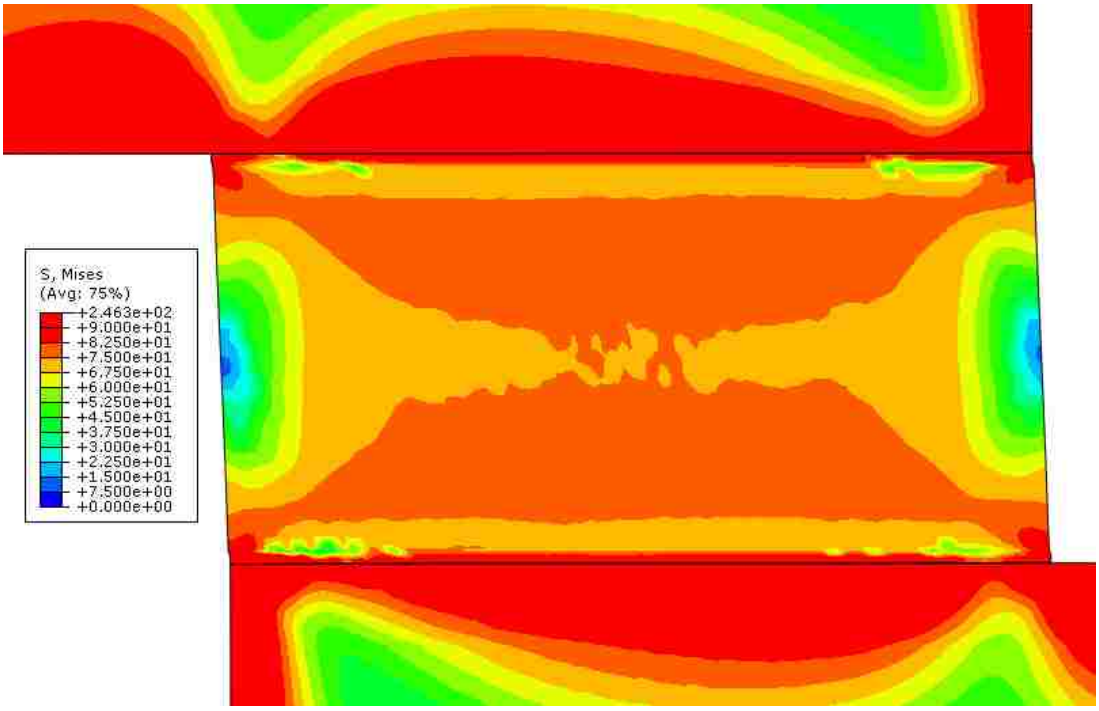
S, Mises
(Avg: 75%)
+2.463e+02
+9.000e+01
+8.250e+01
+7.500e+01
+6.750e+01
+6.000e+01
+5.250e+01
+4.500e+01
+3.750e+01
+3.000e+01
+2.250e+01
+1.500e+01
+7.500e+00
+0.000e+00

3.3 (a)

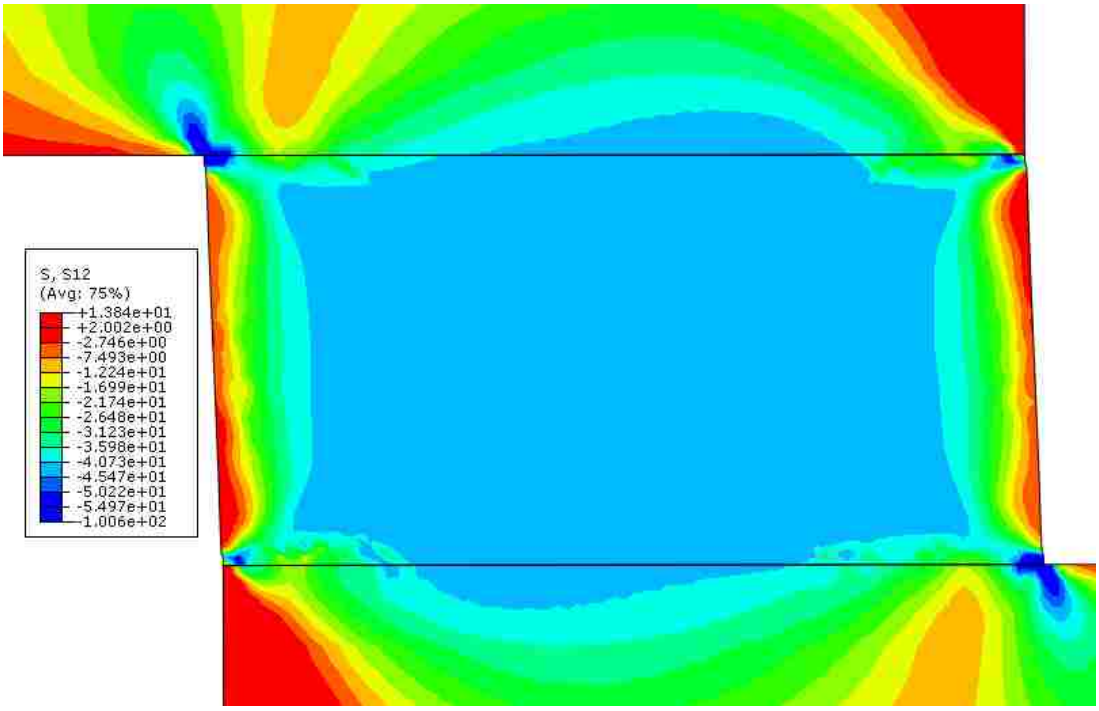
S, S12
(Avg: 75%)
+1.384e+01
+2.002e+00
-2.746e+00
-7.493e+00
-1.224e+01
-1.699e+01
-2.174e+01
-2.648e+01
-3.123e+01
-3.598e+01
-4.073e+01
-4.547e+01
-5.022e+01
-5.497e+01
-1.006e+02

3.3 (b)

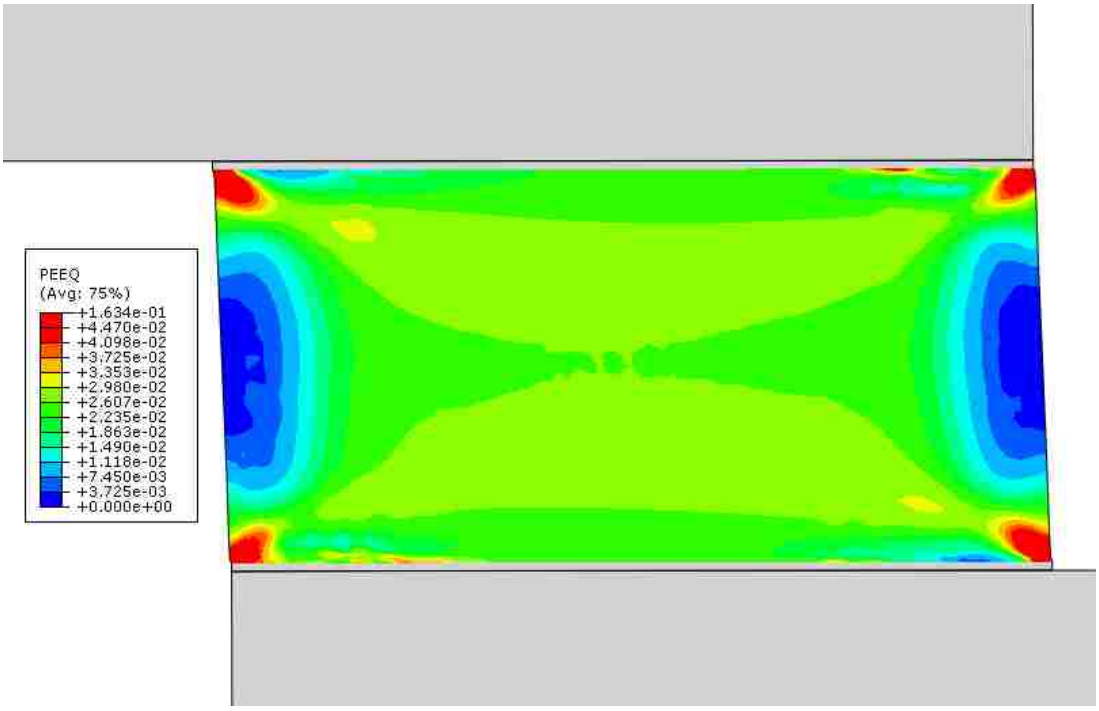

3.3 (c)

Fig. 3.3 Contour plots showing (a) von Mises effective stress, (b) shear stress and (c) equivalent plastic strain in the case of 10s^{-1} shear strain rate

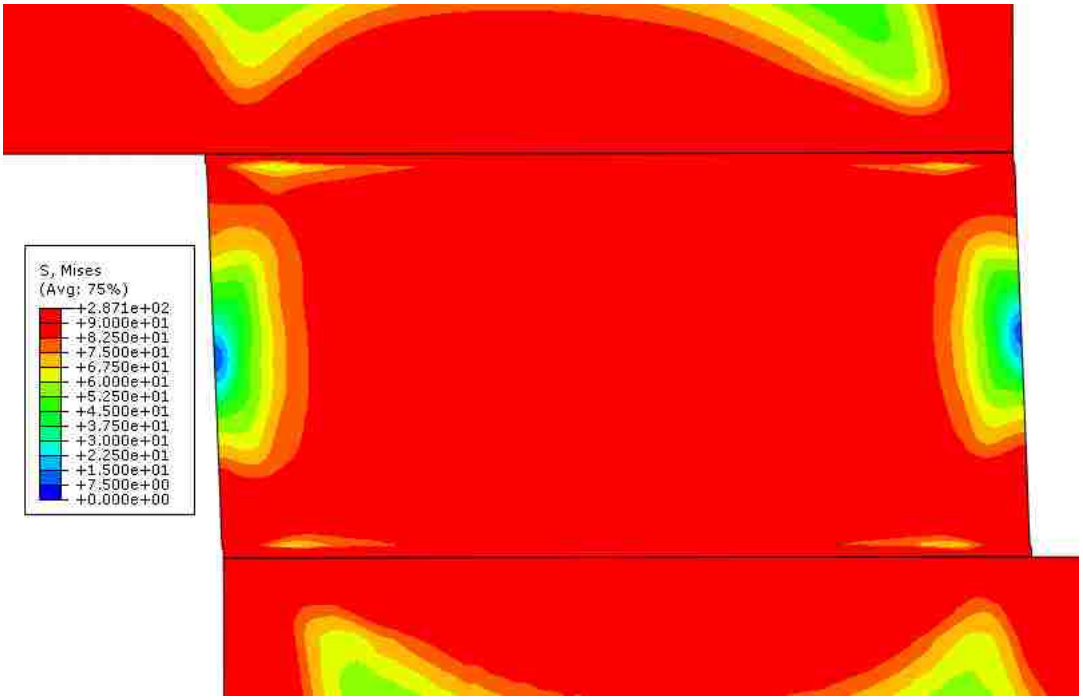
S, Mises
(Avg: 75%)
+2.871e+02
+9.000e+01
+8.250e+01
+7.500e+01
+6.750e+01
+6.000e+01
+5.250e+01
+4.500e+01
+3.750e+01
+3.000e+01
+2.250e+01
+1.500e+01
+7.500e+00
+0.000e+00

3.4(a)

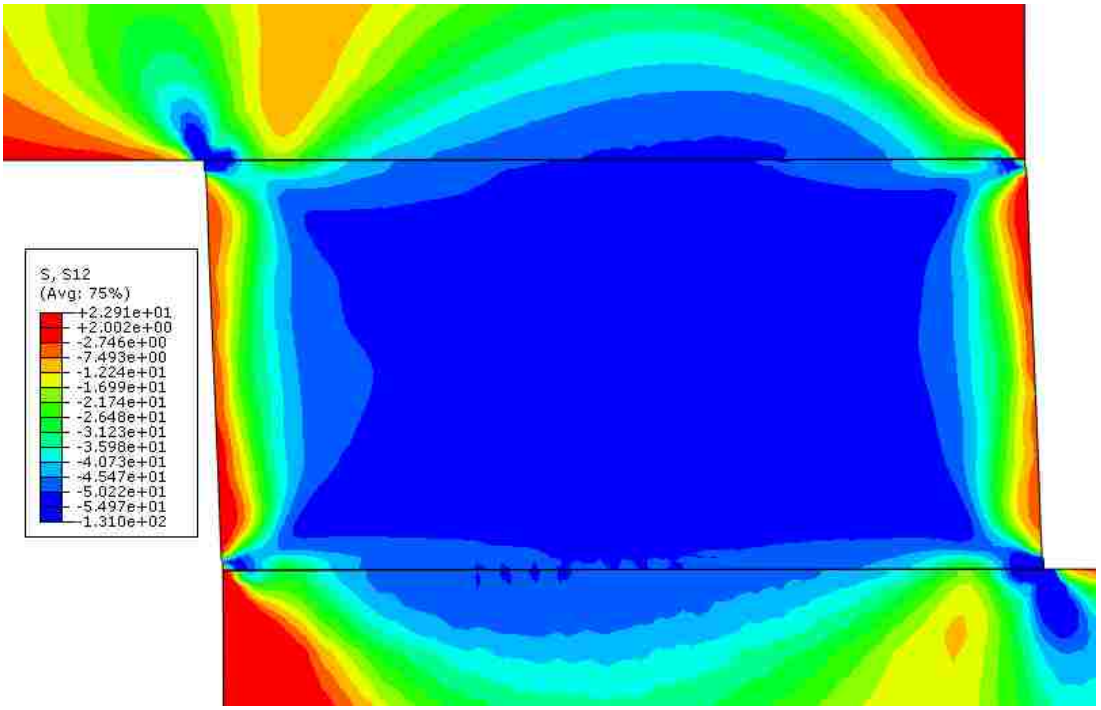
S, S12
(Avg: 75%)
+2.291e+01
+2.002e+00
-2.746e+00
-7.493e+00
-1.224e+01
-1.699e+01
-2.174e+01
-2.648e+01
-3.123e+01
-3.598e+01
-4.073e+01
-4.547e+01
-5.022e+01
-5.497e+01
-1.310e+02

3.4(b)

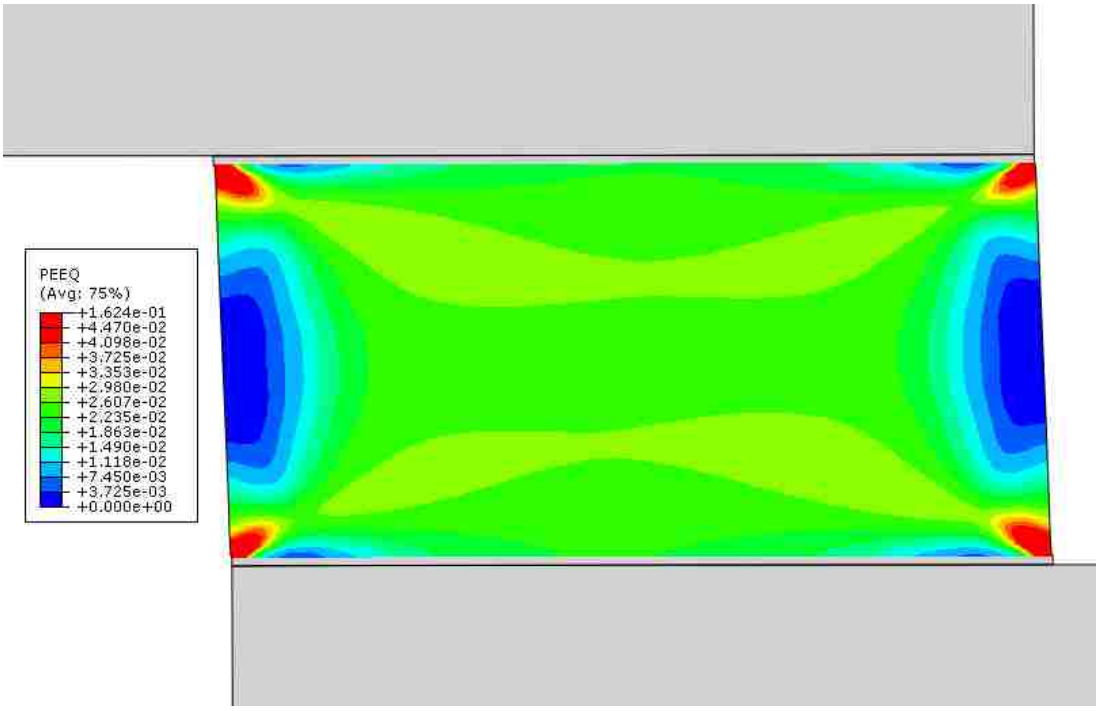

3.4(c)

Fig. 3.4 Contour plots showing (a) von Mises effective stress, (b) shear stress and (c) equivalent plastic strain in the case of 100s^{-1} shear strain rate

Attention is now turned to the ductile failure pattern in solder under the different applied strain rates. Figures 3.5(a) and (b) show the contour plots of equivalent plastic strain along with the failure (removed elements), at the early stage of the cracking process and upon final failure, respectively, for the case of 1 s^{-1} strain rate. Note that final failure occurs when a major crack traversing the entire span of solder joint is formed. The corresponding plots for the cases of 10 s^{-1} and 100 s^{-1} strain rates are shown in Figs. 3.6 and 3.7, respectively. In Fig. 3.5, the initiation of crack appears at the upper right corner of the solder. Crack propagation follows the path of greatest equivalent plastic strain, which in turn is evolving during the deformation and damage processes. It is seen that the initiated corner crack first propagates close to, but not at, the interface between the solder alloy and the intermetallic. However, it links up with a crack from the upper left corner along the interface, and causes final fracture. It is worth pointing out that the current numerical model does not include any true interface failure features; the simulated "interface" fracture is still due to the ductile damage model of solder adopted in the analysis.

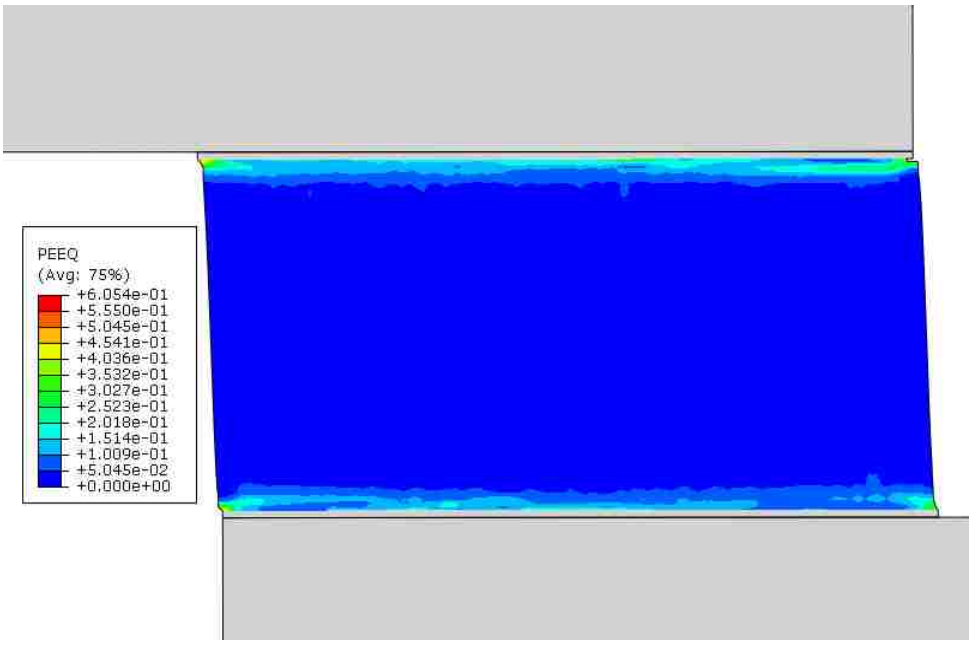

3.5(a)

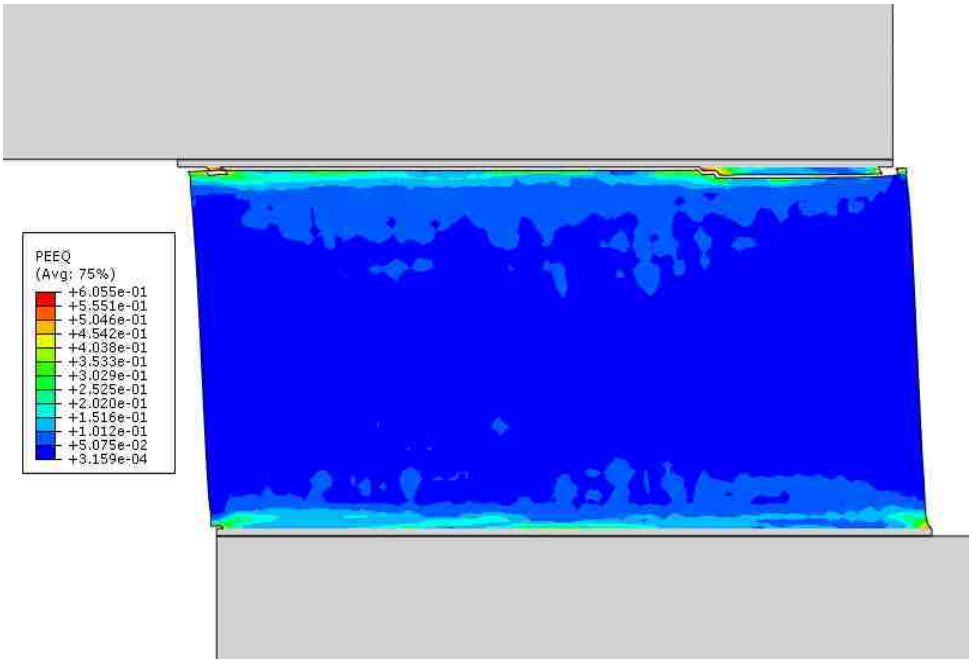

3.5(b)

Fig.3.5 Contours of equivalent plastic strain for the case of $1s^{-1}$ strain rate (a) shortly after cracking begins and (b) shortly after complete failure of the joint.

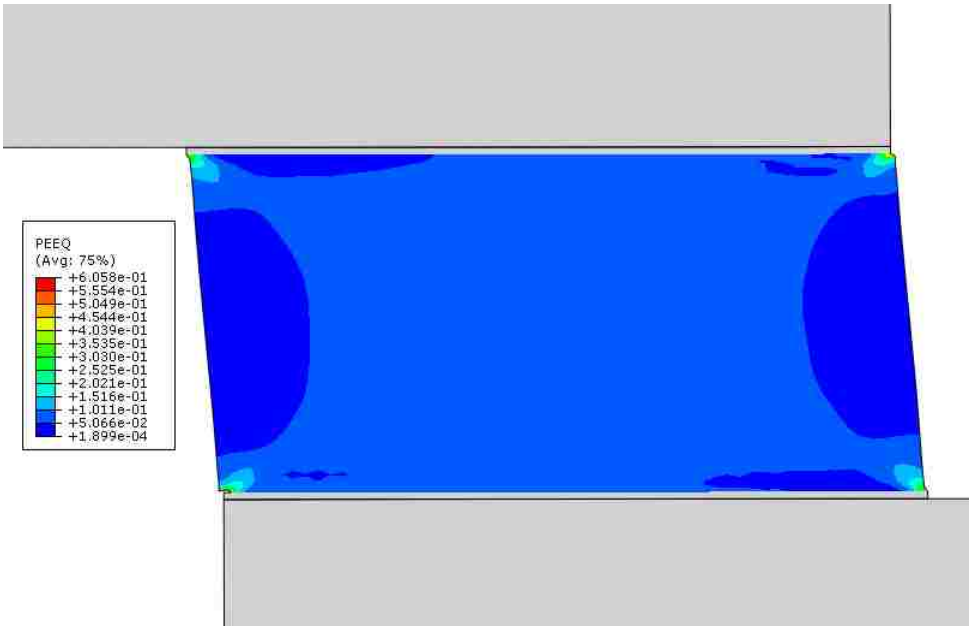

3.6(a)

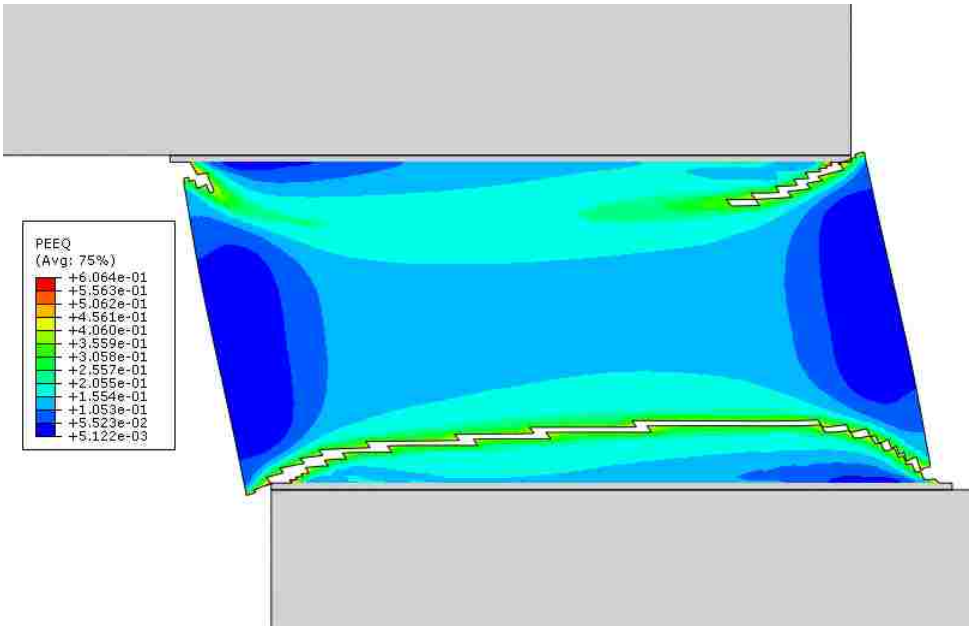

3.6 (b)

Fig.3.6.Contours of equivalent plastic strain for the case of $10s^{-1}$ strain rate (a) shortly after cracking begins and (b) shortly after complete failure of the joint.

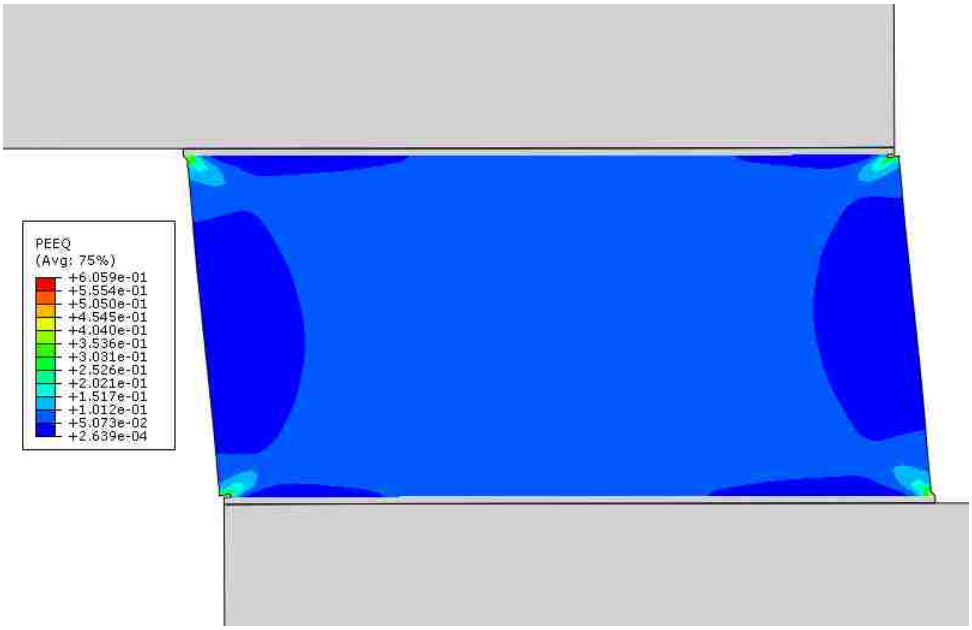

3.7 (a)

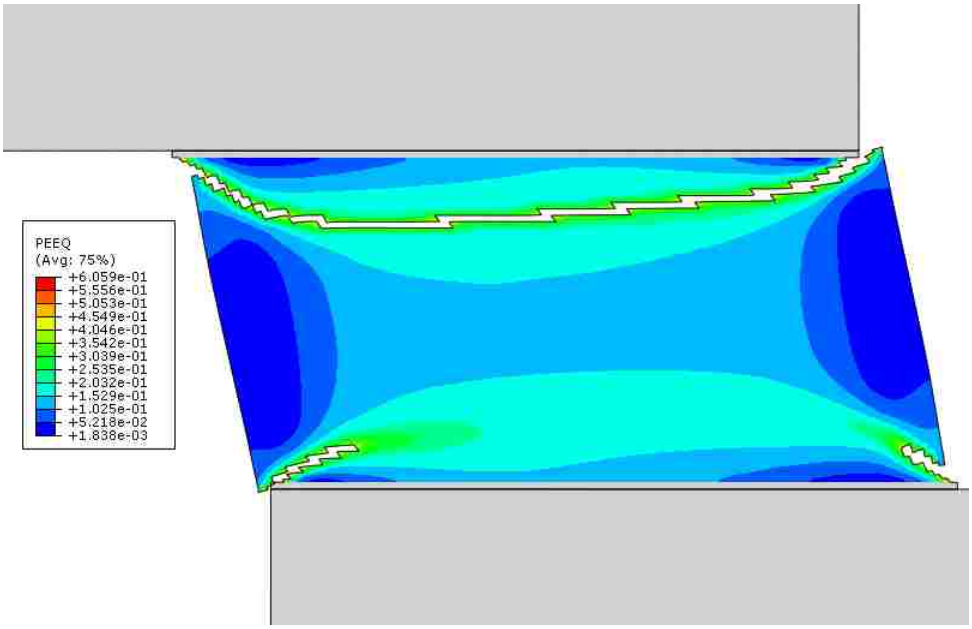

3.7 (b)

Fig. 3.7 Contours of equivalent plastic strain for the case of 100s^{-1} strain rate (a) shortly after cracking begins and (b) shortly after complete failure of the joint.

A different form of crack pattern is observed when the applied shear strain rates are higher, as in Figs. 3.6 and 3.7. Cracks still initiate in the corner region, and they tend to grow inward along the near 45° direction. However, owing to the dominant shear deformation mode, a band of strong plastic deformation in the horizontal direction gradually forms parallel to each interface. Damage therefore localizes along the band where final linkage of cracks takes place. Note that in these two fast loading conditions, the strain-rate hardening effect is particularly strong and any concentration of plasticity adjacent to the interface is quickly "diffused" away, leading to a crack path farther from the interface. This also explains the higher ductility (greater failure strain) under the $10s^{-1}$ and 100 s^{-1} strain rates, compared to case of 1 s^{-1} as seen in Fig. 3.1.

From the present numerical analysis, a faster loading rate is seen to result in an increase in failure strain. Conventional wisdom stipulates that a metal tends to become more brittle under a higher strain rate. However, the current study suggests that the solder joint can actually become more ductile as the applied strain rate increases. This is due to the highly non-uniform deformation field and the associated alteration of failure path. As a consequence, this study brings about the possibility of improving solder joint reliability under drop and impact conditions, through proper design and choice of the material and geometry.

Chapter 4 Effects of Superimposed Tension/Compression on Shear Failure

In this chapter, we focus on the failure pattern induced by shear, under the influence of tensile or compressive deformation. The motivation for this analysis is that, in typical drop and impact loading of electronic packages, shear is generally not the only deformation mode. Depending on the relative positions of the solder joint in the device and the impact angle, local tensile or compressive stresses can arise. For simplicity, we assume that the normal stress is generated by a constant velocity in the y-direction, imposed on the bottom boundary of the lower copper substrate (simultaneously with the shear deformation). A given applied velocity in y results in a constant nominal tensile or compressive strain rate in the solder. Different tensile (or compressive) strain rates are chosen so as to give different ratios of tensile (or compressive) strain rate to shear strain rate. It should be noted that the present approach is an idealization of the loading condition, for the purpose of gaining a first-order insight into the phenomenon. In actual drop and impact, the strain rate experienced by the solder will not be constant and can be of the pulsed or vibrational form.

A large number of simulations were carried out. To conserve space, only salient results are included in the following sections.

4.1 Pure Tensile and Compressive Deformation

Before the effects of superimposed tension or compression can be discussed, the baseline cases of pure tension and pure compression should be examined. Here we present a series of contours plots of equivalent plastic strain with the cracking pattern. Figures 4.1-4.3 show the results of pure tensile deformation for the nominal tensile strain rates of 1 s^{-1}, 10 s^{-1} and 100 s^{-1}, respectively. Parts (a) and (b) in these figures represent the deformed configurations shortly after crack initiation and shortly after final failure, respectively.

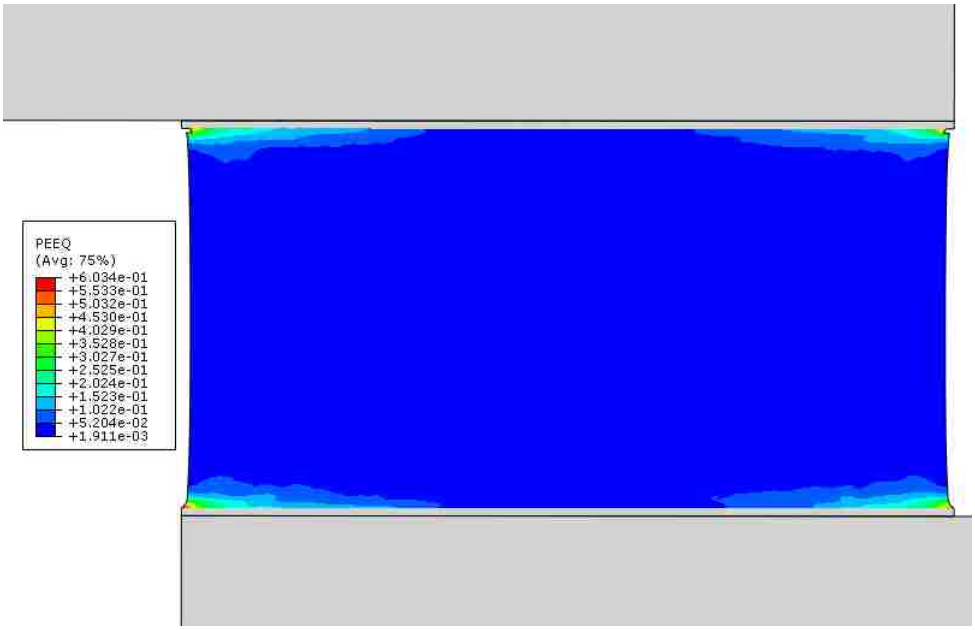

(a)

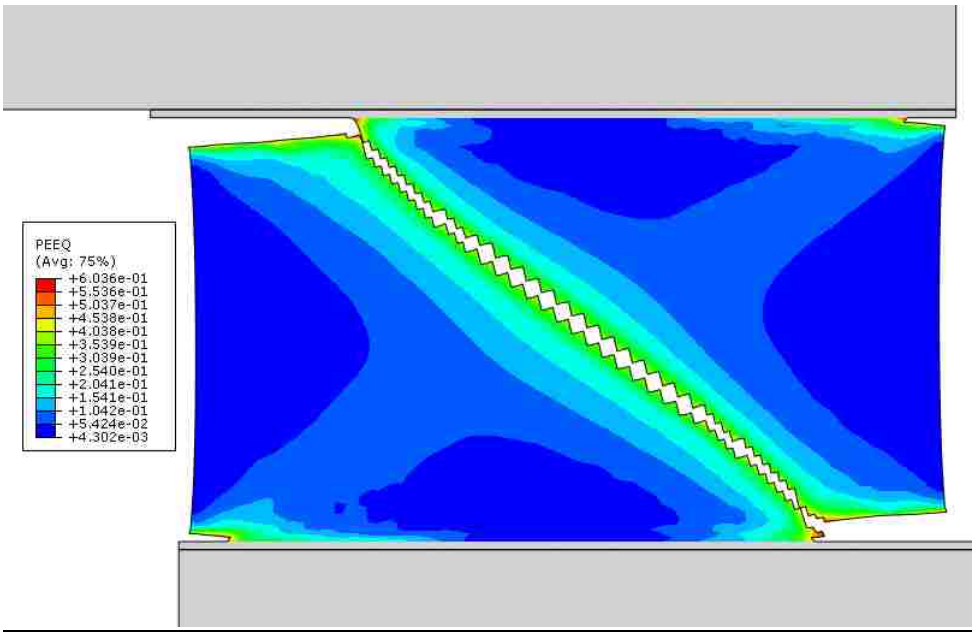

(b)

Fig. 4.1 Contour plots of pure tensile deformation showing the equivalent plastic strain for the case of $1s^{-1}$ strain rate.

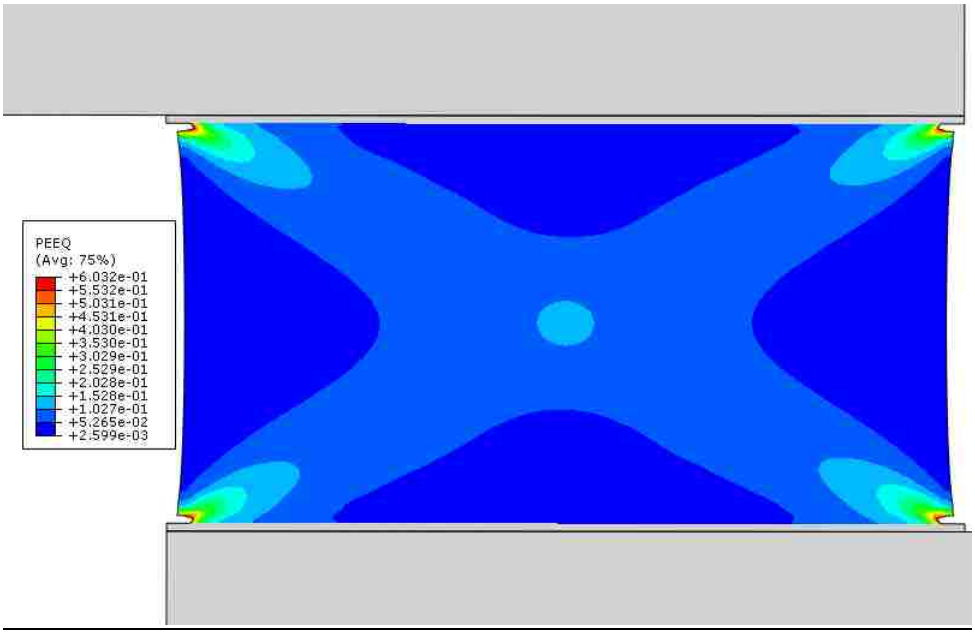

(a)

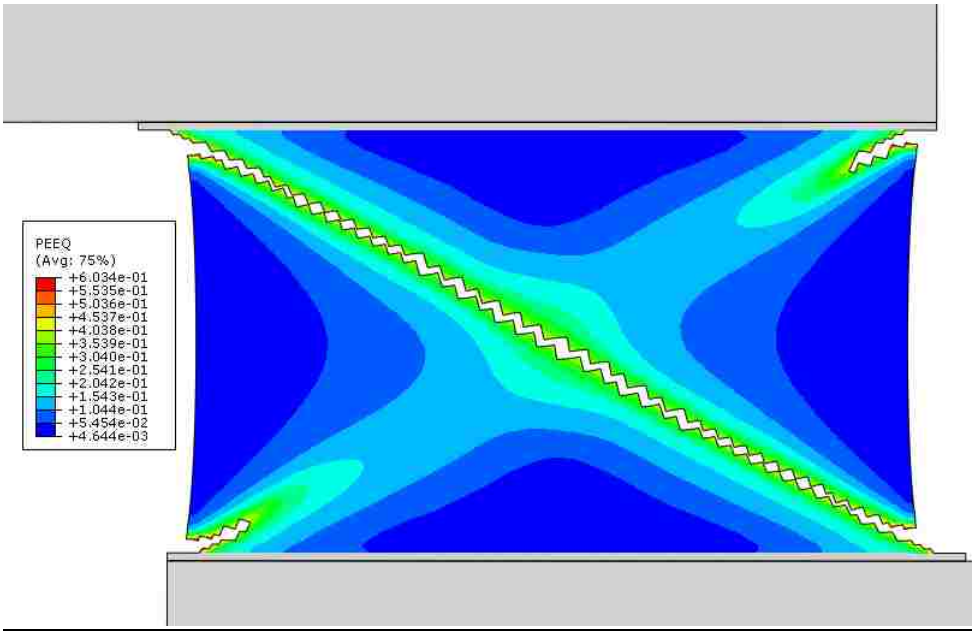

(b)

Fig. 4.2 Contour plots of pure tensile deformation showing the equivalent plastic strain for the case of $10s^{-1}$ strain rate.

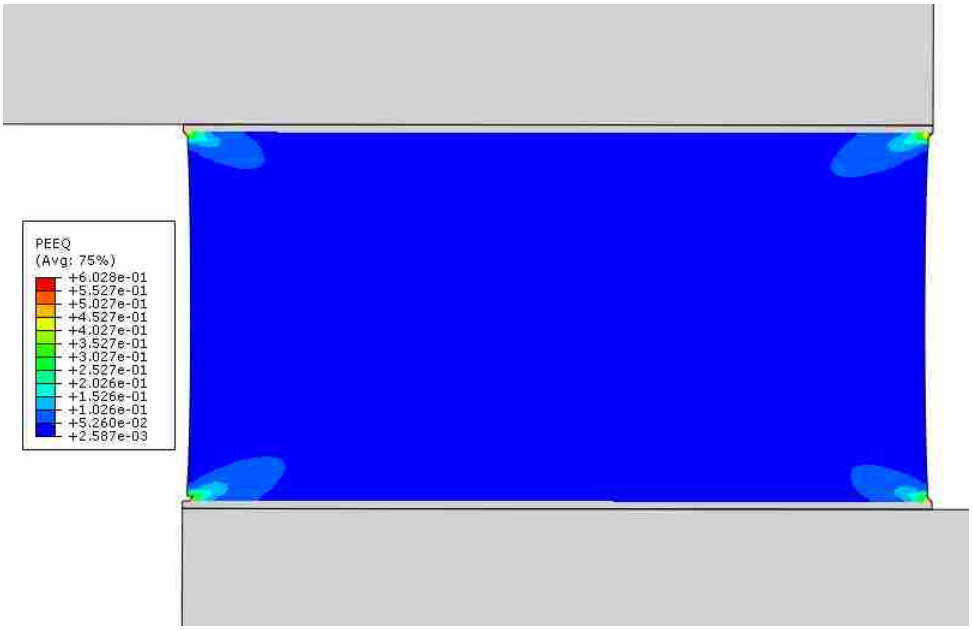

(a)

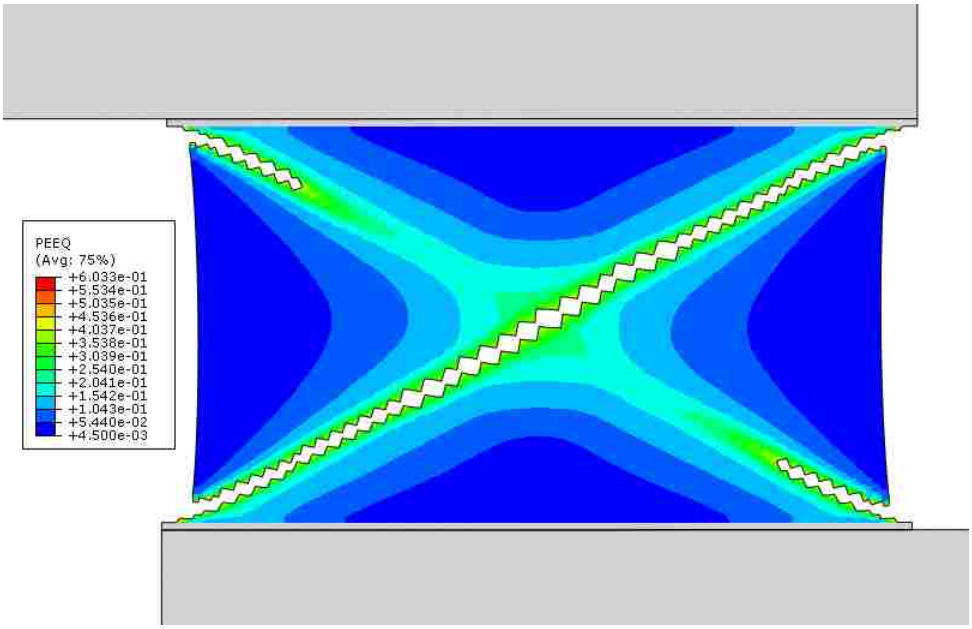

(b)

Fig. 4.3 Contour plots of pure tensile deformation showing the equivalent plastic strain for the case of 100s^{-1} strain rate.

It can be seen that in Fig. 4.1 where the strain rate is the lowest, cracks first form along the interface between the solder and the intermetallic layer. However, they soon link up along the near 45° direction in which the highest shear stress takes place. The damage mode in Figs. 4.2 and 4.3 is similar, with the exception that the interface part of the failure does not exist. This is again due to the strong strain-rate hardening effect when the applied tensile strain rate is higher.

Figure 4.4 shows the modeled tensile stress-strain curves for the three strain rates. Here the quantities of stress and strain are based on the ordinary "engineering" definition. It is evident that the peak flow stress increases with the applied strain rate. The tensile ductility increases slightly with an increasing applied strain rate.

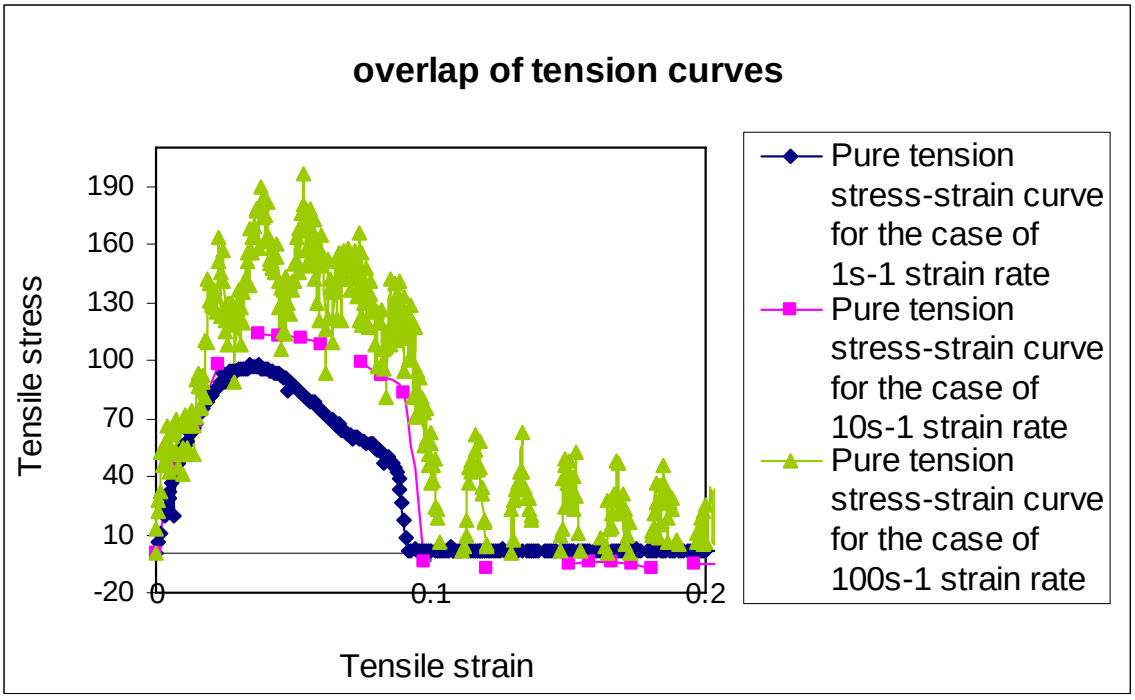

Fig. 4.4 Stress-strain curves resulting from the nominally pure tensile loading for all the strain rates.

Attention is now turned to the case of pure compression. Figures 4.5-4.7 show the results of pure compressive deformation for the nominal compressive strain rates of 1 s^{-1}, 10 s^{-1} and 100 s^{-1}, respectively. As in the case of tension above, parts (a) and (b) in these figures represent the deformed configurations shortly after crack initiation and shortly after final failure, respectively. The compressive stress-strain curves for the three strain rates are shown in Fig. 4.8. It can be seen that the evolution of failure shows similar general features as in the case of tension. Initial cracking along the interface between the solder and the intermetallic occurs when the strain rate is low. Final fracture, however, takes the path of near-45º direction in all cases. Note that the "overlapping" after complete failure observed in Fig. 4-5 (b), due to the fact that there is no contact algorithm implemented in the simulation, is unphysical. Nevertheless, the fundamental features of ductile damage obtained from the simulation are still valid. In Fig. 4.8, the stress-strain curves also show similar behavior as in the case of pure tension.

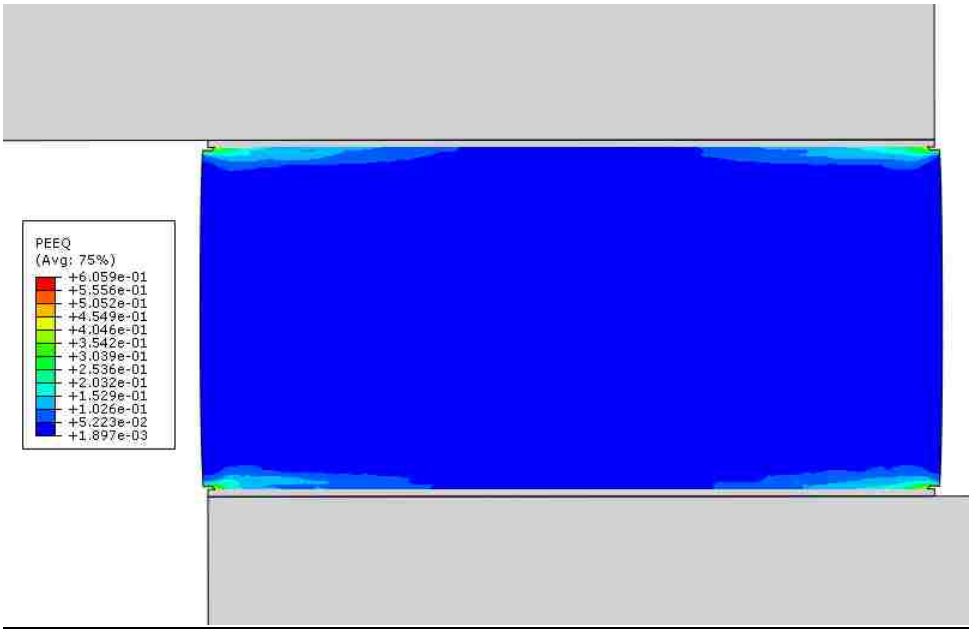

(a)

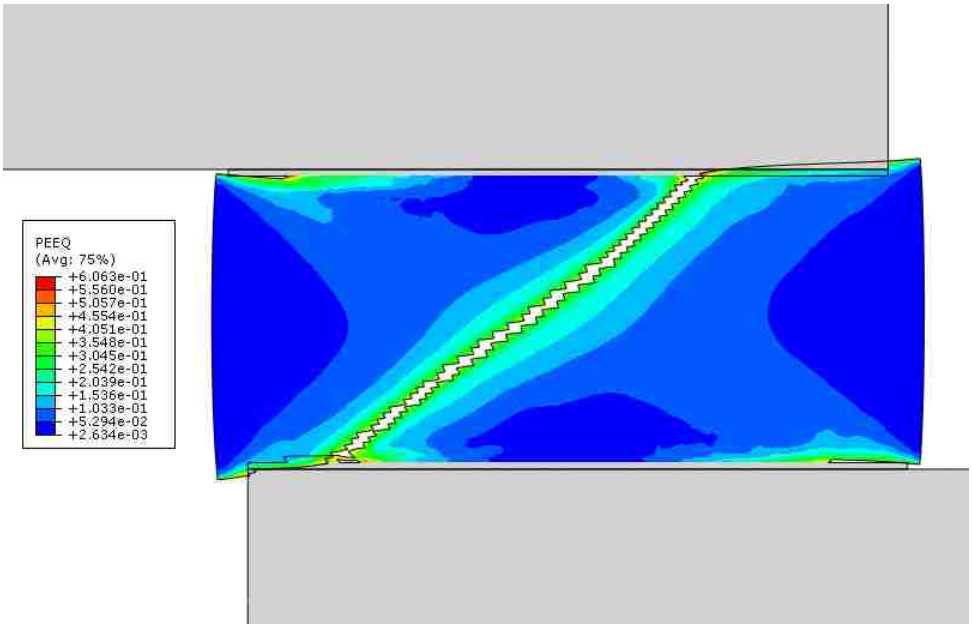

(b)

Fig. 4-5 Contour plots of pure compressive deformation showing the equivalent plastic strain for the case of $1s^{-1}$ strain rate

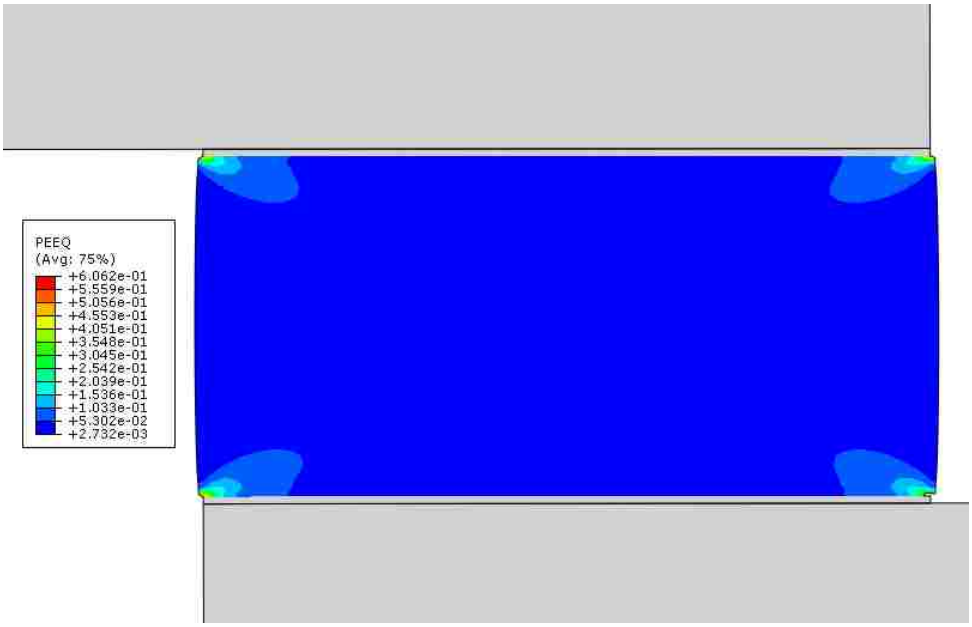

(a)

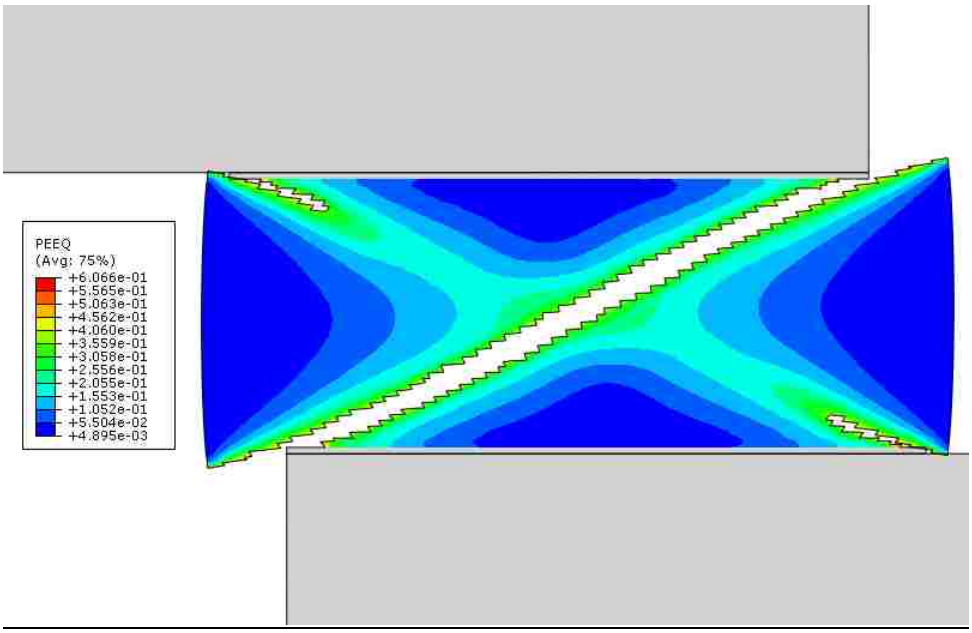

(b)

Fig. 4-6 Contour plots of pure compressive deformation showing the equivalent plastic strain for the case of $10s^{-1}$ strain rate

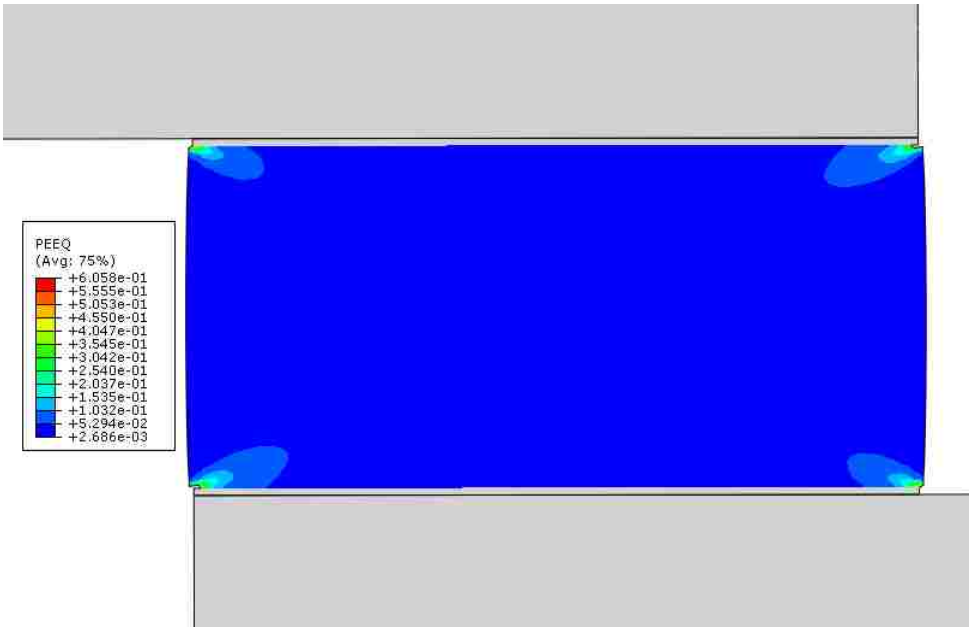

(a)

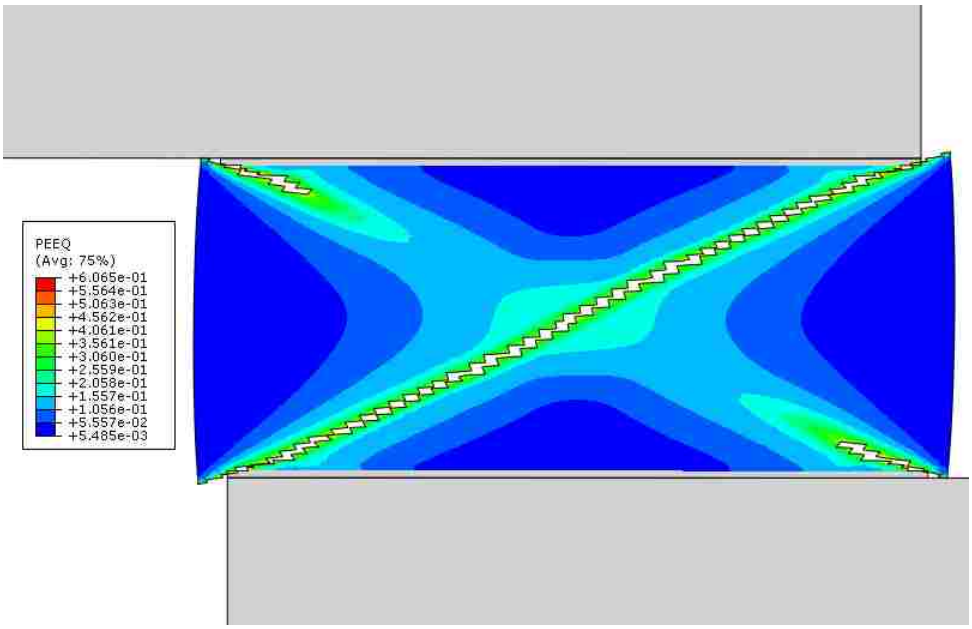

(b)

Fig. 4-7 Contour plots of pure compressive deformation showing the equivalent plastic strain for the case of 100s^{-1} strain rate

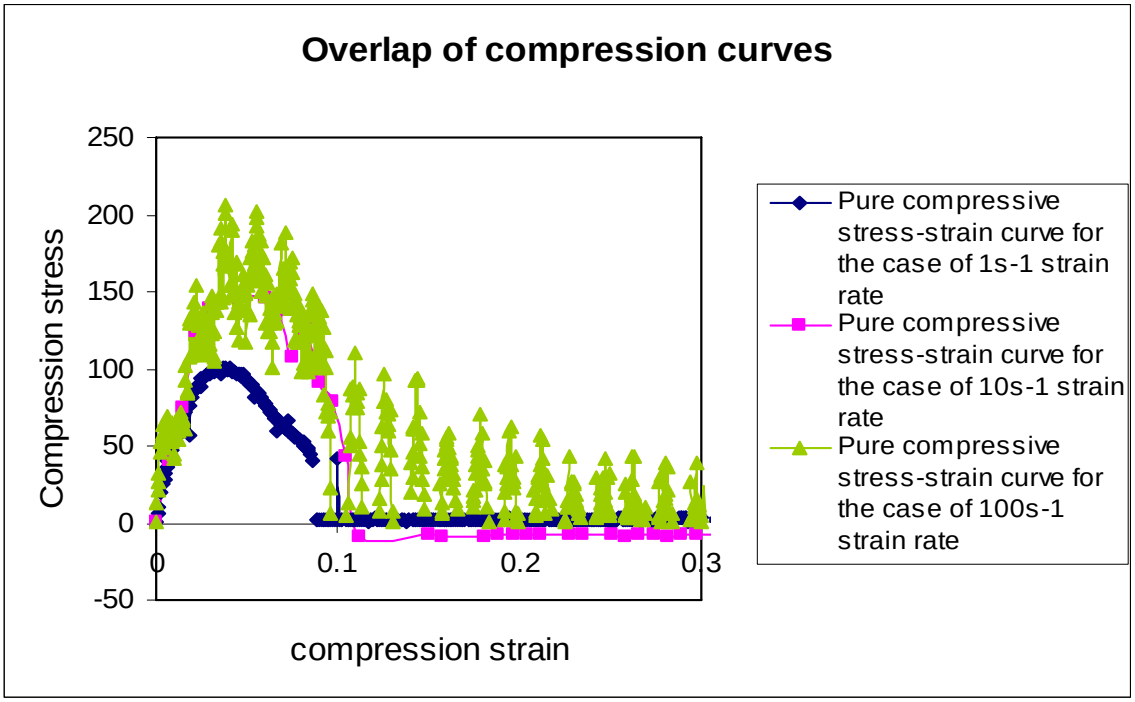

Fig. 4-8 Stress-strain curves resulting from the nominally pure compressive loading for all the strain rates.

4.2 Shear Loading with Superimposed Tension

In this section, we investigate how the superimposed tension will affect the failure pattern in the shearing of solder joint. Various combinations of the tensile strain rate and shear strain rate were employed. In the presentation below each combination is designated as a ratio of tensile-to-shear strain rates (under an applied shear strain rate). Note that, with a fixed time of deformation, the total tensile strain and shear strain also follow the same ratio.

Since pure tension and pure shear result in distinctly different failure appearances (near 45º in tension; mostly parallel to interface in shear), the mixed-mode effect can be observed from the cracking configuration in a straightforward manner. To simplify the presentation, salient results are summarized in Table 4.1. The table lists the apparent dominant failure mode ("tension" or "shear") for each combination of the shear strain rate and the ratio of tensile-to-shear strain rates.

Table 4.1 Dominant failure mode ("tension" or "shear") observed from the finite element simulation. For each shear strain rate, four different ratios of tensile strain rate/shear strain rate are considered.

Shear strain rate (s^{-1})	Tension/Shear (1/1)	Tension/Shear (1/5)	Tension/Shear (1/10)	Tension/Shear (1/20)
1	Tension	Shear	Shear	Shear
10	Tension	Tension	Shear	Shear
100	Tension	Tension	Tension	Shear

Table 4.1 shows that the superimposed tension can influence the failure mode to a great extent. The influence becomes larger as the shear strain rate increases. For instance, at a shear strain rate of 100 s^1, even a small ratio of tensile and shear strain rates (1/10) can force the cracking to follow the tensile mode. For smaller shear strain rates, a greater

ratio is needed. In Fig. 4.9 we present contour plots showing the failure morphology of the following six cases of the strain rates:

(a) Shear strain rate 1 s^{-1}, tension/shear ratio 1/1,

(b) Shear strain rate 1 s^{-1}, tension/shear ratio 1/5,

(c) Shear strain rate 10 s^{-1}, tension/shear ratio 1/5,

(d) Shear strain rate 10 s^{-1}, tension/shear ratio 1/10,

(e) Shear strain rate 100 s^{-1}, tension/shear ratio 1/10, and

(f) Shear strain rate 100 s^{-1}, tension/shear ratio 1/20.

Note that these six cases correspond to the strain rate conditions across the "boundary" between the tension mode (red) and shear mode (blue) in Table 4.1. It can be seen from Fig. 4.9 that the failure mode indeed appears in a distinct manner: either the tension mode or the shear mode with no ambiguity (although the loading has both the tension and shear components).

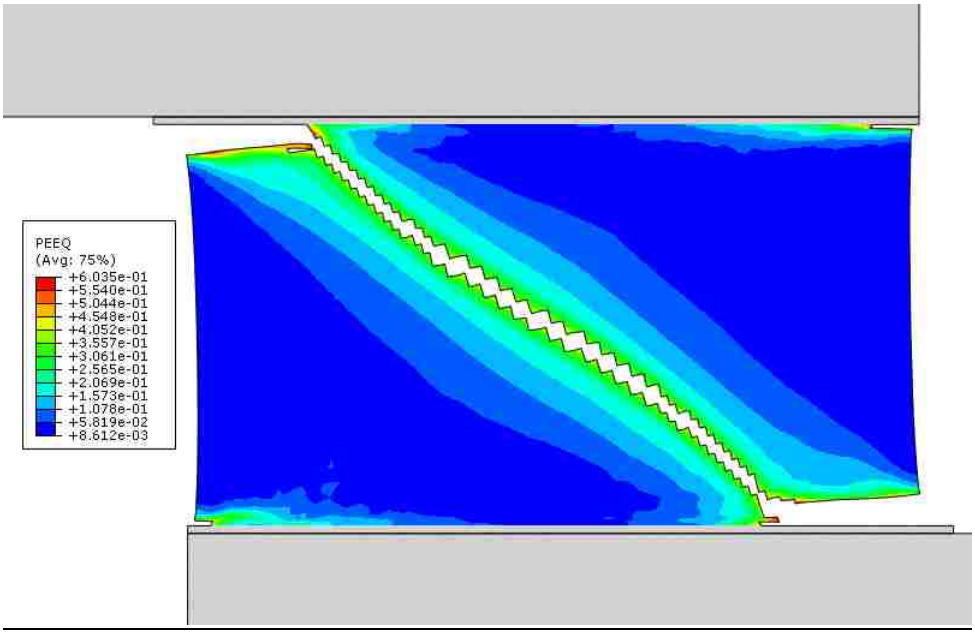
PEEQ
(Avg: 75%)
+6.035e-01
+5.540e-01
+5.044e-01
+4.548e-01
+4.052e-01
+3.557e-01
+3.061e-01
+2.565e-01
+2.069e-01
+1.573e-01
+1.078e-01
+5.819e-02
+8.612e-03

(a)

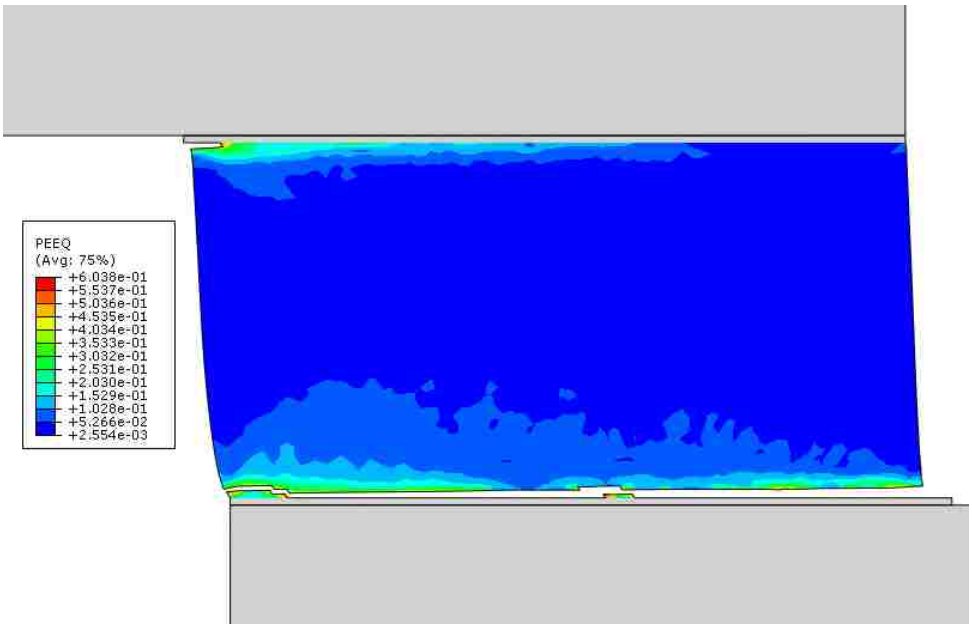
PEEQ
(Avg: 75%)
+6.038e-01
+5.537e-01
+5.036e-01
+4.535e-01
+4.034e-01
+3.533e-01
+3.032e-01
+2.531e-01
+2.030e-01
+1.529e-01
+1.028e-01
+5.266e-02
+2.554e-03

(b)

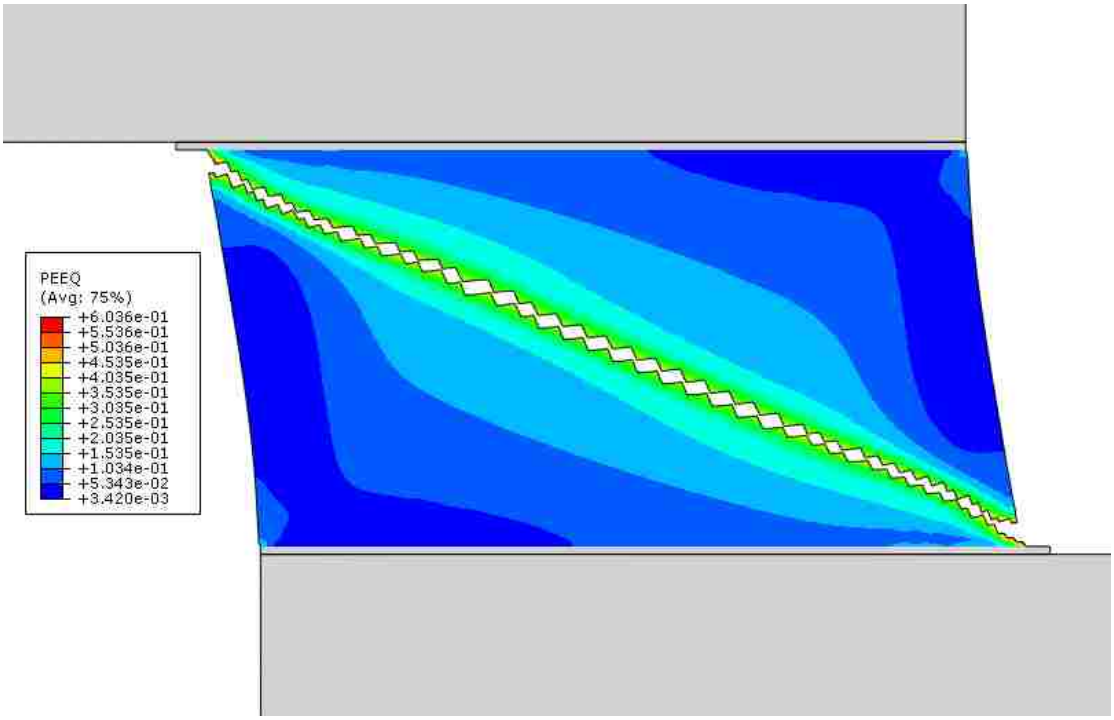
PEEQ
(Avg: 75%)
+6.036e-01
+5.536e-01
+5.036e-01
+4.535e-01
+4.035e-01
+3.535e-01
+3.035e-01
+2.535e-01
+2.035e-01
+1.535e-01
+1.034e-01
+5.343e-02
+3.420e-03

(c)

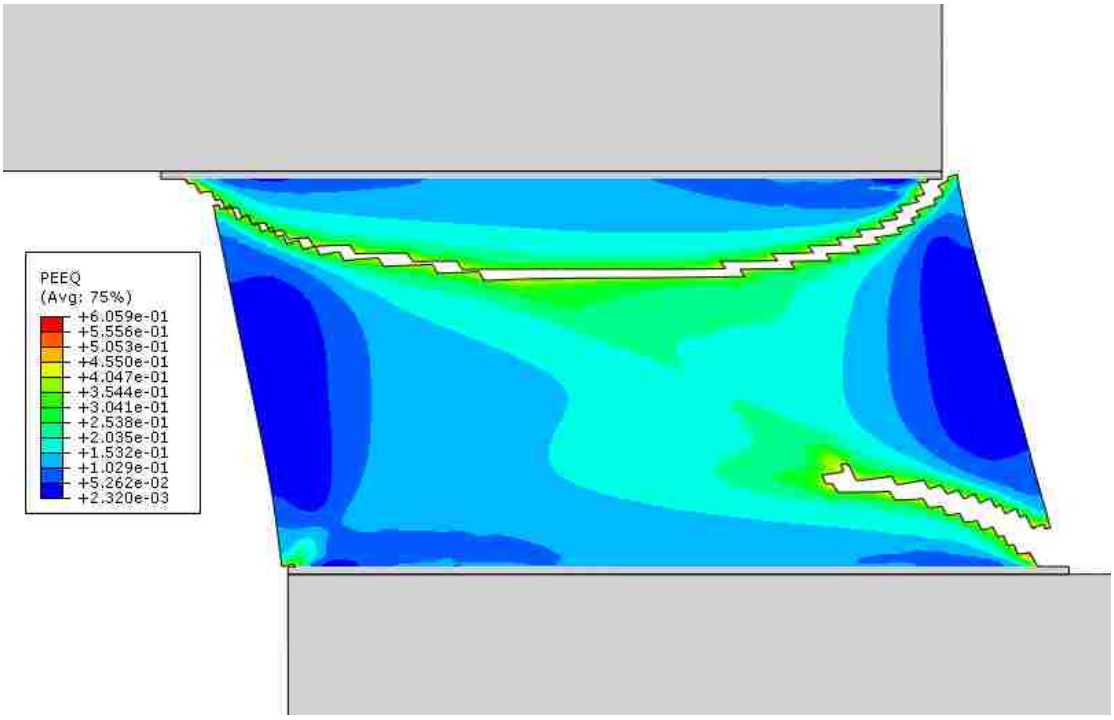
PEEQ
(Avg: 75%)
+6.059e-01
+5.556e-01
+5.053e-01
+4.550e-01
+4.047e-01
+3.544e-01
+3.041e-01
+2.538e-01
+2.035e-01
+1.532e-01
+1.029e-01
+5.262e-02
+2.320e-03

(d)

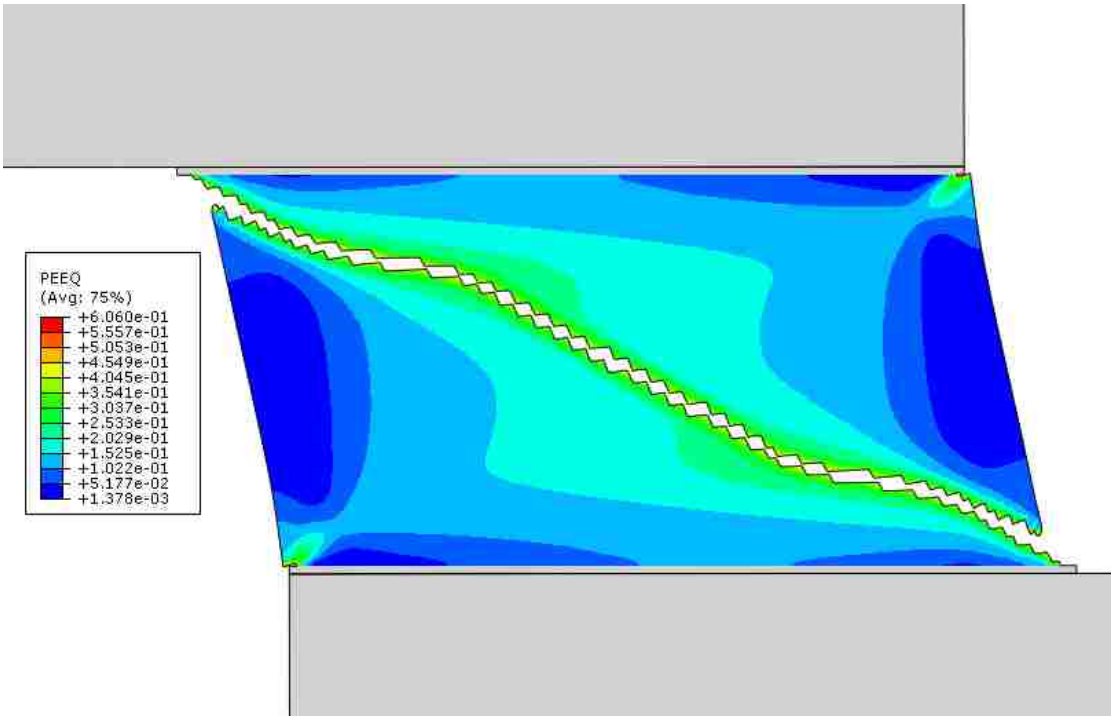

(e)

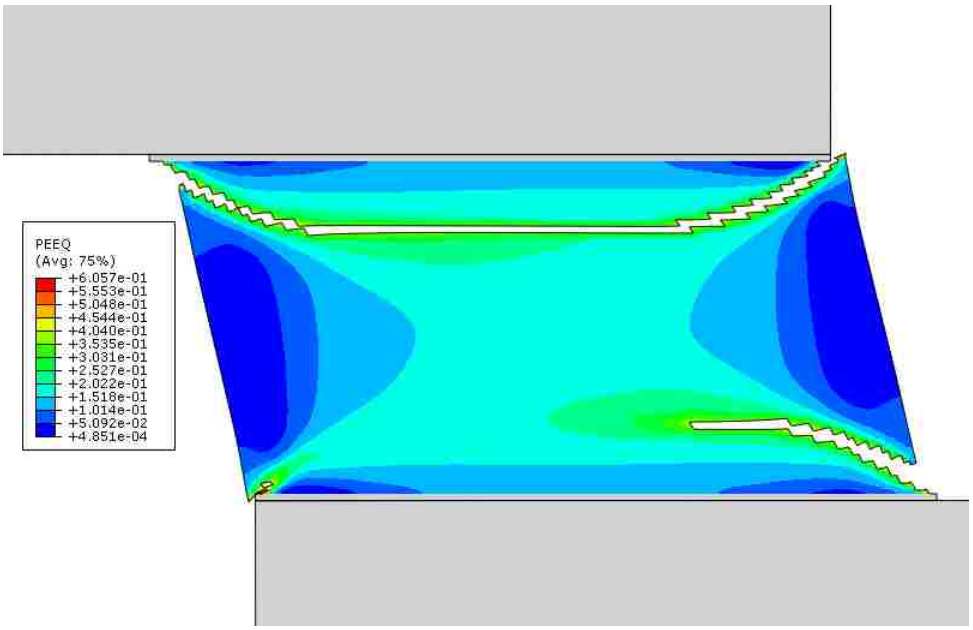

(f)

Fig. 4.9 Failure modes for various superimposed tensile/shear deformation ratios.

It is worth mentioning that the superimposed tension not only affects the apparent failure mode but the overall stress-strain response in shear is also affected. An example is shown in Fig. 4.10 where the shear stress-shear strain curves are shown for the case of the 1 s^{-1} shear strain rate with the tension/shear ratios of 0, 1/20, 1/10, 1/5 and 1/1. When the tension contribution is relatively large, the damage portion of the curve shows a less steep drop in shear stress. The ductility for the case of a tension/shear ratio of 1/1 is significantly smaller than the other cases.

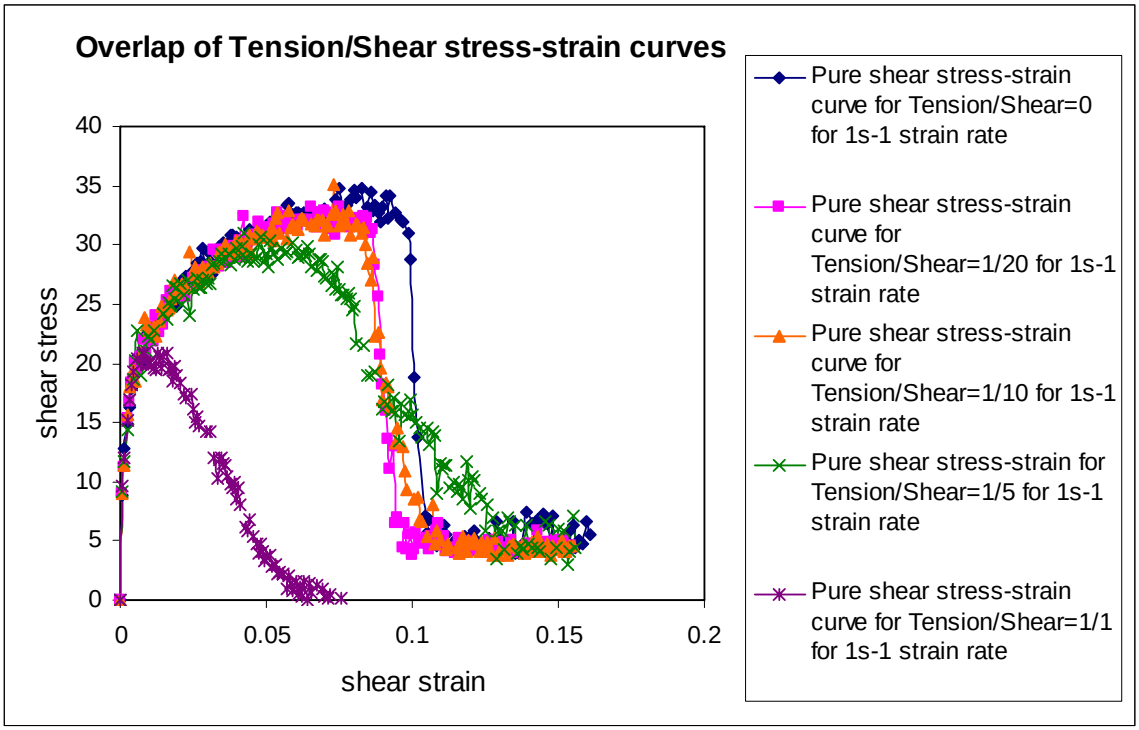

Fig.4.10 Shear stress-shear strain curves resulting from the loading with 1 s^{-1} shear strain rate, with different extents of tension superimposed.

4.3 Shear Loading with Superimposed Compression

We now address the case of superimposed compression. As in Section 4.2, the dominant failure modes for the various combinations of shear strain rate and compressive strain rate are summarized in Table 4.3. Here the same strain rate values and ratios as in the case of tension are considered. In general, a similar type of behavior is seen. The only difference between the results in Tables 4.2 and 4.1 is that, at a shear strain rate of 100 s^{-1} and the compression/shear ratio of 1/10, the failure mode is shear but in Table 4.1 the corresponding mode is tension.

Table 4.2 Dominant failure mode ("compression" or "shear") observed from the finite element simulation. For each shear strain rate, four different ratios of compressive strain rate/shear strain rate are considered.

Shear strain rate(s^{-1})	Compression/ Shear (1/1)	Compression/ Shear(1/5)	Compression/ Shear (1/10)	Compression/ Shear (1/20)
1	Compression	Shear	Shear	Shear
10	Compression	Compression	Shear	Shear
100	Compression	Compression	Shear	Shear

Figures 4.11(a)-(f) show the contour plots of equivalent plastic strain, shortly after complete failure of the joint, for the following cases:

(a) shear strain rate 1 s^{-1}, compression/shear ratio 1/1,

(b) shear strain rate 1 s^{-1}, compression/shear ratio 1/5,

(c) shear strain rate 10 s^{-1}, compression/shear ratio 1/5,

(d) shear strain rate 10 s^{-1}, compression/shear ratio 1/10,

(e) shear strain rate 100 s^{-1}, compression/shear ratio 1/5, and

(f) shear strain rate 100 s^{-1}, compression/shear ratio 1/10.

As in Section 4.3 above, these six cases correspond to the strain rate conditions across the "boundary" between the compression modes (red) and shear mode (blue) in Table 4.2. Similar to the case of Fig. 4.9, Fig. 4.11 shows that the failure mode appears in a distinct manner: either the compression mode or the shear mode with no ambiguity (although the loading has both the compression and shear components).

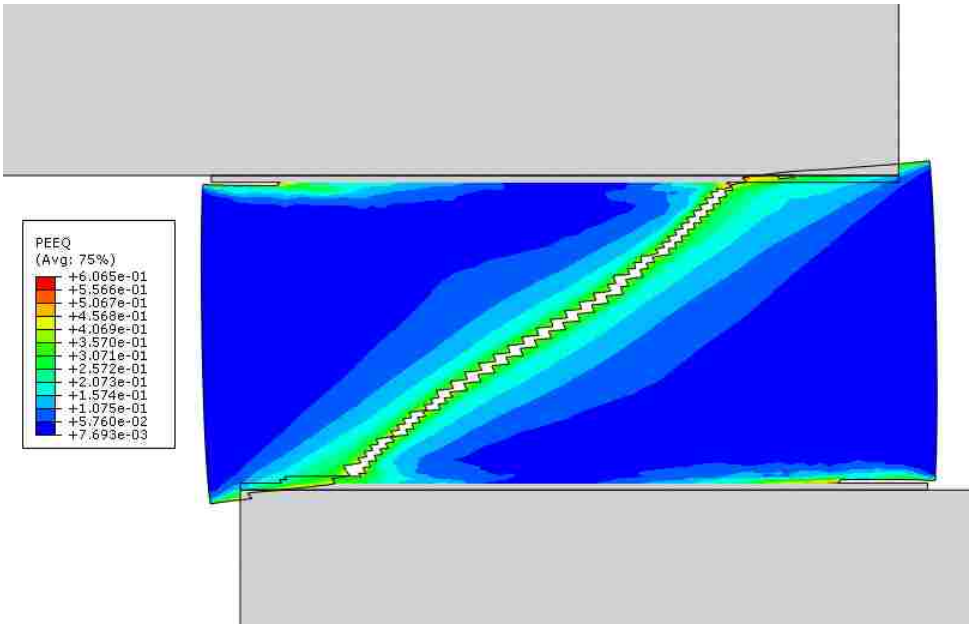
PEEQ
(Avg: 75%)
+6.065e-01
+5.566e-01
+5.067e-01
+4.568e-01
+4.069e-01
+3.570e-01
+3.071e-01
+2.572e-01
+2.073e-01
+1.574e-01
+1.075e-01
+5.760e-02
+7.693e-03

(a)

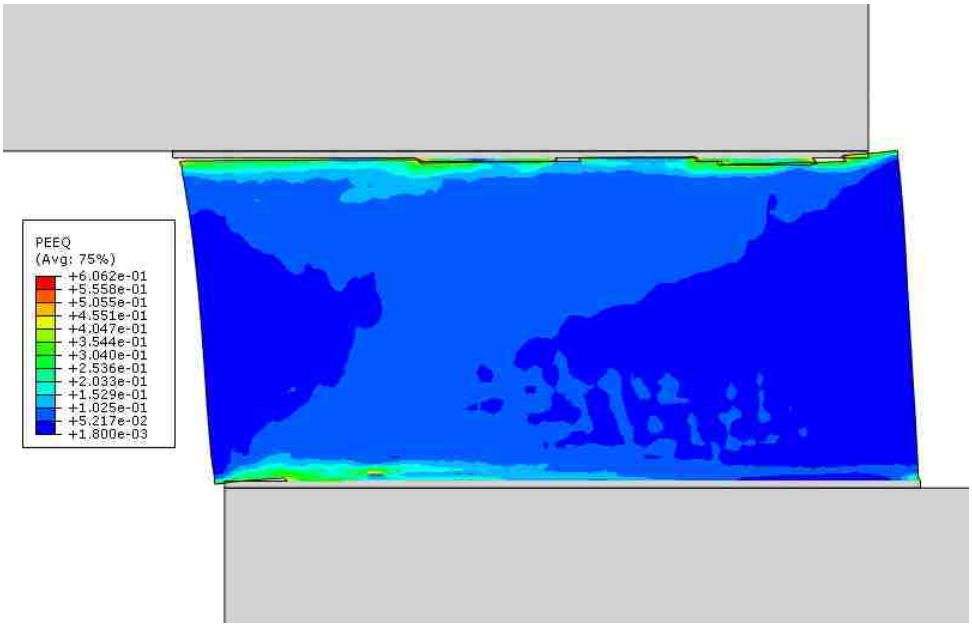
PEEQ
(Avg: 75%)
+6.062e-01
+5.558e-01
+5.055e-01
+4.551e-01
+4.047e-01
+3.544e-01
+3.040e-01
+2.536e-01
+2.033e-01
+1.529e-01
+1.025e-01
+5.217e-02
+1.800e-03

(b)

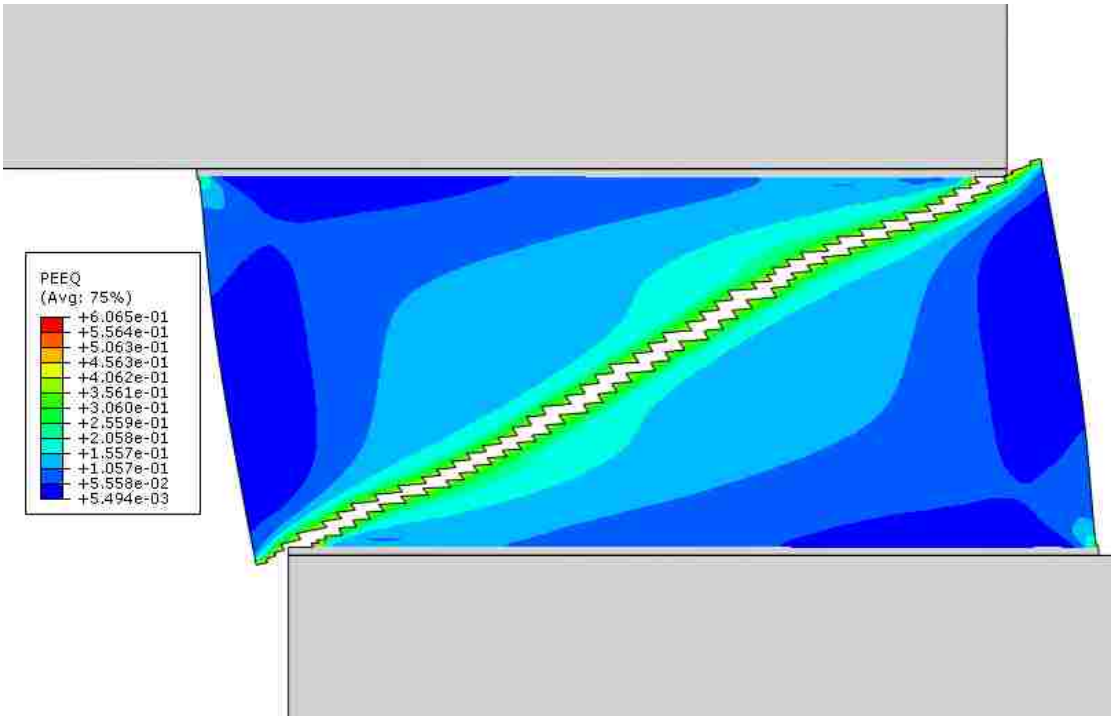
PEEQ
(Avg: 75%)
+6.065e-01
+5.564e-01
+5.063e-01
+4.563e-01
+4.062e-01
+3.561e-01
+3.060e-01
+2.559e-01
+2.058e-01
+1.557e-01
+1.057e-01
+5.558e-02
+5.494e-03

(c)

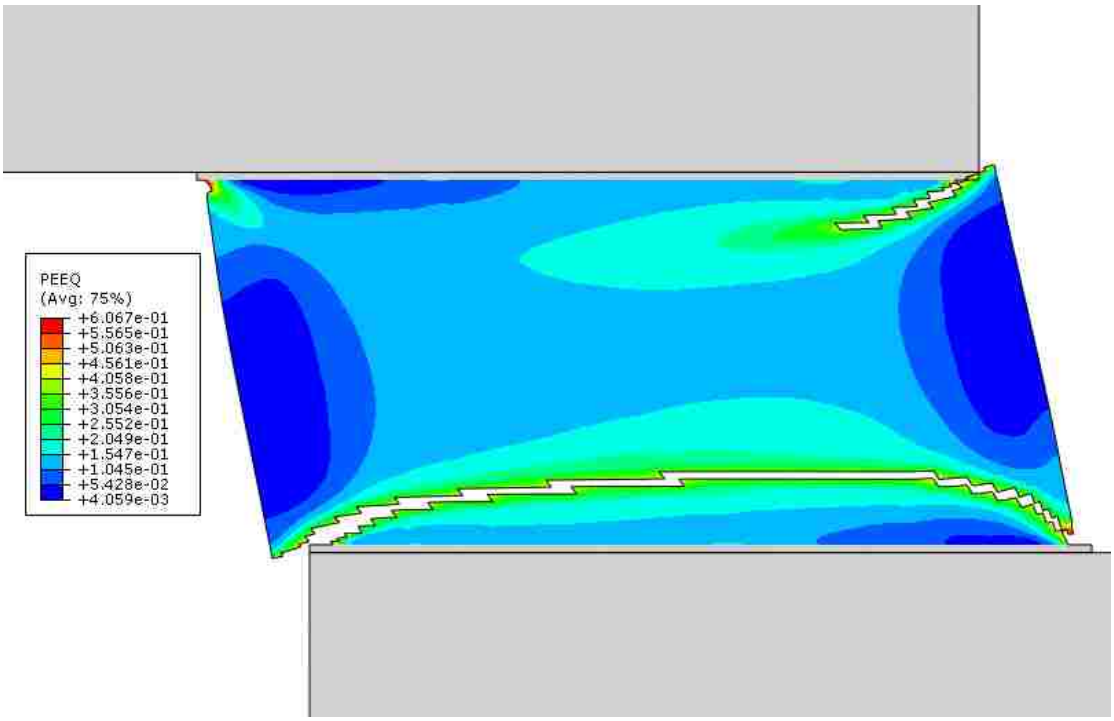
PEEQ
(Avg: 75%)
+6.067e-01
+5.565e-01
+5.063e-01
+4.561e-01
+4.058e-01
+3.556e-01
+3.054e-01
+2.552e-01
+2.049e-01
+1.547e-01
+1.045e-01
+5.428e-02
+4.059e-03

(d)

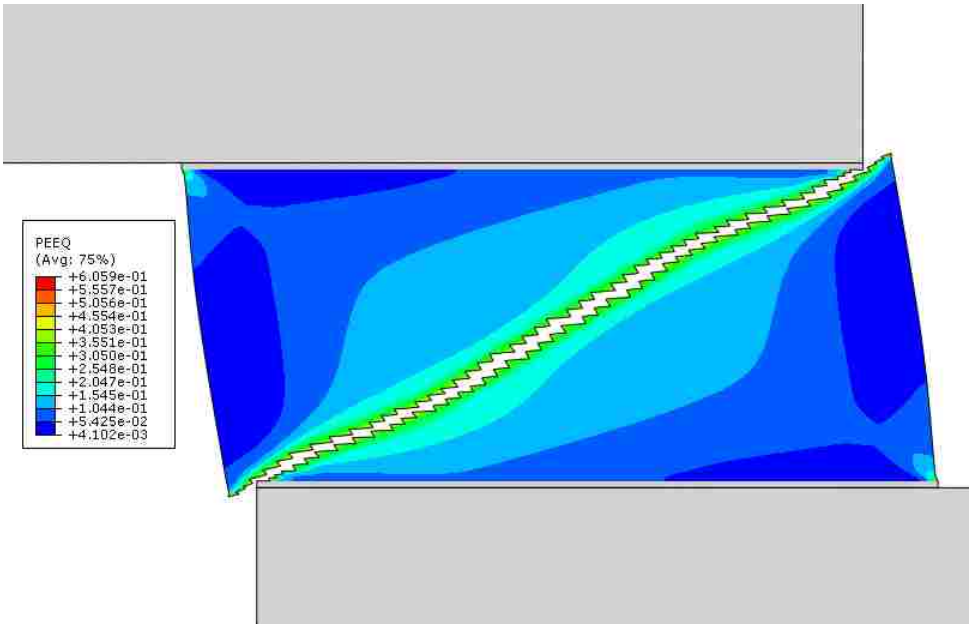

(e)

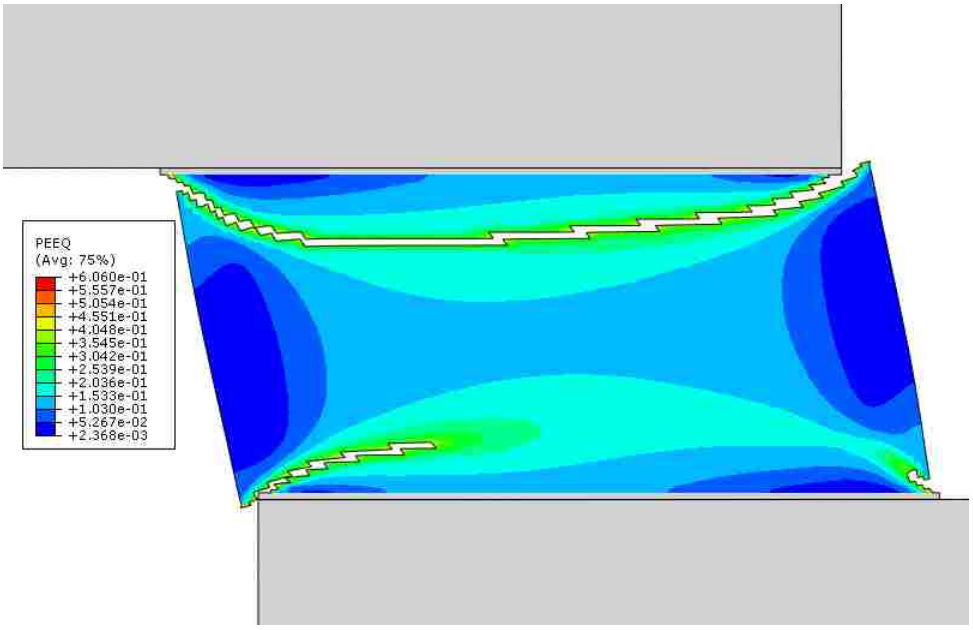

(f)

Fig. 4.11. Failure modes for various superimposed compression/shear deformation ratios.

As in the case of superimposed tension, the overall stress-strain curve in shear is also affected by the superimposed compression. An example is shown in Fig. 4.12 where the shear stress-shear strain curves are shown for the case of the 1 s^{-1} shear strain rate with the compression/shear ratios of 0, 1/20,1/10, 1/5 and 1/1. Similar to the case of superimposed tension, the curves of the compression/shear ratios of 1/1 and 1/5 are affected most. There is a significant reduction in ductility when the tension/shear ratio is 1/1.

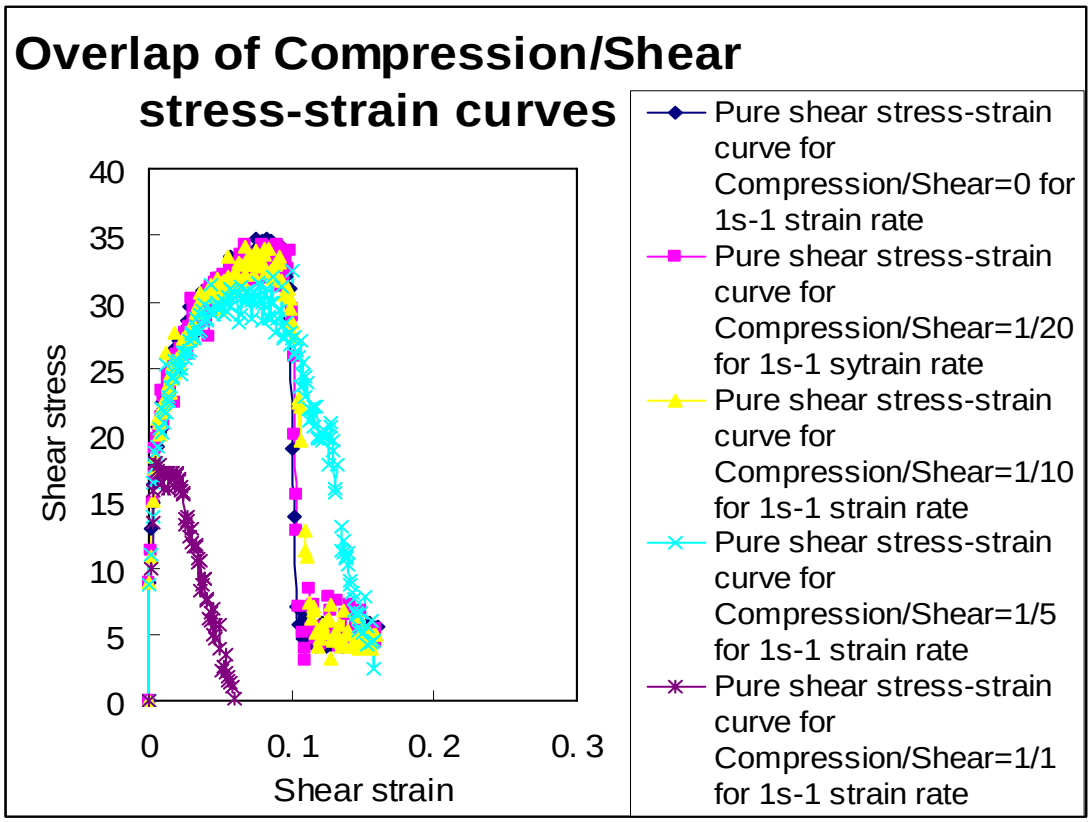

Fig.4.12 Shear stress-shear strain curves resulting from the loading with 1 s^{-1} shear strain rate, with different extents of compression superimposed.

4.4 Comparison with Experiments

Experimental studies correlating the shear strain rate and failure pattern in solder, under the high rate conditions as considered in this study, are not available in a systematic format. The correlation will also depend on the actual loading mode, loading history, mechanical properties (which in turn depend on the composition and microstructure of the solder alloy), the three-dimensional geometry of the joint and the detailed design of bond pad and peripheral structures in real devices. Nevertheless, the failure features presented in Chapters 3 and 4 are commonly observed in experiments when the intermetallic layers themselves are sufficiently strong. Representative experimental photographs showing solder failure under fast loading are shown in Fig. 4.13(a)-(d).

(a) Cross section of corner solder interconnect in the failed samples to fail at the package-to-solder interconnect interface

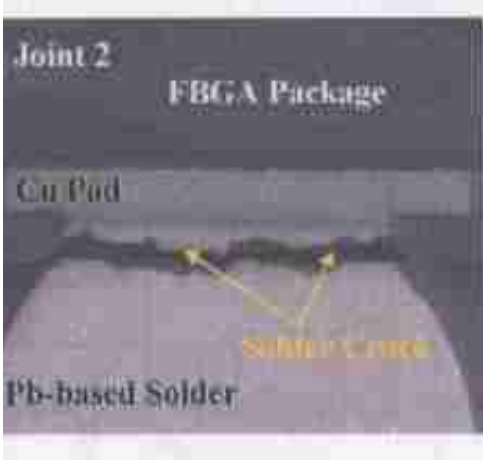

(b) Cracks and failures found in the solder joint system-Pb-based on Organic Solderability Preservative (OSP).

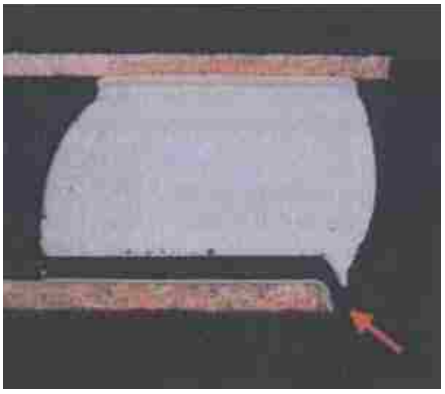

(c) Board side solder fracture

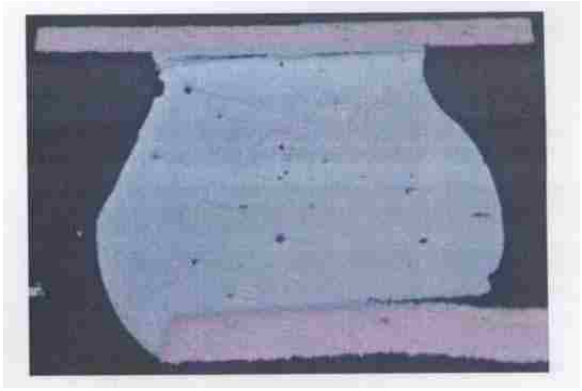

(d) ***95.5Sn4.0Ag0.5 Cu*** Solder interconnect failure at the package to-solder interface and at the solder-to-board interface.

Fig. 4.13 Experimental photographs showing solder failure under fast loading conditions. Parts (a), (b), (c) and (d) are taken from References [38], [39], [40] and [41], respectively.

4.5 Conclusions

On the basis of the presentation above, it can be concluded that ductile failure of the solder joint is very sensitive to the deformation mode. Under the constant strain rate conditions considered in this study, both the superimposed tension and compression can dramatically change the shear-induced failure morphology. With the tensile/compression strain rate (and thus strain) being a small fraction of the shear strain rate, the tension/compression failure mode becomes dominant. The overall ductility is significantly reduced when the superimposed tension/compression reaches 1/1. As a consequence, a large deviation from the pure shearing deformation under fast loading is seen to have a detrimental effect on the mechanical reliability of solder joints.

Chapter 5 Effects of Damage Parameters

In this chapter simulation results based on the second set of damage parameters ($\bar{\varepsilon}_0^{pl}$ = 0.54 and $\bar{u}_f^p$ = 9 μm) are presented. The primary objective is to examine if the more ductile material response (delayed damage) will result in fundamentally different failure characteristics in the solder joint. All the other modeling conditions are kept the same.

5.1 Pure Shear Loading

The case of simple shear loading is first considered. Figures 5.1(a)-(c) show the Mises effective stress, shear stress σ_{xy}, and the equivalent plastic strain at the nominal shear strain of 0.25, for the case of 1 s^{-1} shear strain rate. The corresponding contour plots for the cases of 10 s^{-1} and 100 s^{-1} strain rates are shown in Figs. 5.2 and 5.3, respectively. It can be seen that the magnitudes of Mises effective stress and the shear stress in the solder increase as the applied shear strain rate increases. The case of the slowest strain rate shows the largest area under very high equivalent plastic strain (comparing part (c) of the three figures). In Fig. 5.1(c) the banded deformation pattern is evident near the interface. The plastic strain fields in Figs. 5.2(c) and 5.3(c) are more diffuse, except near the corners.

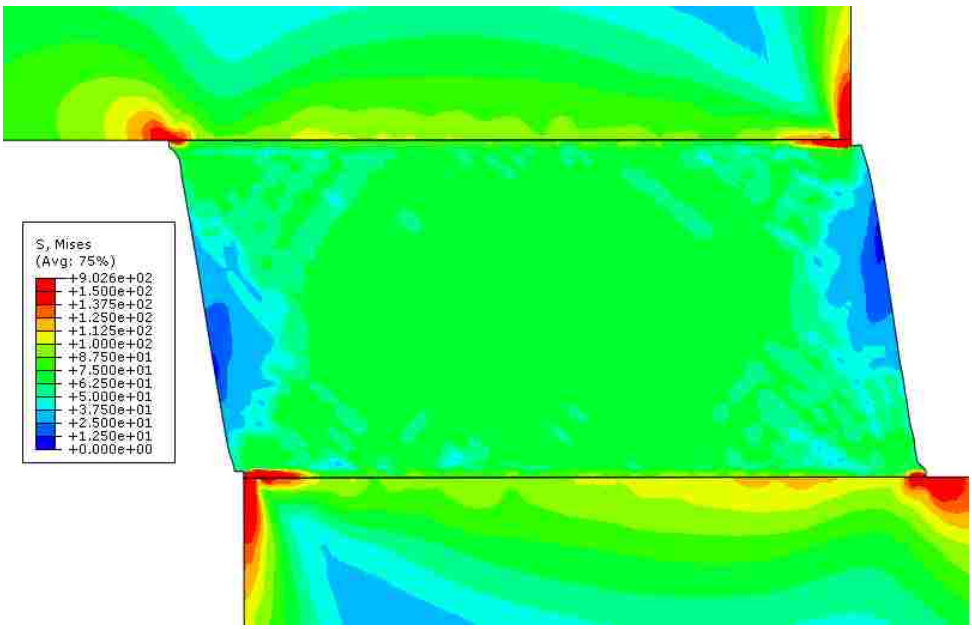
S, Mises
(Avg: 75%)
+9.026e+02
+1.500e+02
+1.375e+02
+1.250e+02
+1.125e+02
+1.000e+02
+8.750e+01
+7.500e+01
+6.250e+01
+5.000e+01
+3.750e+01
+2.500e+01
+1.250e+01
+0.000e+00

5.1 (a)

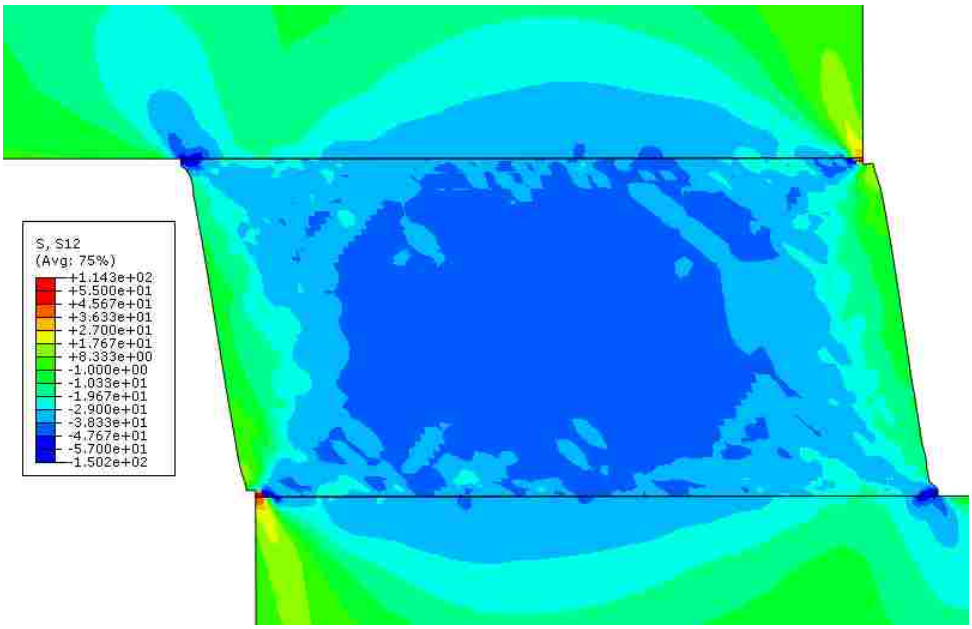
S, S12
(Avg: 75%)
+1.143e+02
+5.500e+01
+4.567e+01
+3.633e+01
+2.700e+01
+1.767e+01
+8.333e+00
-1.000e+00
-1.033e+01
-1.967e+01
-2.900e+01
-3.833e+01
-4.767e+01
-5.700e+01
-1.502e+02

5.1 (b)

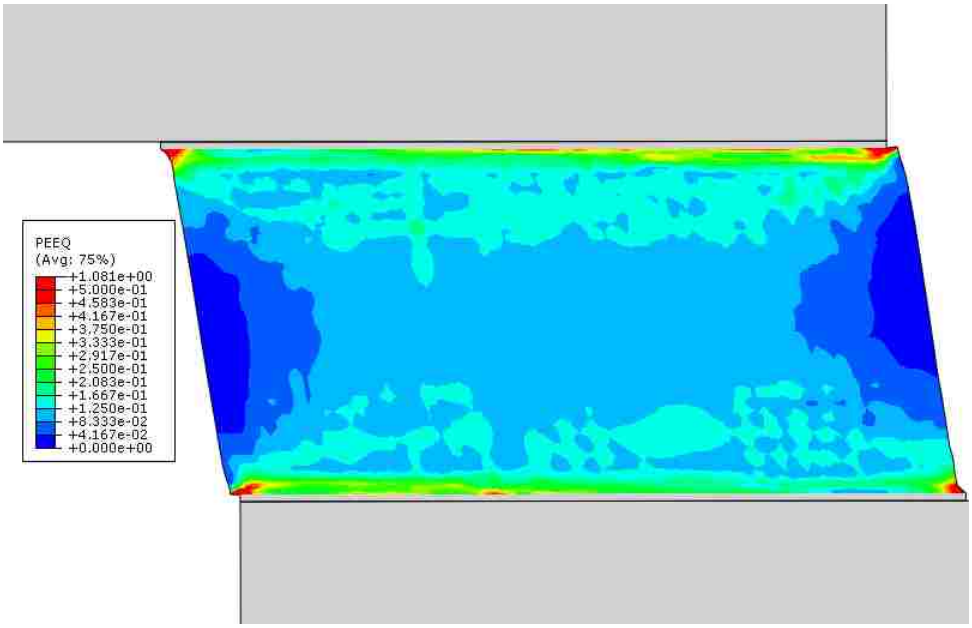

5.1 (c)

Fig. 5.1 Contour plots showing (a) von Mises effective stress, (b) Shear stress and (c) equivalent plastic strain corresponding to the nominal shear strain of 0.25, in the case of $1s^{-1}$ shear strain rate.

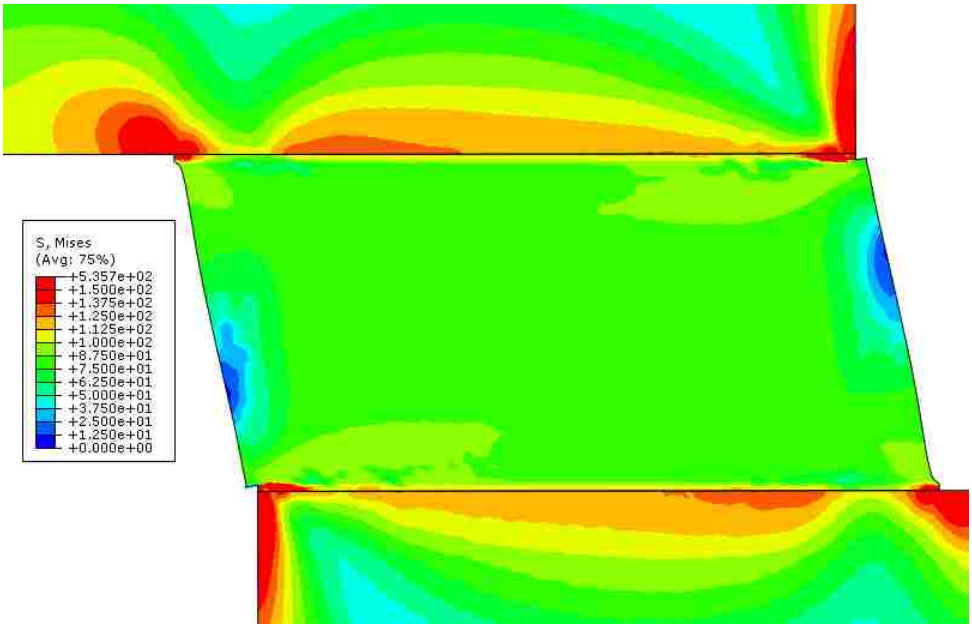
S, Mises
(Avg: 75%)
+5.357e+02
+1.500e+02
+1.375e+02
+1.250e+02
+1.125e+02
+1.000e+02
+8.750e+01
+7.500e+01
+6.250e+01
+5.000e+01
+3.750e+01
+2.500e+01
+1.250e+01
+0.000e+00

5.2 (a)

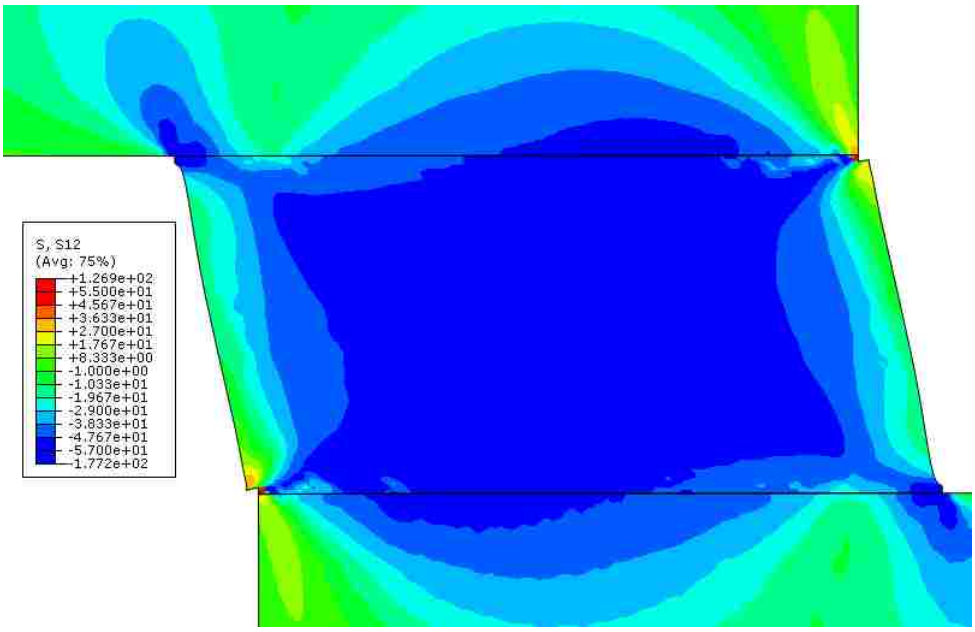
S, S12
(Avg: 75%)
+1.269e+02
+5.500e+01
+4.567e+01
+3.633e+01
+2.700e+01
+1.767e+01
+8.333e+00
-1.000e+00
-1.033e+01
-1.967e+01
-2.900e+01
-3.833e+01
-4.767e+01
-5.700e+01
-1.772e+02

5.2 (b)

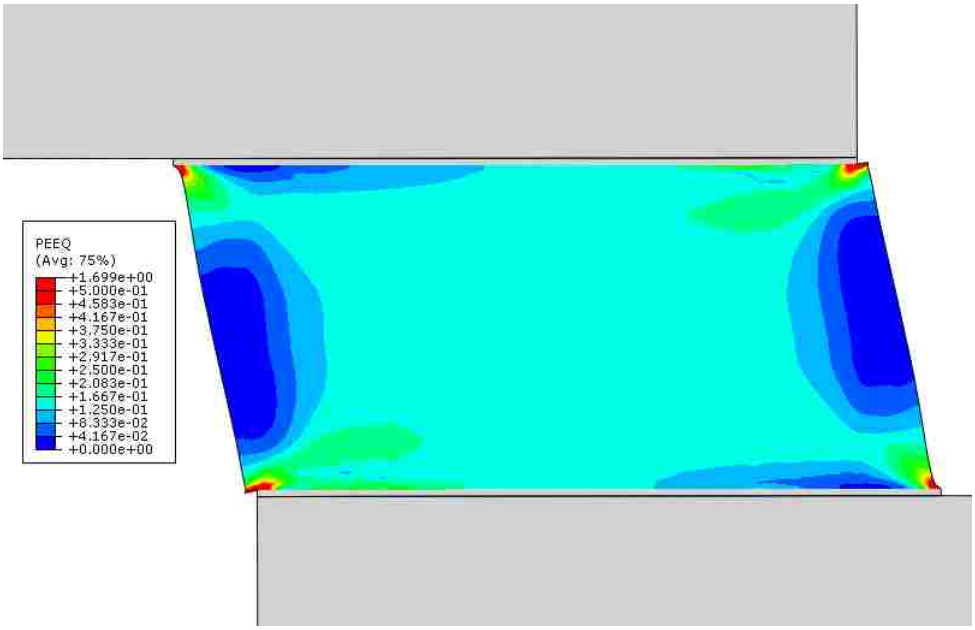

5.2 (c)

Fig.5.2. Contour plots showing (a) von Mises effective stress, (b) shear stress and (c) equivalent plastic strain corresponding to the nominal shear strain of 0.25, in the case of $10s^{-1}$ shear strain rate

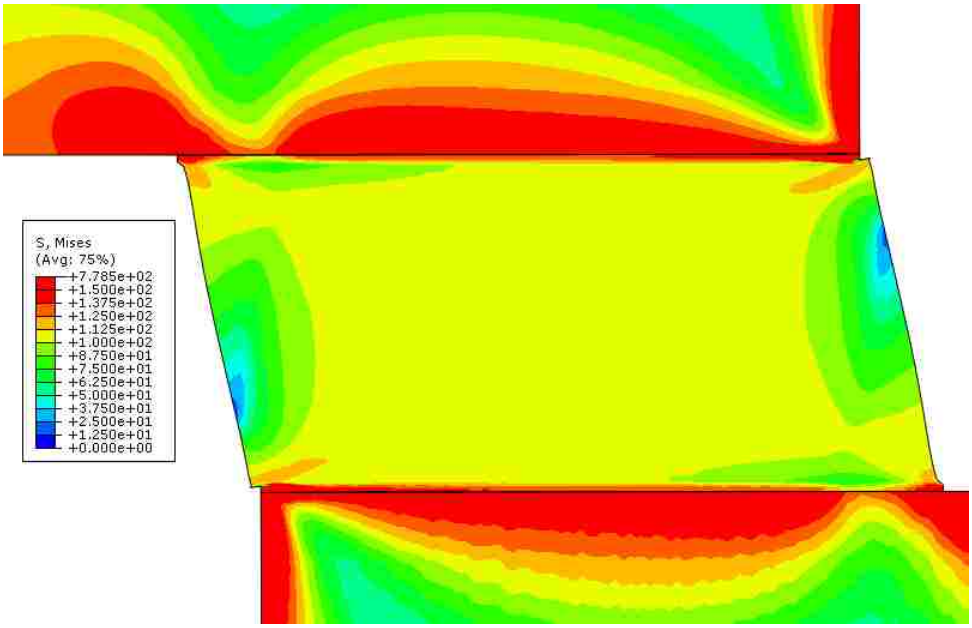
S, Mises
(Avg: 75%)
+7.785e+02
+1.500e+02
+1.375e+02
+1.250e+02
+1.125e+02
+1.000e+02
+8.750e+01
+7.500e+01
+6.250e+01
+5.000e+01
+3.750e+01
+2.500e+01
+1.250e+01
+0.000e+00

5.3 (a)

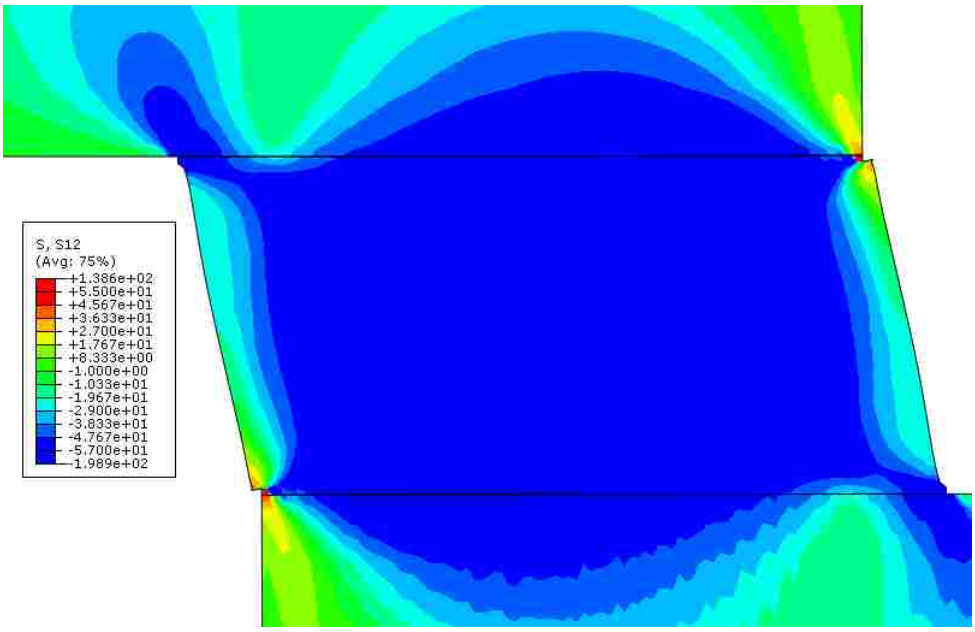
S, S12
(Avg: 75%)
+1.386e+02
+5.500e+01
+4.567e+01
+3.633e+01
+2.700e+01
+1.767e+01
+8.333e+00
-1.000e+00
-1.033e+01
-1.967e+01
-2.900e+01
-3.833e+01
-4.767e+01
-5.700e+01
-1.989e+02

5.3 (b)

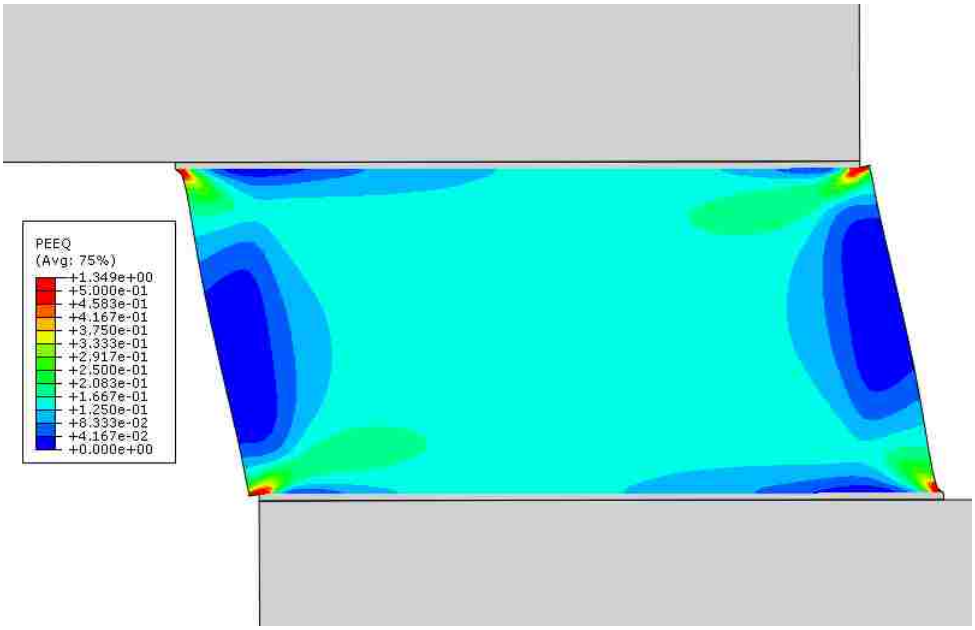

5.3(c)

Fig.5.3. Contour plots showing (a) von Mises effective stress, (b) shear stress and (c) equivalent plastic strain corresponding to the nominal shear strain of 0.25, in the case of 100s^{-1} shear strain rate

Figures 5.4(a) and (b) show the contour plots of equivalent plastic strain along with the failure (removed elements), at the early stage of the cracking process and upon final failure, respectively, for the case of 1 s^{-1} strain rate. The corresponding plots for the cases of 10 s^{-1} and 100 s^{-1} strain rates are shown in Figs. 5.5 and 5.6, respectively. It is apparent that, with the damage parameters used in the current chapter, cracking starts when the overall deformation is much greater compared to that in the previous chapters. In the case of slowest strain rate, failure appears along or very close to the interface between the solder and intermetallic (Fig. 5.4(b)). For larger strain rates, an "angled" failure path is seen (Figs. 5.5(b) and 5.6(b)), with cracking close to the interface near only one corner. Here cracking initiates from one corner and stays dominant during its propagation. Subsequent damage is localized at the crack tip until the entire joint is severed. Note in Chapter 3 (specifically Figs. 3.6 and 3.7), that the final fracture was caused by the linking of cracks initiating from the two corners. Despite this main difference, it is worth noting again that the cases of 10 s^{-1} and 100 s^{-1} strain rates in the current chapter still result in a fundamentally different failure morphology compared to that of 1 s^{-1}. This tendency is qualitatively the same as that in Chapter 3.

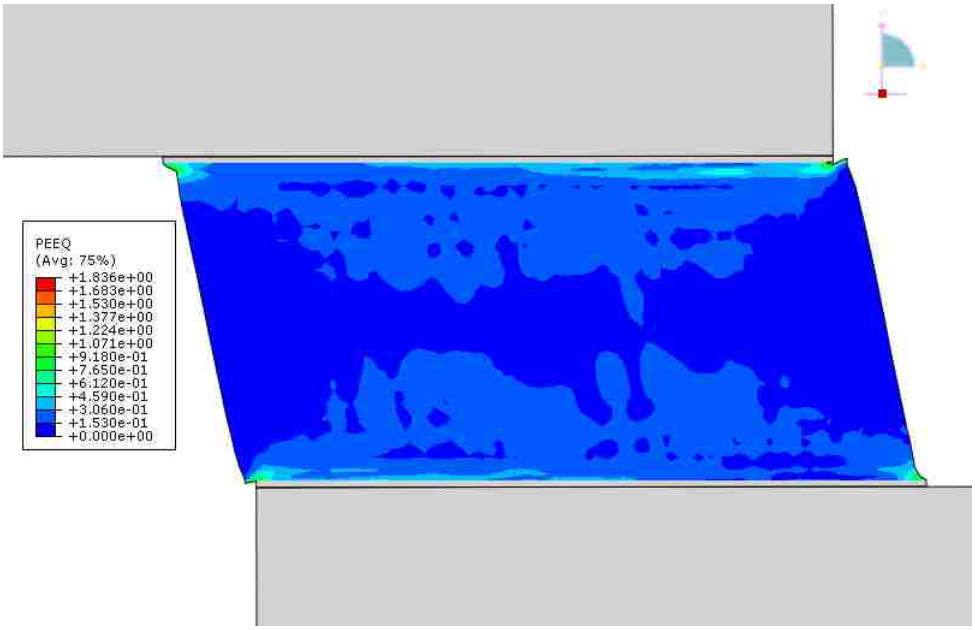

5.4 (a)

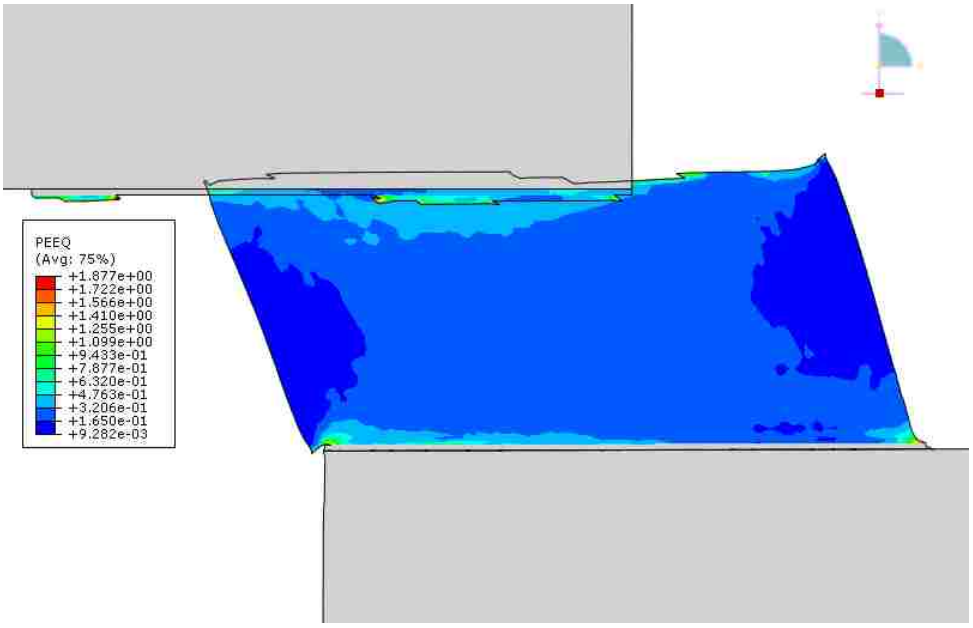

5.4 (b)

Fig.5.4. Contours of equivalent plastic strain for the case of 1s^{-1} strain rate (a) shortly after cracking begins and (b) shortly after complete failure of the joint.

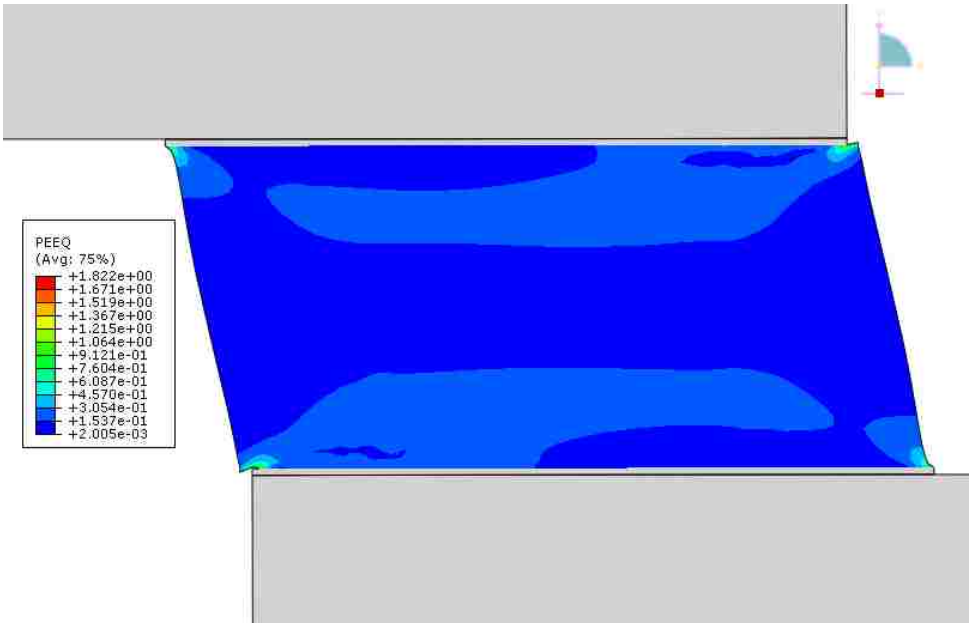

5.5(a)

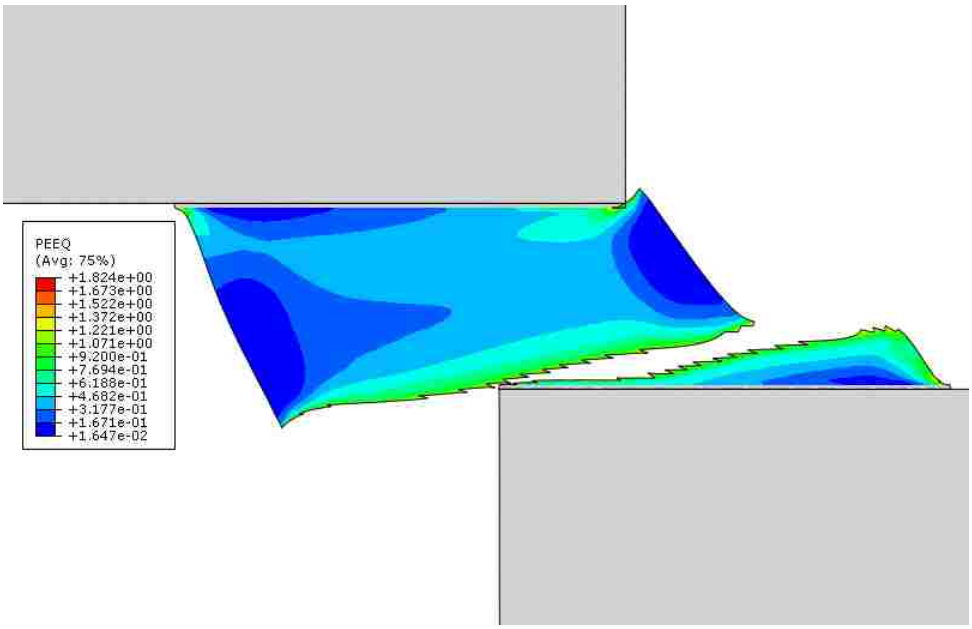

5.5 (b)

Fig.5.5. Contours of equivalent plastic strain for the case of $10s^{-1}$ strain rate (a) shortly after cracking begins and (b) shortly after complete failure of the joint.

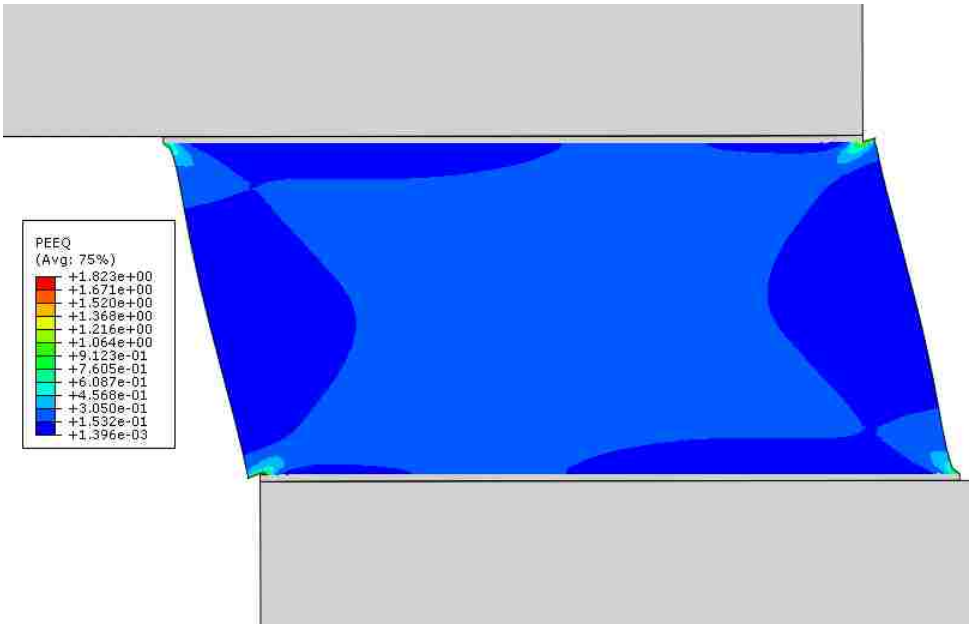

5.6 (a)

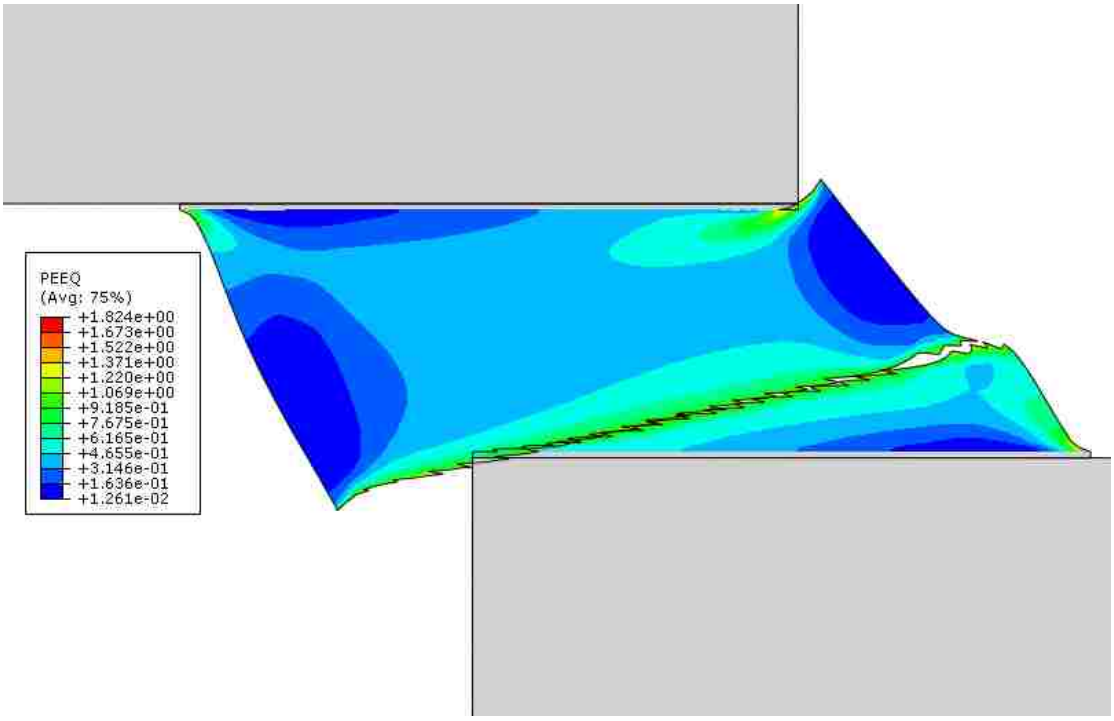

5.6 (b)

Fig.5.6. Contours of equivalent plastic strain for the case of 100s^{-1} strain rate (a) shortly after cracking begins and (b) shortly after complete failure of the joint.

5.2 Pure Tensile and Compressive Deformation

We now present the pure tension and pure compression results, for gaining a basic understanding of the effects of the damage parameters. Figures 5.7-5.9 show the contour plots of equivalent plastic strain with the cracking pattern for the nominal tensile strain rates of 1 s^{-1}, 10 s^{-1} and 100 s^{-1}, respectively. Parts (a) and (b) in these figures correspond to the stages shortly after crack initiation and shortly after final failure, respectively. Due to the present damage parameters, failure occurs when the tensile strain is much greater compared to the cases in Figs. 4.1-4.3. It can be seen that, in Fig. 5.7, cracks first appear along the interface between the solder and the intermetallic, but they soon link up along the near 45º direction. The failure mode in Figs. 5.8 and 5.9 is similar, except that the interface part of the failure is of a much smaller scale. In general, the qualitative failure features observed here is the same as those in Chapter 4.

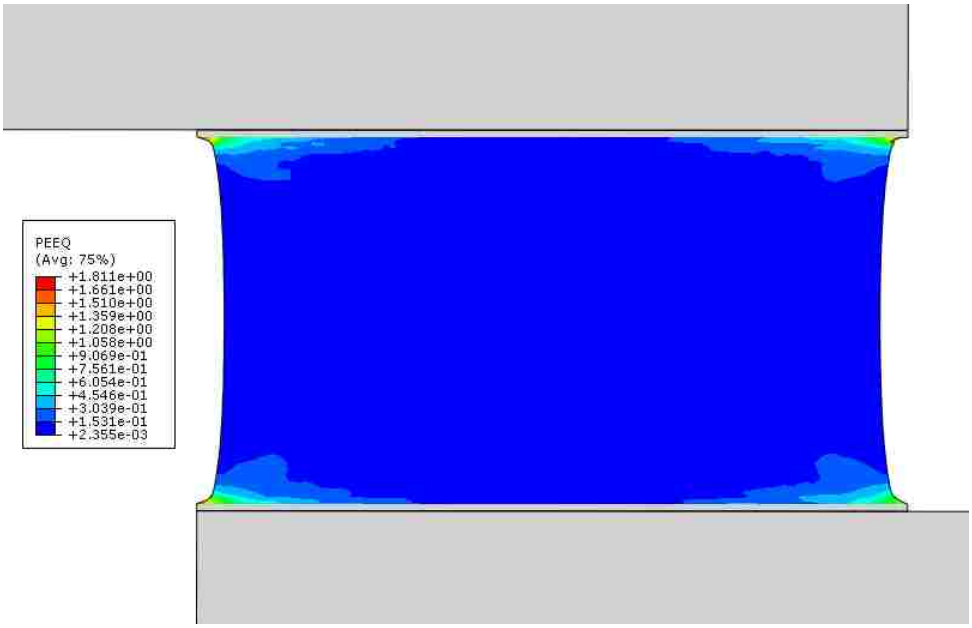

5.7 (a)

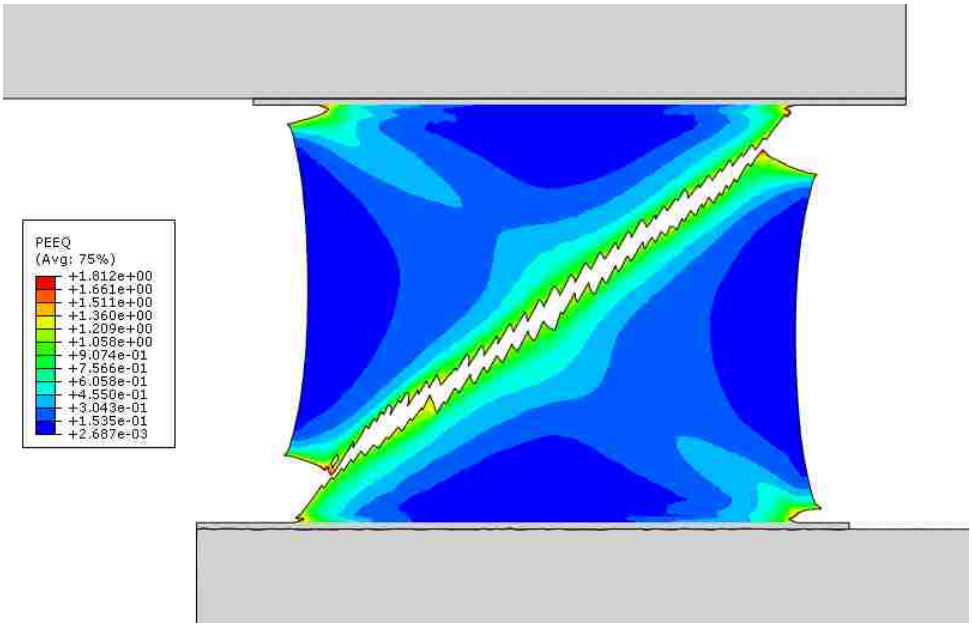

5.7 (b)

Fig.5.7.Contour plots of pure tensile deformation showing the equivalent plastic strain for the case of $1s^{-1}$ strain rate.

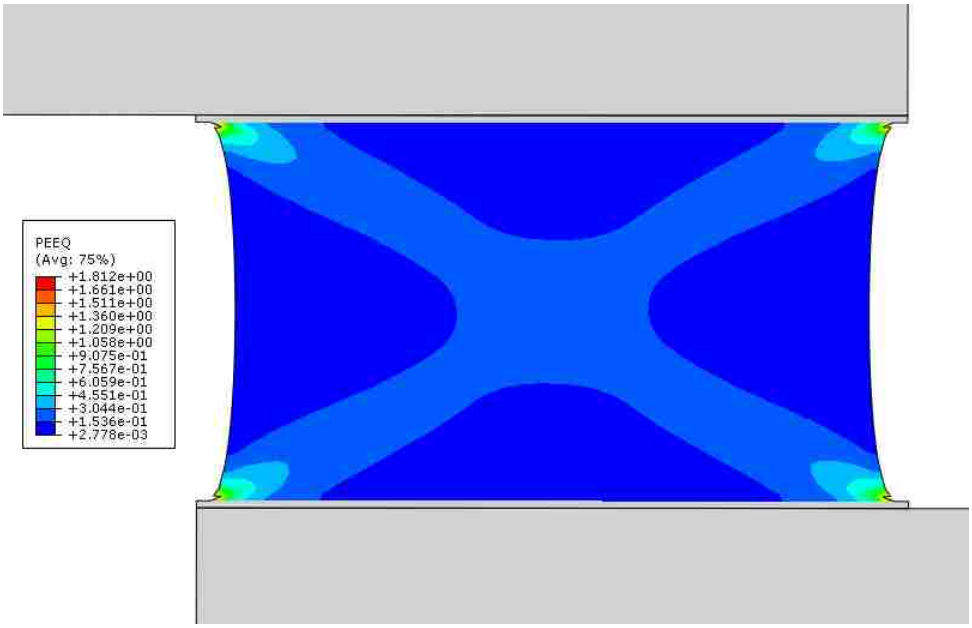

5.8 (a)

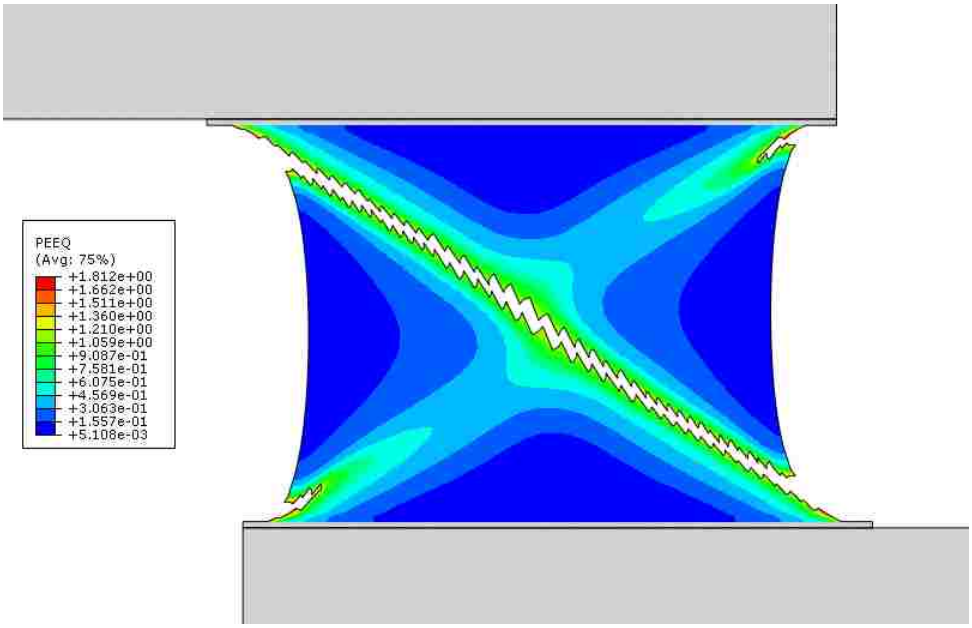

5.8 (b)

Fig. 5.8. Contour plots of pure tensile deformation showing the equivalent plastic strain for the case of $10s^{-1}$ strain rate.

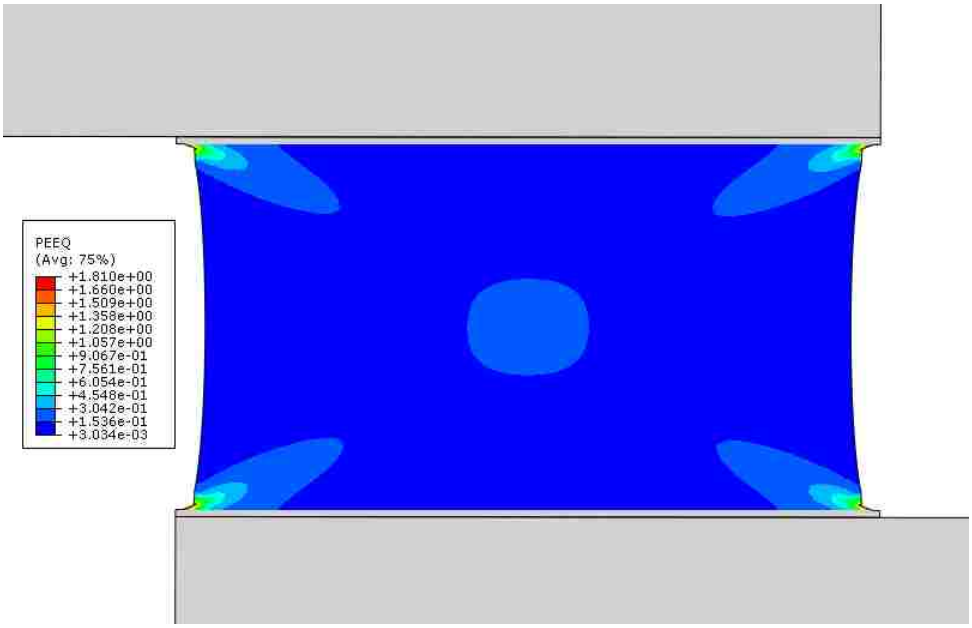

5.9 (a)

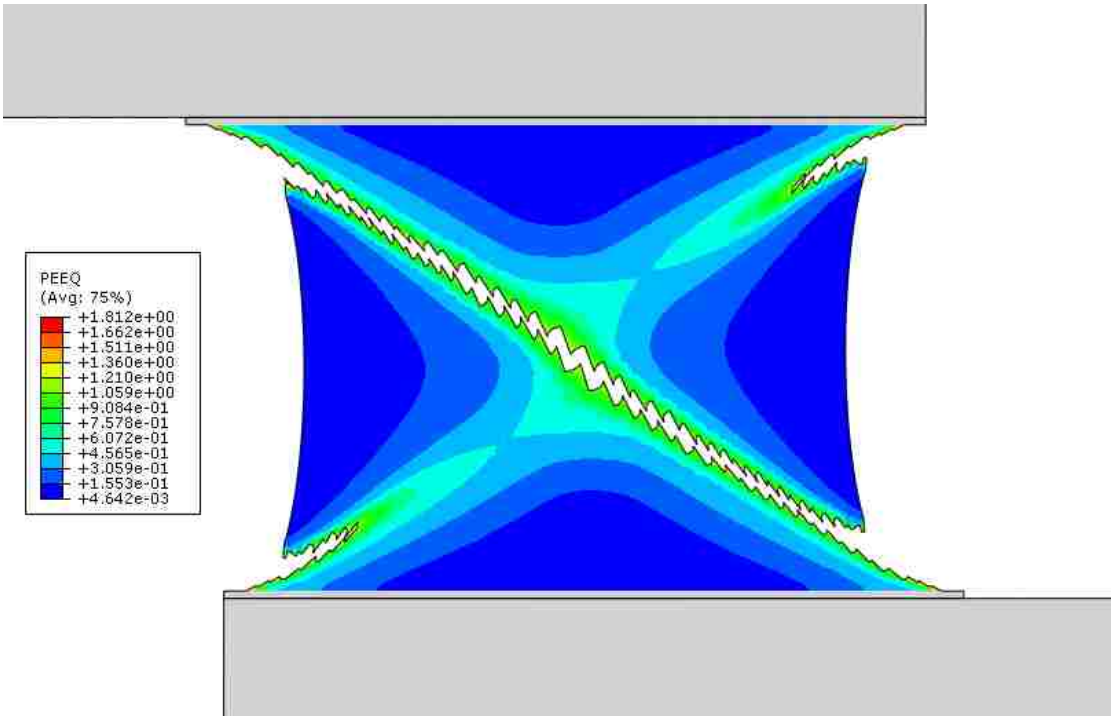

5.9 (b)

Fig.5.9. Contour plots of pure tensile deformation showing the equivalent plastic strain for the case of 100s^{-1} strain rate.

Next we consider the case of pure compression. Figures 5.10-5.12 show the results of pure compressive deformation for the nominal compressive strain rates of 1 s^{-1}, 10 s^{-1} and 100 s^{-1}, respectively. As in the case of tension, parts (a) and (b) in these figures correspond to the deformed configurations shortly after crack initiation and after final failure, respectively. Similar general features as in the case of tension can be seen. There is a decreasing tendency for initial cracking along the interface as the applied strain rate increases. Final fracture takes the path of near 45º direction in all cases. Note also that the overlapping of materials after complete failure seen in the figures is unphysical and should be ignored. In general, the delayed damage model considered in the current chapter results in qualitatively the same compressive failure behavior as observed in Chapter 4.

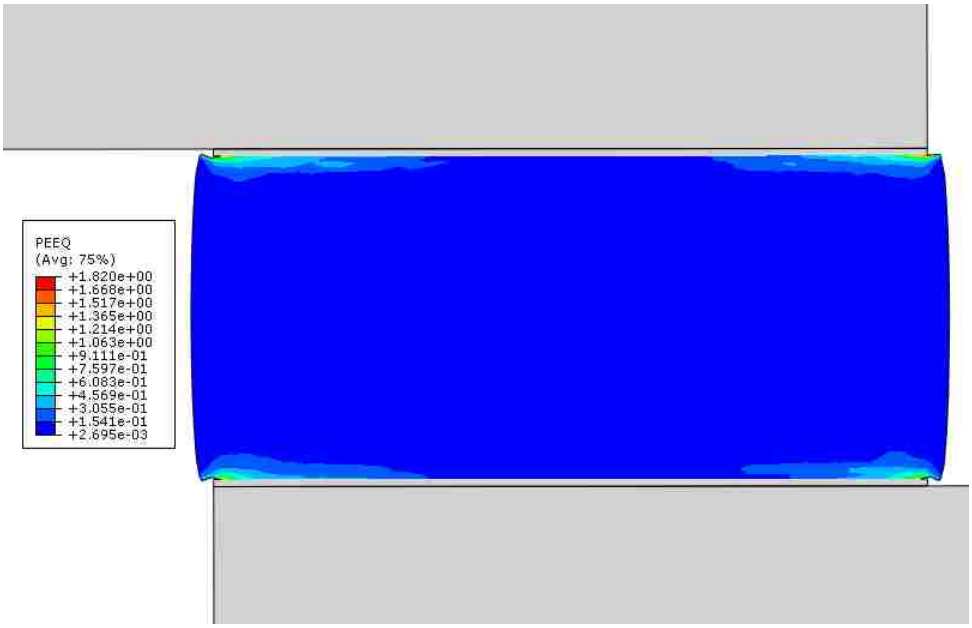

5.10. (a)

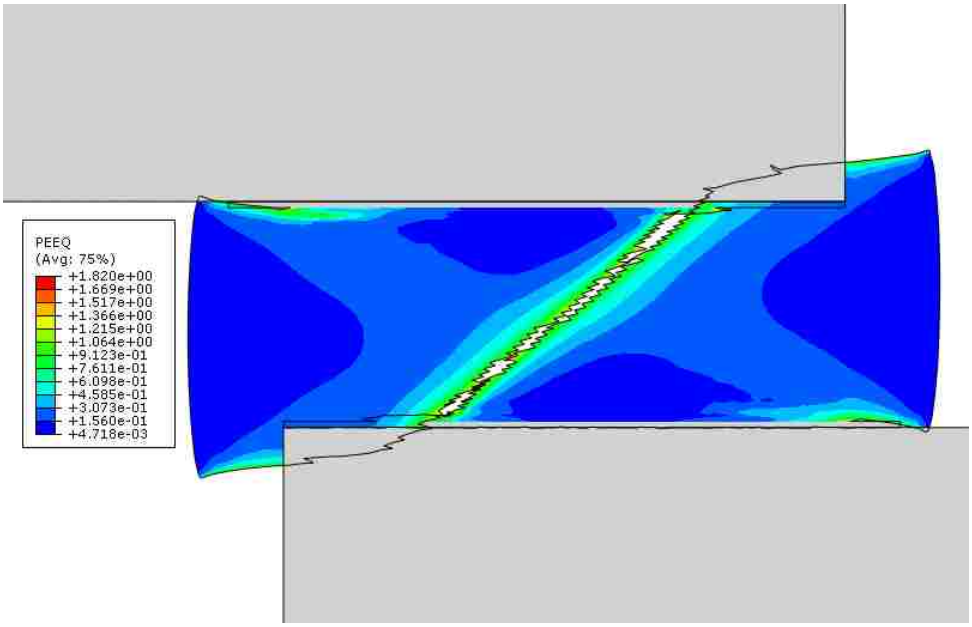

5.10 (b)

Fig.5.10. Contour plots of pure compressive deformation showing the equivalent plastic strain for the case of $1s^{-1}$ strain rate

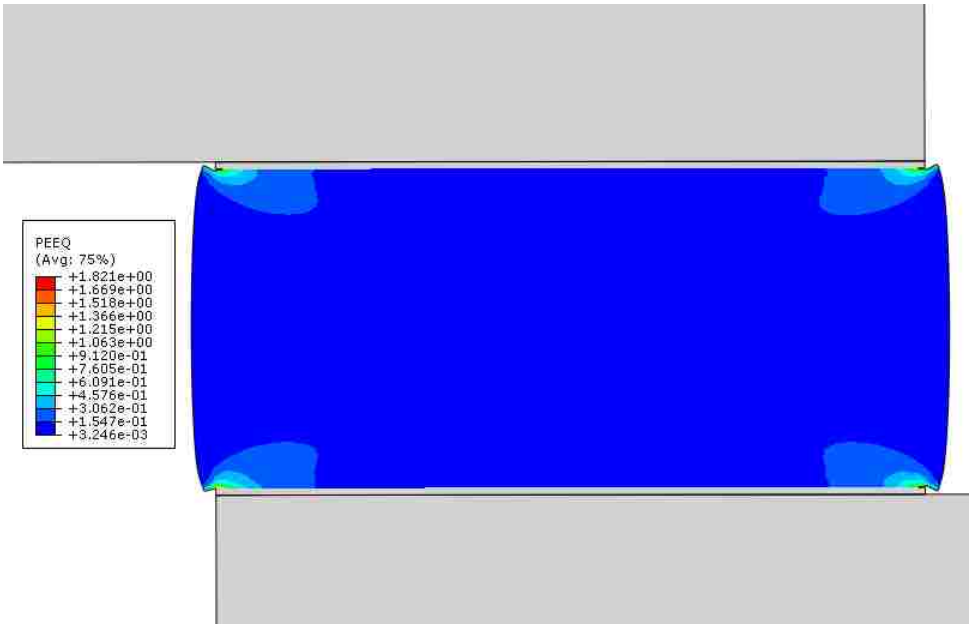

5.11 (a)

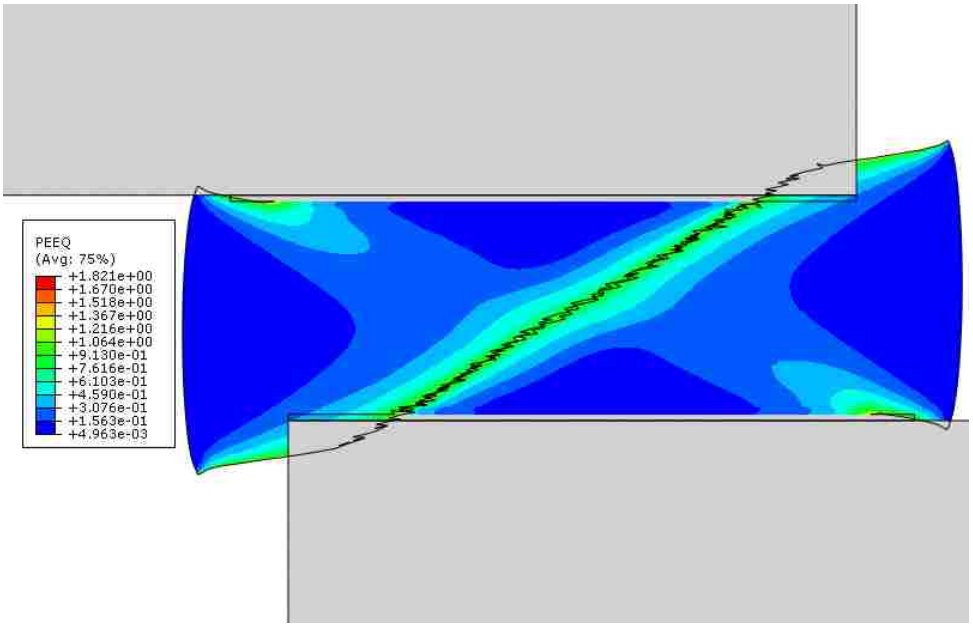

5.11 (b)

Fig.5.11. Contour plots of pure compressive deformation showing the equivalent plastic strain for the case of 10s^{-1} strain rate

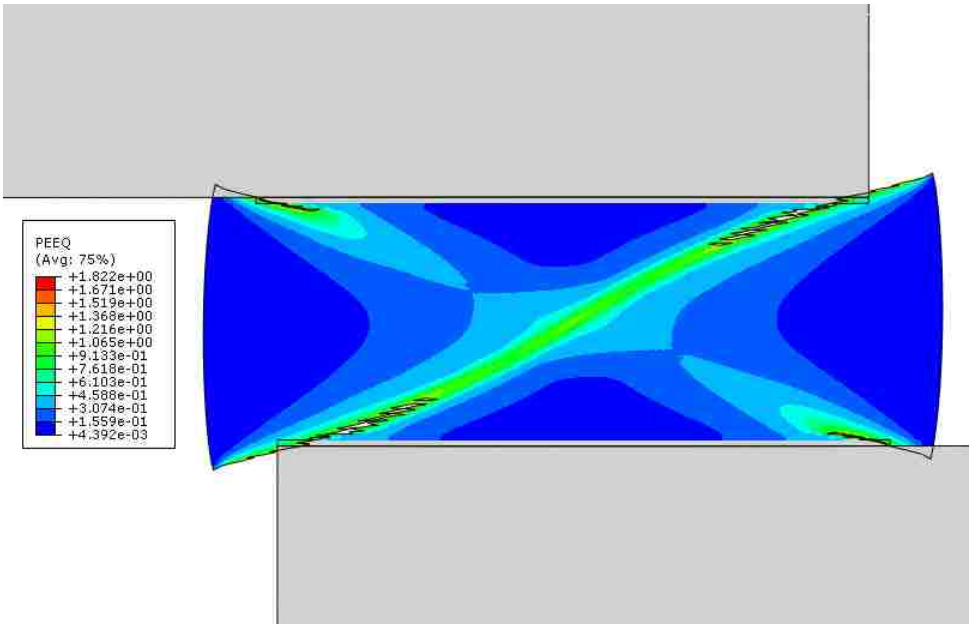

5.12 (a)

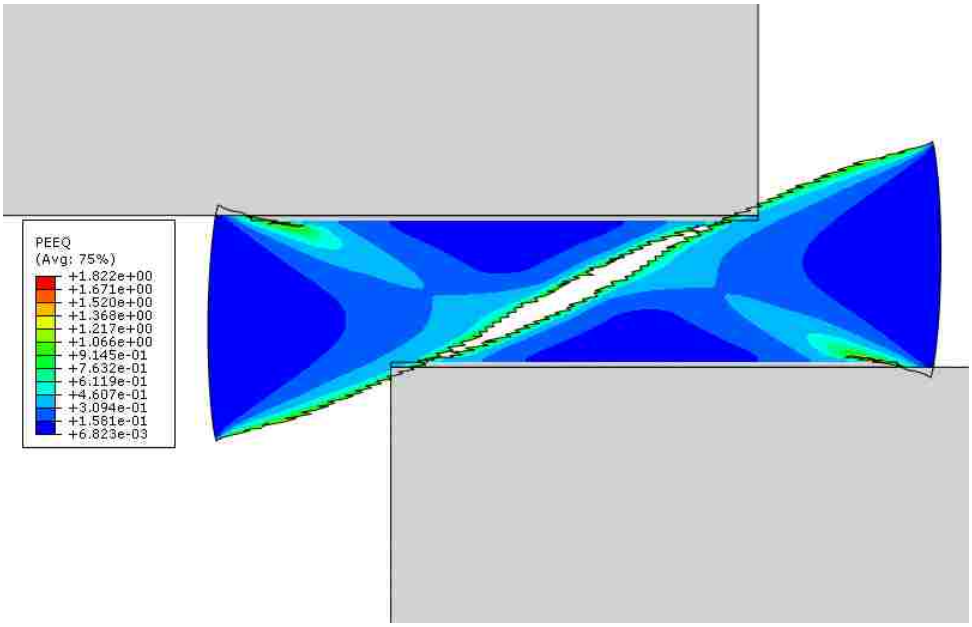

5.12 (b)

Fig.5.12. Contour plots of pure compressive deformation showing the equivalent plastic strain for the case of 100s^{-1} strain rate

5.3 Shear Loading with Superimposed Tension

In this section, we follow the same format as in Section 4.2 to examine how the superimposed tension will affect the failure pattern. Table 5.1 lists the apparent dominant failure mode ("tension" or "shear") for each combination of the shear strain rate and the ratio of tensile-to-shear strain rates.

Table 5.1 Dominant failure mode ("tension" or "shear") observed from the finite element simulation. For each shear strain rate, four different ratios of tensile strain rate/shear strain rate are considered.

Shear strain rate (s^{-1})	Tension/Shear (1/1)	Tension/Shear (1/5)	Tension/Shear (1/10)	Tension/Shear (1/20)
1	Tension	Shear	Shear	Shear
10	Tension	Tension	Tension	Shear
100	Tension	Tension	Tension	Tension

The table shows that the superimposed tension can influence the failure mode to a great extent. The influence becomes larger as the shear strain rate increases. As an example, even the smallest ratio of tensile and shear strain rates considered (1/20) can force the cracking to follow the tensile mode. For smaller shear strain rates, a greater ratio is

needed to achieve the same. In Fig. 5.13, contour plots showing the failure morphology of the following five cases are presented:

(a) shear strain rate 1 s^{-1}, tension/shear ratio 1/1

(b) shear strain rate 1 s^{-1}, tension/shear ratio 1/5

(c) shear strain rate 10 s^{-1}, tension/shear ratio 1/10

(d) shear strain rate 10 s^{-1}, tension/shear ratio 1/20, and

(e) shear strain rate 100 s^{-1}, tension/shear ratio 1/20

Note that the first four cases correspond to the strain rate conditions across the "boundary" between the tension mode (red) and shear mode (blue) in Table 5.1. It can be seen that, for the most part, failure appears in a distinct manner (either the tension mode or the shear mode). It is interesting to note, however, that in Fig. 5.13(d) the shear mode in fact still contains certain tension failure characteristics (i.e., cracking along the near 45° direction).

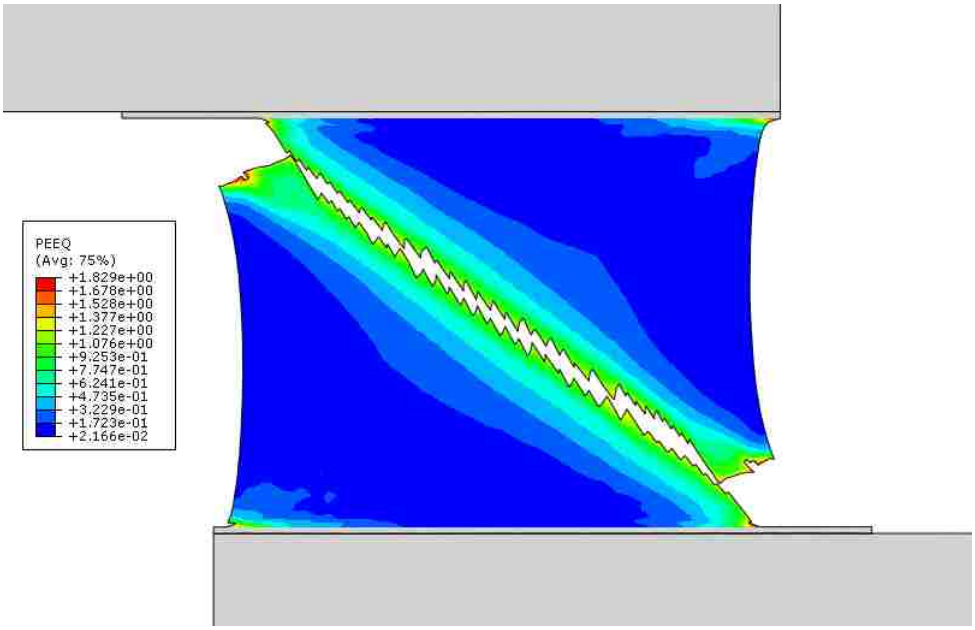
PEEQ
(Avg: 75%)
+1.829e+00
+1.678e+00
+1.528e+00
+1.377e+00
+1.227e+00
+1.076e+00
+9.253e-01
+7.747e-01
+6.241e-01
+4.735e-01
+3.229e-01
+1.723e-01
+2.166e-02

5.13 (a)

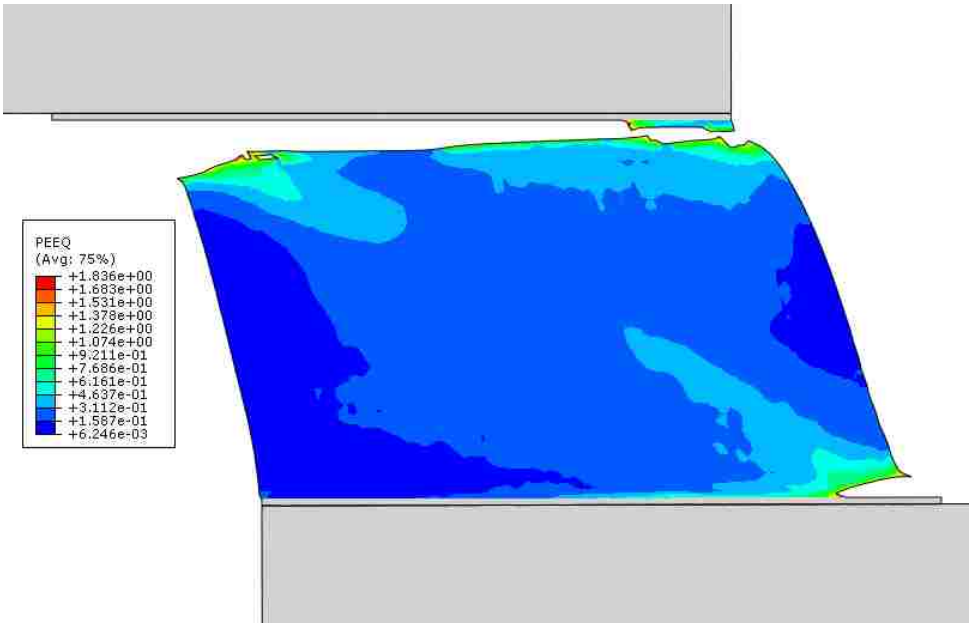
PEEQ
(Avg: 75%)
+1.836e+00
+1.683e+00
+1.531e+00
+1.378e+00
+1.226e+00
+1.074e+00
+9.211e-01
+7.686e-01
+6.161e-01
+4.637e-01
+3.112e-01
+1.587e-01
+6.246e-03

5.13 (b)

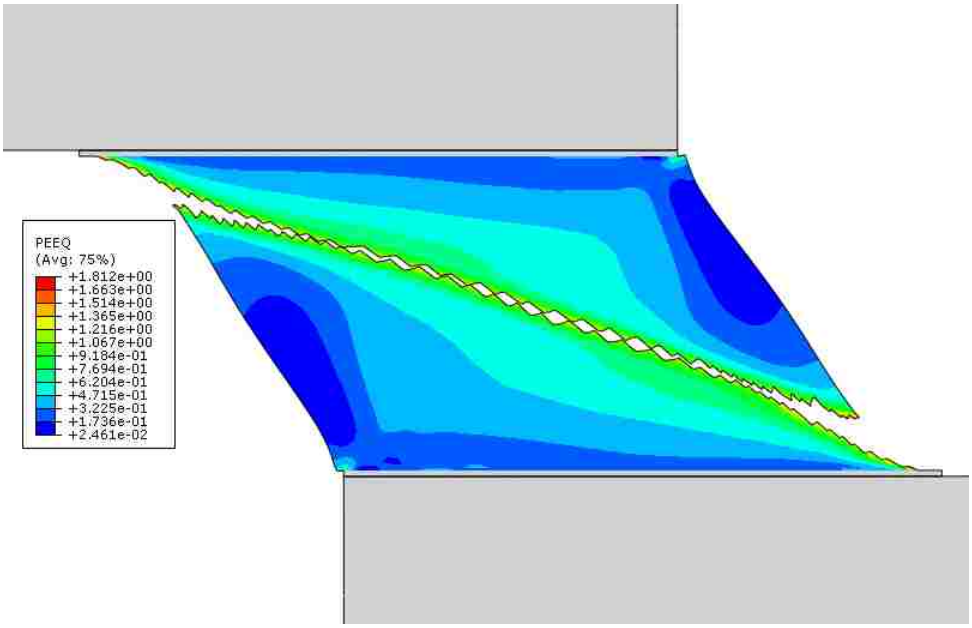
PEEQ
(Avg: 75%)
+1.812e+00
+1.663e+00
+1.514e+00
+1.365e+00
+1.216e+00
+1.067e+00
+9.184e-01
+7.694e-01
+6.204e-01
+4.715e-01
+3.225e-01
+1.736e-01
+2.461e-02

5.13(c)

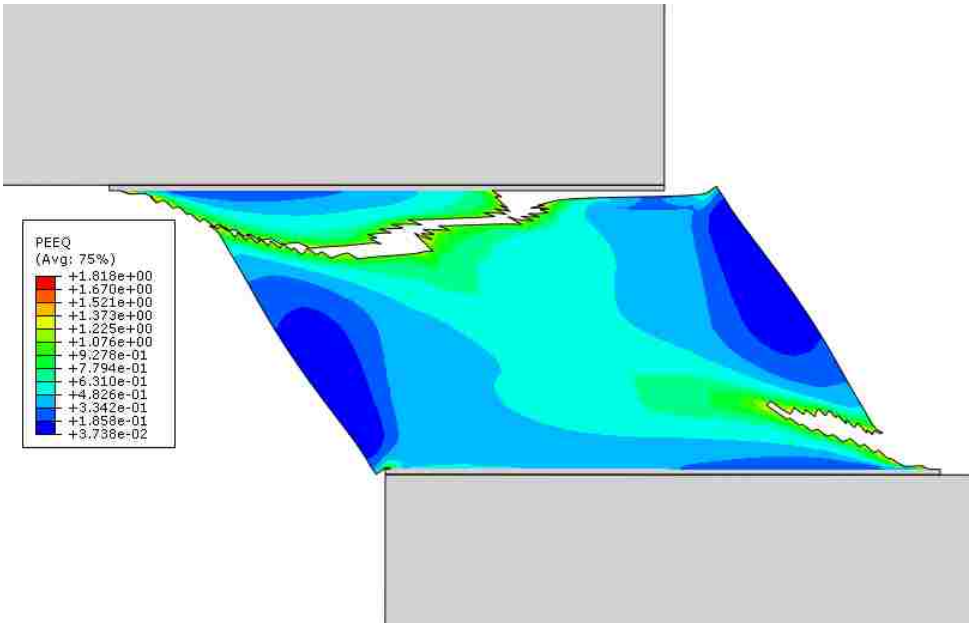
PEEQ
(Avg: 75%)
+1.818e+00
+1.670e+00
+1.521e+00
+1.373e+00
+1.225e+00
+1.076e+00
+9.278e-01
+7.794e-01
+6.310e-01
+4.826e-01
+3.342e-01
+1.858e-01
+3.738e-02

5.13(d)

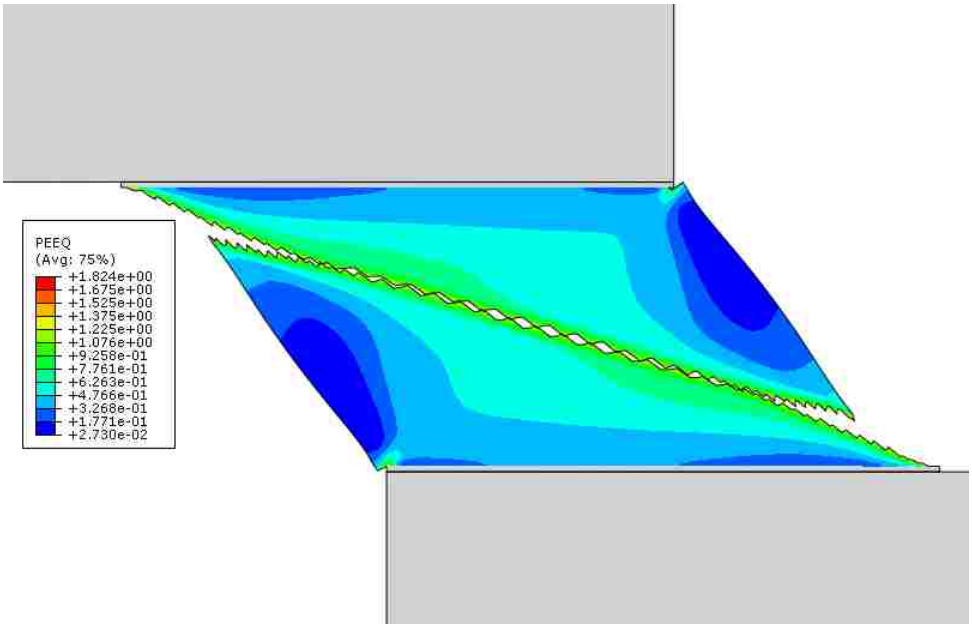

5.13(e)

Fig. 5.13 Failure modes for various superimposed tensile/shear deformation ratios.

5.4 Shear Loading with Superimposed Compression

The case of superimposed compression is now discussed. The dominant failure modes for the various combinations of shear strain rate and compressive strain rate are summarized in Table 5.2. Compared to the cases of superimposed tension, the influence of compression is less prominent. Only when the compression/shear ratio is high (1/1) does the compression mode become dominant.

Table 5.2 Dominant failure mode ("compression" or "shear") observed from the finite element simulation. For each shear strain rate, four different ratios of compressive strain rate/shear strain rate are considered.

Shear strain rate (s^{-1})	Compression/Shear (1/1)	Compression/Shear (1/5)	Compression/Shear (1/10)	Compression/Shear (1/20)
1	Compression	Shear	Shear	Shear
10	Compression	Shear	Shear	Shear
100	Compression	Shear	Shear	Shear

Figures 5.14(a)-(f) show the contour plots of equivalent plastic strain after complete failure of the joint, for the following cases:

(a) Shear strain rate 1 s^{-1}, compression/shear ratio 1/1,

(b) Shear strain rate 1 s^{-1}, compression/shear ratio 1/5,

(c) Shear strain rate 10 s^{-1}, compression/shear ratio 1/1,

(d) Shear strain rate 10 s^{-1}, compression/shear ratio 1/5,

(e) Shear strain rate 100 s^{-1}, compression/shear ratio 1/1, and

(f) Shear strain rate 100 s^{-1}, compression/shear ratio 1/5.

These six cases correspond to the strain rate conditions across the "boundary" between the compression mode (red) and shear mode (blue) in Table 5.2. It can be seen from Fig. 5.14 that the failure mode, either compression or shear, appears in a distinct manner without ambiguity.

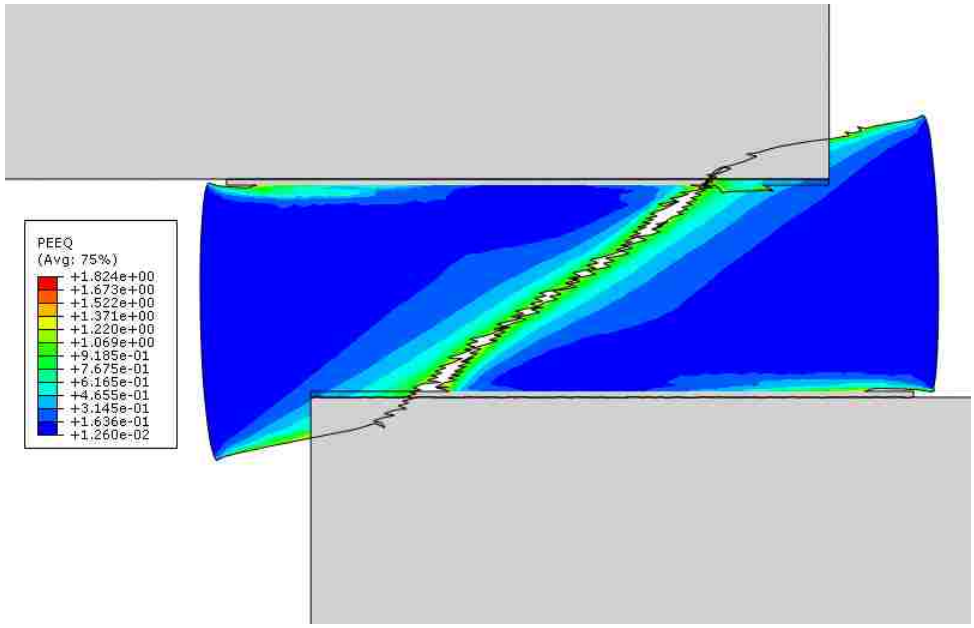
PEEQ
(Avg: 75%)
+1.824e+00
+1.673e+00
+1.522e+00
+1.371e+00
+1.220e+00
+1.069e+00
+9.185e-01
+7.675e-01
+6.165e-01
+4.655e-01
+3.145e-01
+1.636e-01
+1.260e-02

5.14(a)

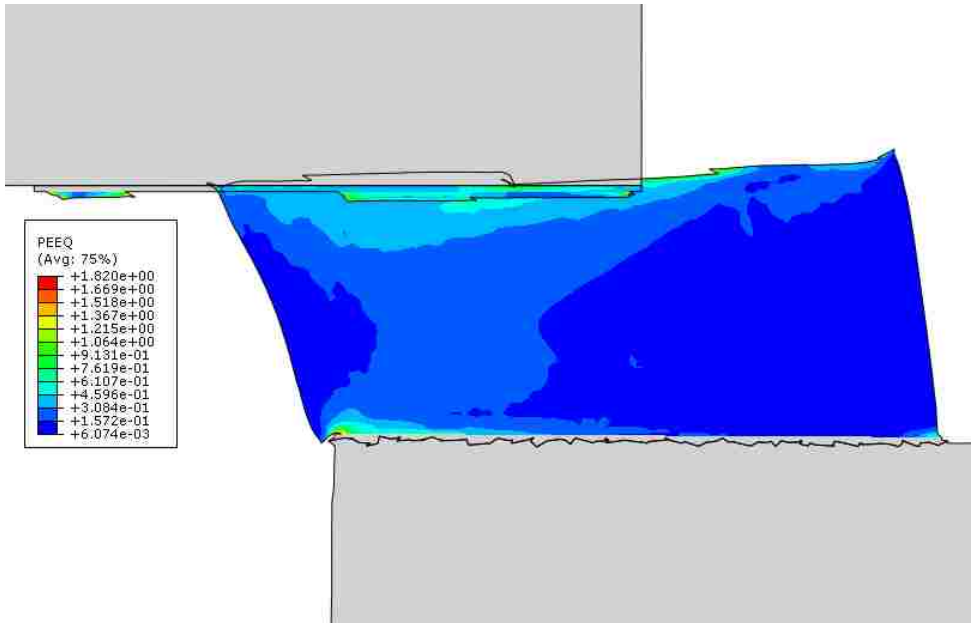
PEEQ
(Avg: 75%)
+1.820e+00
+1.669e+00
+1.518e+00
+1.367e+00
+1.215e+00
+1.064e+00
+9.131e-01
+7.619e-01
+6.107e-01
+4.596e-01
+3.084e-01
+1.572e-01
+6.074e-03

5.14(b)

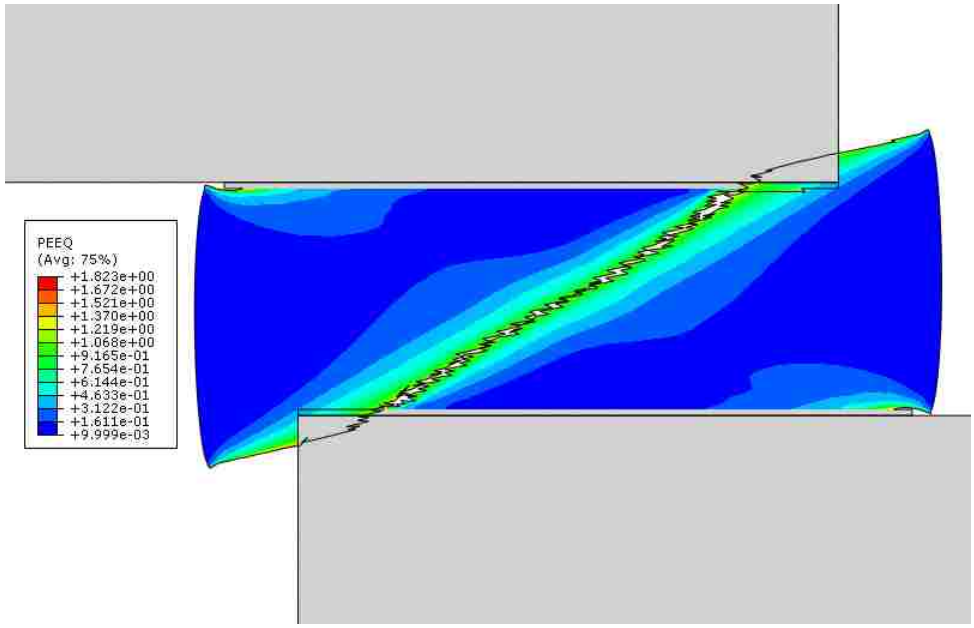
PEEQ
(Avg: 75%)
+1.823e+00
+1.672e+00
+1.521e+00
+1.370e+00
+1.219e+00
+1.068e+00
+9.165e-01
+7.654e-01
+6.144e-01
+4.633e-01
+3.122e-01
+1.611e-01
+9.999e-03

5.14(c)

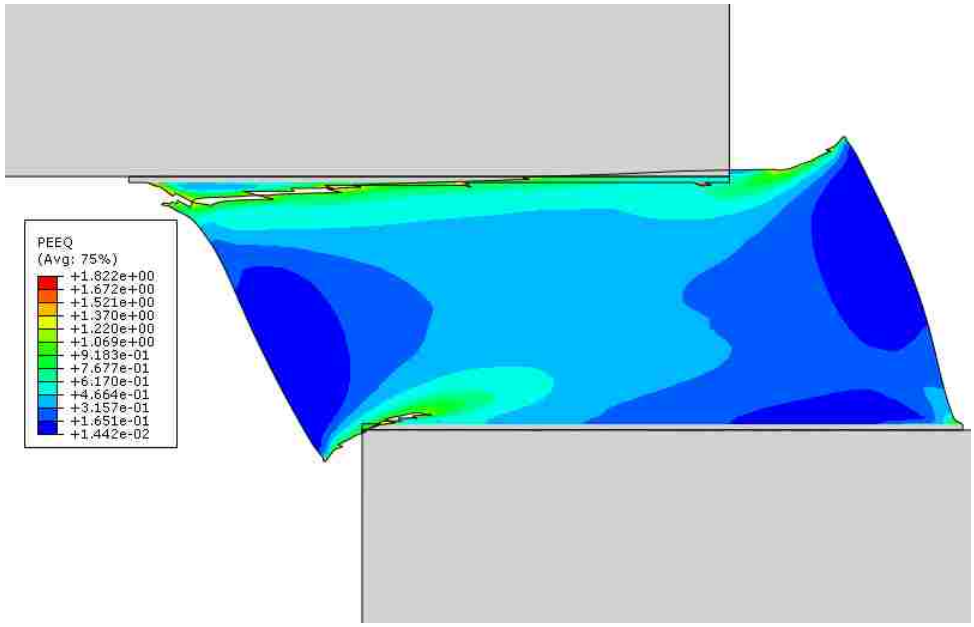
PEEQ
(Avg: 75%)
+1.822e+00
+1.672e+00
+1.521e+00
+1.370e+00
+1.220e+00
+1.069e+00
+9.183e-01
+7.677e-01
+6.170e-01
+4.664e-01
+3.157e-01
+1.651e-01
+1.442e-02

5.14(d)

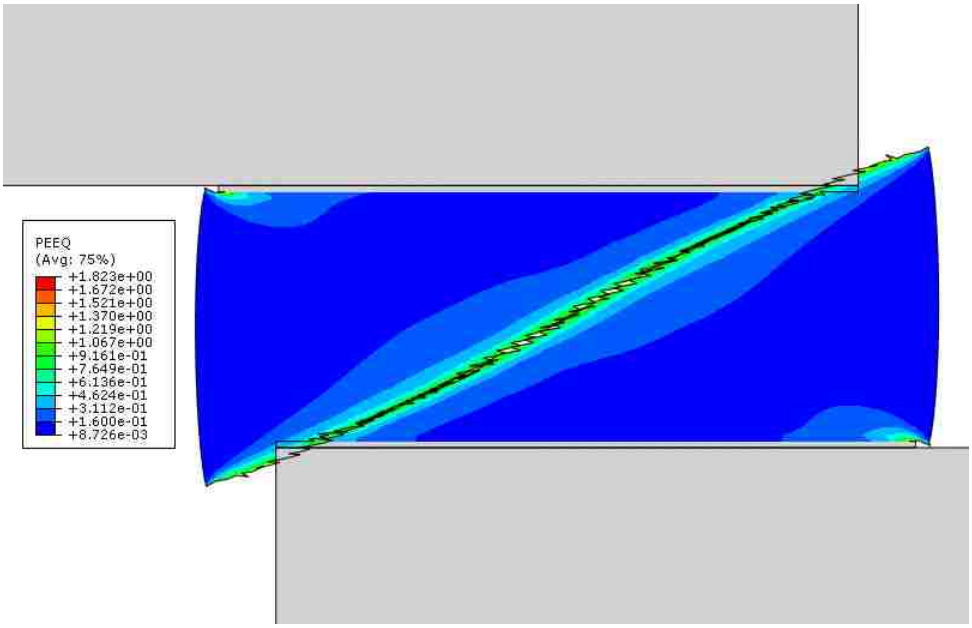

5.14(e)

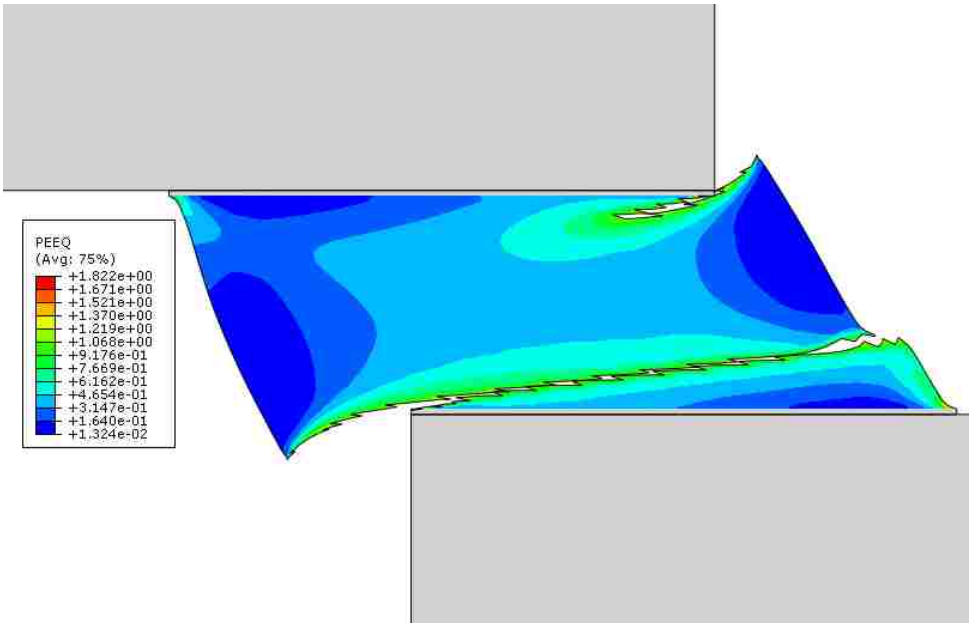

5.14(f)

Fig. 5.14 Failure modes for various superimposed compressive/shear deformation ratios.

5.5 Conclusions

The second set of damage parameters (allowing delayed damage and thus higher ductility) was seen to generate a similar kind of failure features with some exceptions, compared to the modeling results presented in Chapters 3 and 4 using the first set of damage parameters. The pure shear loading at the 1 s^{-1} strain rate leads to failure largely along the interface between the solder and the intermetallic, while the 10 s^{-1} and 100 s^{-1} strain rates show failure paths away from the interface. Final fracture is a result of a single crack initiating from one corner and propagating to the other side of the joint, as opposed to the linking of two cracks initiating from different corners. When tension or compression is superimposed on the shear loading, the dominant failure mode can be affected. Only a small fraction of superimposed tension is needed to trigger a tension failure mode if the applied strain rate is high. In general a higher compression/shear ratio is needed for the solder to display a compression failure mode. Despite the quantitative differences of the failure behavior resulting from the two sets of damage parameters, it is fair to conclude that the fundamental features stay unchanged.

Chapter-6 Cyclic Deformation

In most of the actual devices and test structures, deformation of the solder joints is cyclic in nature. The amplitude of strain or stress may not be large, but after repeated loading a fatigue crack eventually develops and severs the joint. This can be a consequence of "slow" cyclic loading such as that due to thermal expansion mismatch between the two components (e.g., chip carrier and printed circuit board) the solder connects, or a consequence of "fast" cyclic loading resulting from mechanical vibration. In this chapter we present simulation results based on the three shear strain rates considered in the previous chapters. Only the shear loading is investigated, with the nominal shear strain range between 0 and 0.01. The "standard" set of damage parameters is used, and we seek to examine the effects of loading rate on the failure pattern and the number of cycles to failure.

6.1 Evolution of Cyclic Stress and Deformation Fields

First we compare the representative stress and strain fields developed in the solder joint before any crack initiation. Figures 6.1(a)-(c) show the contour plots of von Mises effective stress, shear stress σ_{xy}, and equivalent plastic strain, respectively, after 4 full cycles of shear strain between 0 and 0.01 under the constant shear strain rate of 1 s^{-1}. It is evident that, although the current nominal shear strain of the entire joint is zero (after 4 full cycles), Figs. 6-1(a) and (b) still show significant values of stresses, which is due to the non-uniform stress field and strong plastic deformation during the cyclic process. In

Fig. 6.1(c), a band of localized strain can be seen near each interface with the intermetallic. Figures 6.2 and 6.3 show the same sets of contour plots, after 4 full cycles of shear strain between 0 and 0.01 under the constant shear strain rate of 10 s^{-1} and 100 s^{-1}, respectively. It is also noted that some regions in the copper substrates are also under relatively high stresses. So in reality, plastic deformation may occur in copper as well, although in the current analysis the substrate material is assumed to be elastic only.

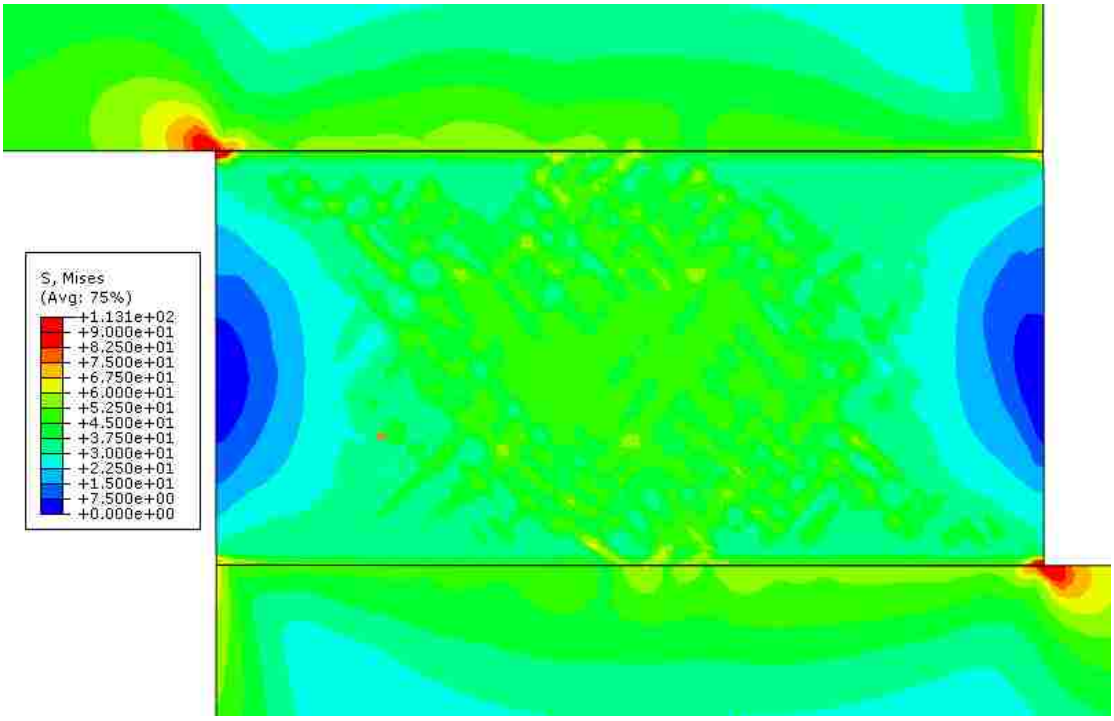
S, Mises
(Avg: 75%)
+1.131e+02
+9.000e+01
+8.250e+01
+7.500e+01
+6.750e+01
+6.000e+01
+5.250e+01
+4.500e+01
+3.750e+01
+3.000e+01
+2.250e+01
+1.500e+01
+7.500e+00
+0.000e+00

(a)

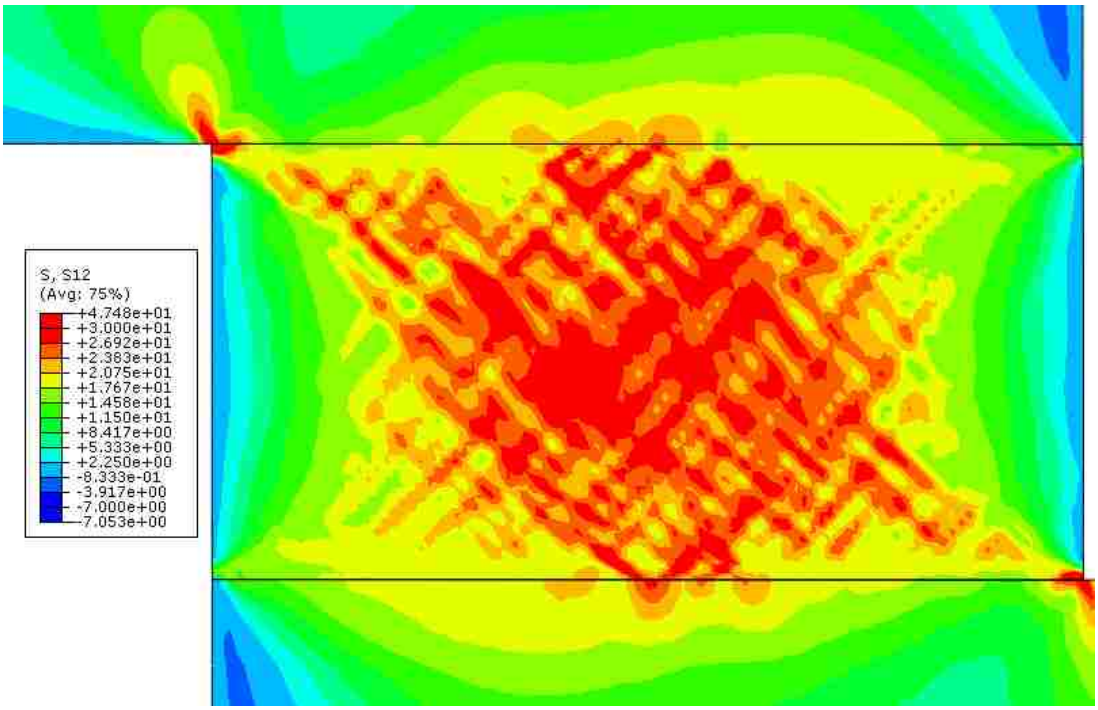
S, S12
(Avg: 75%)
+4.748e+01
+3.000e+01
+2.692e+01
+2.383e+01
+2.075e+01
+1.767e+01
+1.458e+01
+1.150e+01
+8.417e+00
+5.333e+00
+2.250e+00
-8.333e-01
-3.917e+00
-7.000e+00
-7.053e+00

(b)

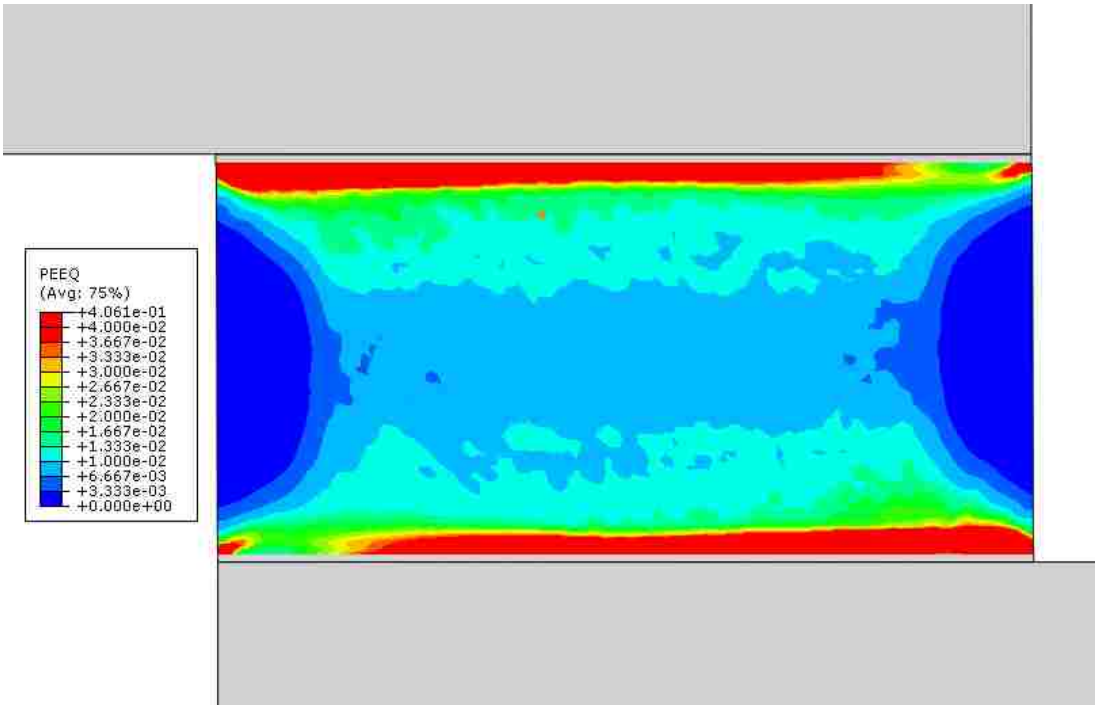

(c)

Fig. 6.1 Contour plots showing (a) von Mises effective stress, (b) Shear stress σ_{xy}, and (c) equivalent plastic strain, after 4 full cycles under the $1s^{-1}$ shear strain rate between the nominal shear strains 0 and 0.01.

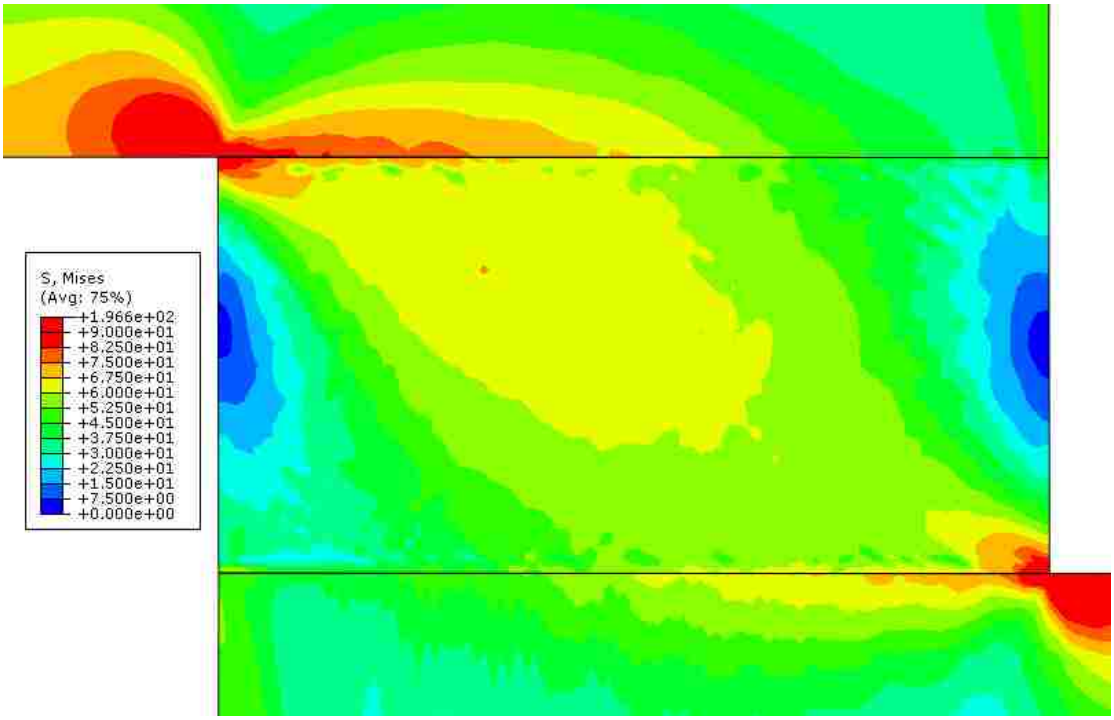
S, Mises
(Avg: 75%)
+1.966e+02
+9.000e+01
+8.250e+01
+7.500e+01
+6.750e+01
+6.000e+01
+5.250e+01
+4.500e+01
+3.750e+01
+3.000e+01
+2.250e+01
+1.500e+01
+7.500e+00
+0.000e+00

(a)

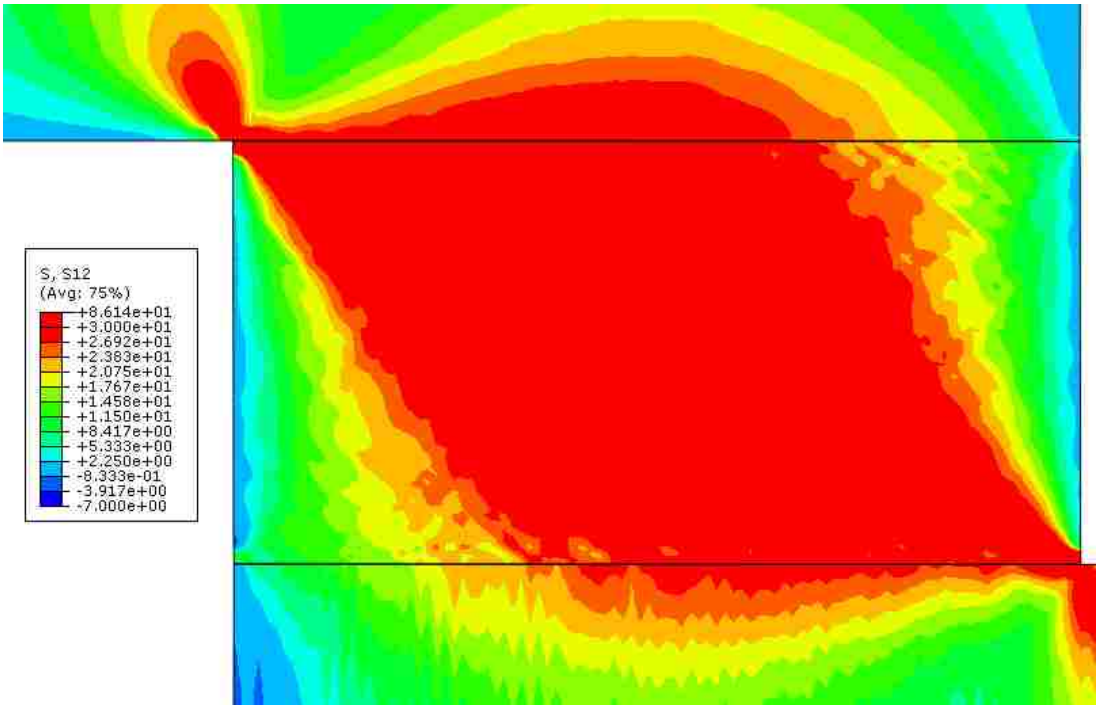
S, S12
(Avg: 75%)
+8.614e+01
+3.000e+01
+2.692e+01
+2.383e+01
+2.075e+01
+1.767e+01
+1.458e+01
+1.150e+01
+8.417e+00
+5.333e+00
+2.250e+00
-8.333e-01
-3.917e+00
-7.000e+00

(b)

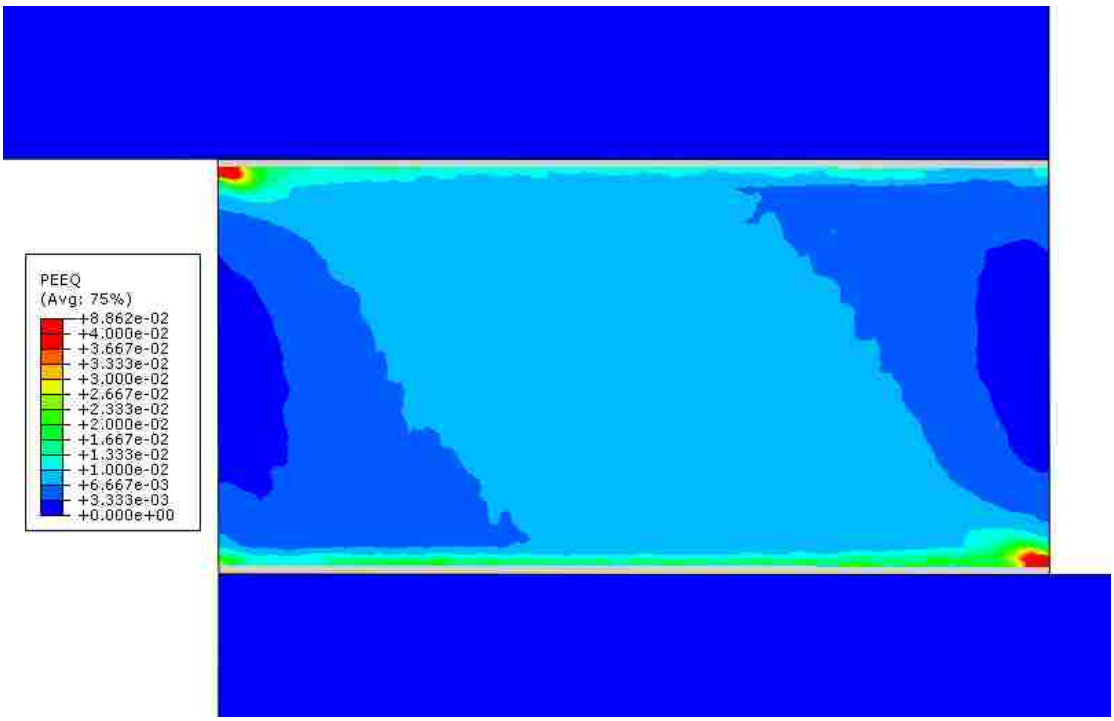

(c)

Fig. 6-2 Contour plots showing (a) von Mises effective stress, (b) Shear stress σ_{xy}, and (c) equivalent plastic strain, after 4 full cycles under the 10 s^{-1} shear strain rate between the nominal shear strains 0 and 0.01.

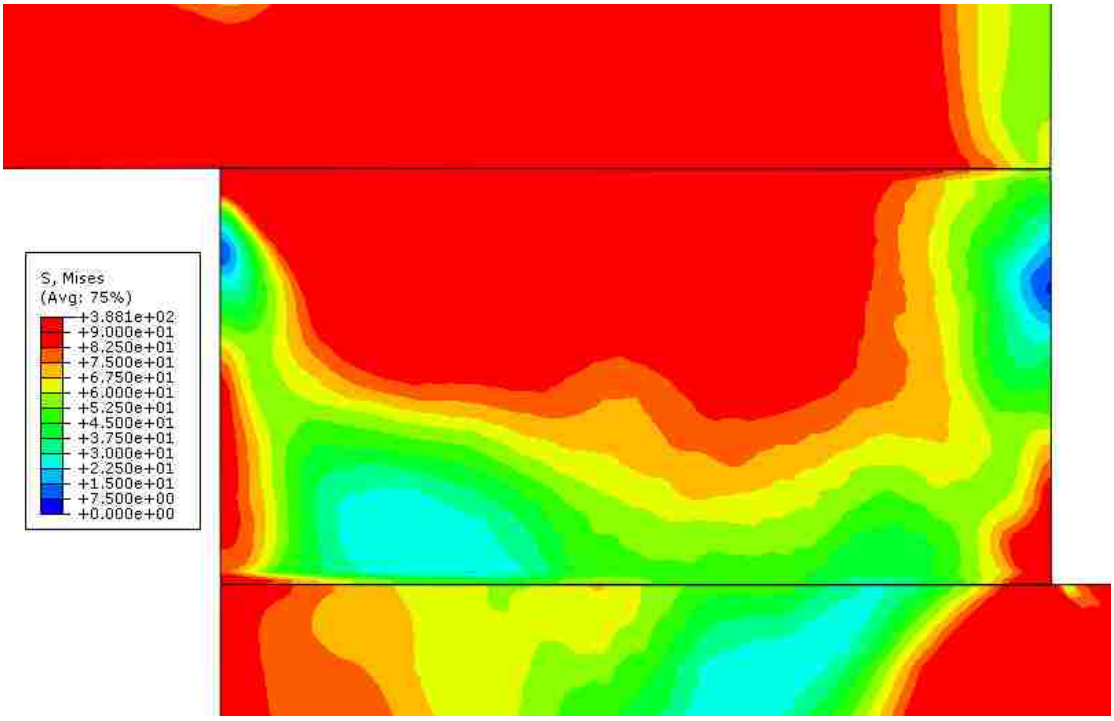
S, Mises
(Avg: 75%)
+3.881e+02
+9.000e+01
+8.250e+01
+7.500e+01
+6.750e+01
+6.000e+01
+5.250e+01
+4.500e+01
+3.750e+01
+3.000e+01
+2.250e+01
+1.500e+01
+7.500e+00
+0.000e+00

(a)

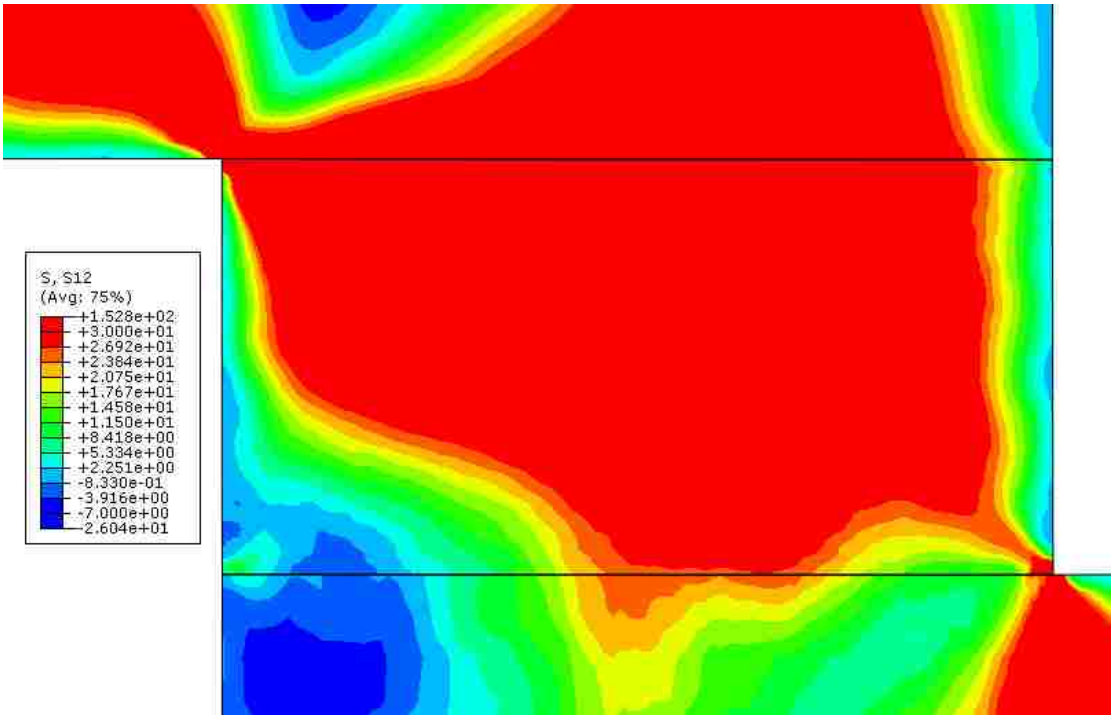
S, S12
(Avg: 75%)
+1.528e+02
+3.000e+01
+2.692e+01
+2.384e+01
+2.075e+01
+1.767e+01
+1.458e+01
+1.150e+01
+8.418e+00
+5.334e+00
+2.251e+00
-8.330e-01
-3.916e+00
-7.000e+00
-2.604e+01

(b)

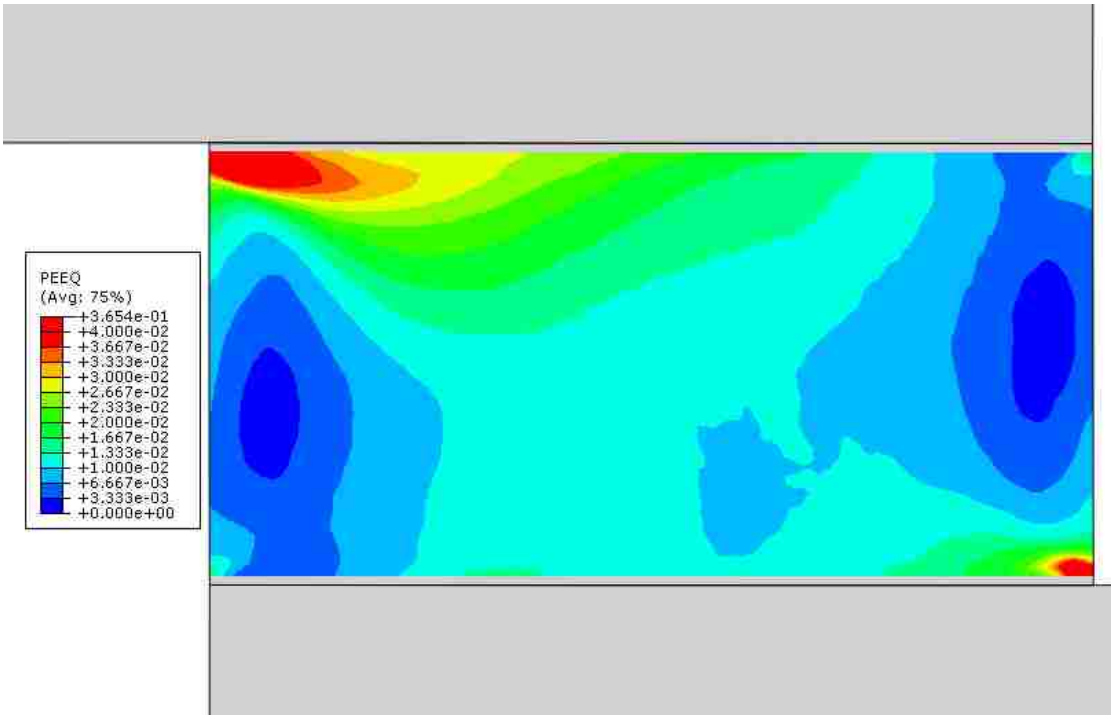

(c)

Fig. 6-3 Contour plots showing (a) von Mises effective stress, (b) Shear stress σ_{xy}, and (c) equivalent plastic strain, after 4 full cycles under the 100 s^{-1} shear strain rate between the nominal shear strains 0 and 0.01.

Comparing the Mises stress and shear stress contour plots in Figs. 6.1-6.3, it is evident that the stress values increase with an increasing strain rate. Therefore this strain-rate hardening phenomenon is also significant in the case of cyclic loading. In Fig. 6.2(c), the concentration of equivalent plastic strain near the interface is much weaker compared to Fig. 6.1(c). However, in Fig. 6.3(c) the localized deformation band has not been developed after 4 cycles. High plastic strains are still largely in the corner regions.

6.2 Failure Pattern

Attention is now turned to the cracking behavior of the solder joint under cyclic shearing. Figures 6.4(a), (b) and (c) show the contour plots of equivalent plastic strain and the cracking configuration shortly after crack initiation, halfway (in terms of the number of cycles) between crack initiation and complete failure, and shortly after complete failure, respectively, for the case of the 1 s^{-1} shear strain rate. The numbers of cycles for parts (a), (b) and (c) are indicated in the figure caption. The corresponding plots for the strain rates of 10 s^{-1} and 100 s^{-1} are shown in Figures 6.5 and 6.6, respectively. In all the cases, the fatigue crack initiated from one of the corners of the joint and propagated inward along or near the interface. At final fracture, two major cracks are seen in all cases: one has traversed the entire joint and the other also has propagated over a significant distance. Therefore, although only one crack is responsible for the final failure, the damage process itself is not associated with only one dominant crack. We attribute this to the slow and steadily progressive accumulation of plastic strain during the cyclic deformation, which leads to significant strain-rate hardening so the two main cracks had to “take turns” to continue with the propagation process.

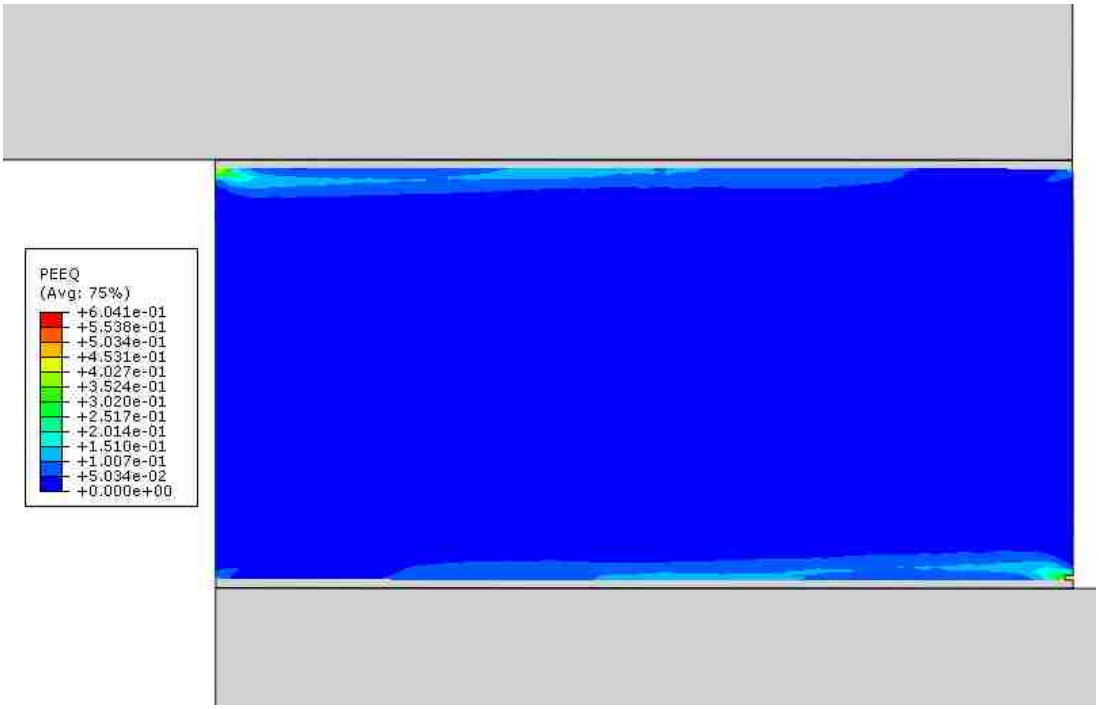
PEEQ
(Avg: 75%)
+6.041e-01
+5.538e-01
+5.034e-01
+4.531e-01
+4.027e-01
+3.524e-01
+3.020e-01
+2.517e-01
+2.014e-01
+1.510e-01
+1.007e-01
+5.034e-02
+0.000e+00

(a)

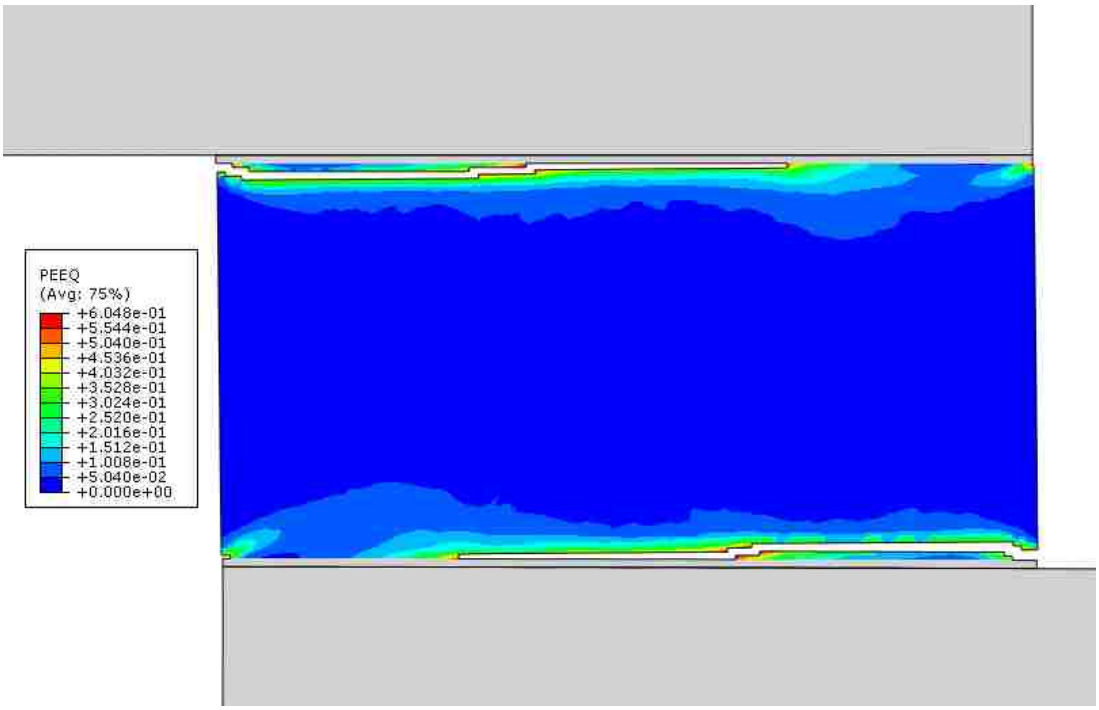
PEEQ
(Avg: 75%)
+6.048e-01
+5.544e-01
+5.040e-01
+4.536e-01
+4.032e-01
+3.528e-01
+3.024e-01
+2.520e-01
+2.016e-01
+1.512e-01
+1.008e-01
+5.040e-02
+0.000e+00

(b)

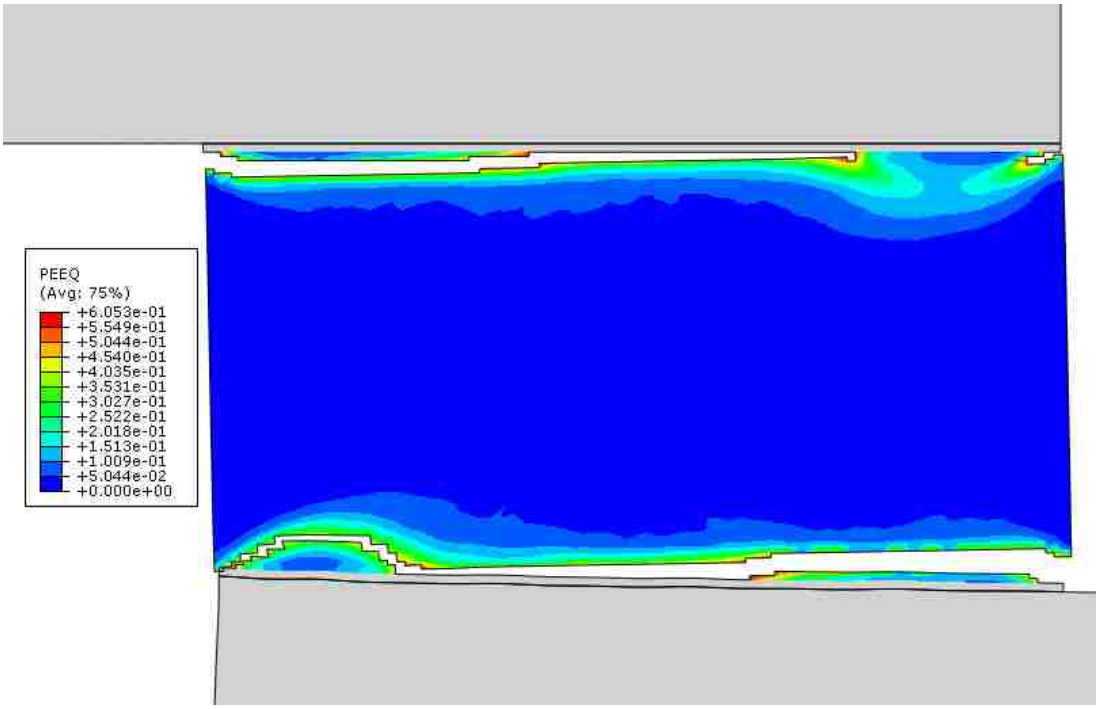

(c)

Fig. 6.4 Contour plots showing the equivalent plastic strain and crack profile for the case of $1s^{-1}$ strain rate at (a) 5 cycles, (b) 20.5 cycles, and (c) 36 cycles

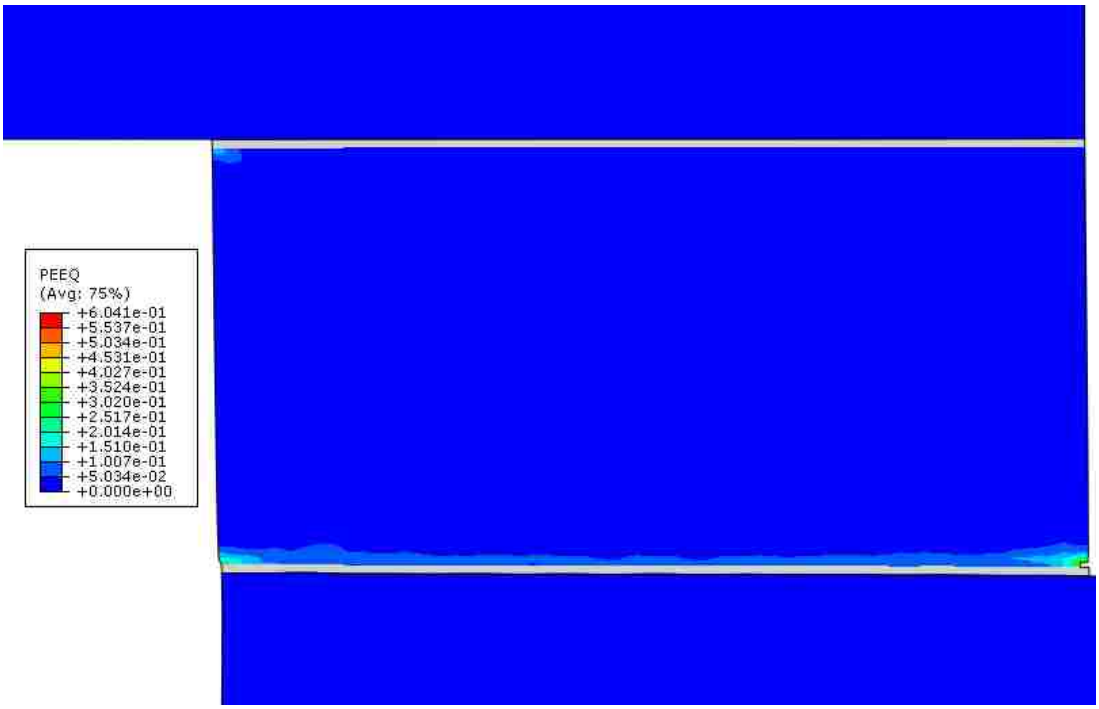
PEEQ
(Avg: 75%)
+6.041e-01
+5.537e-01
+5.034e-01
+4.531e-01
+4.027e-01
+3.524e-01
+3.020e-01
+2.517e-01
+2.014e-01
+1.510e-01
+1.007e-01
+5.034e-02
+0.000e+00

(a)

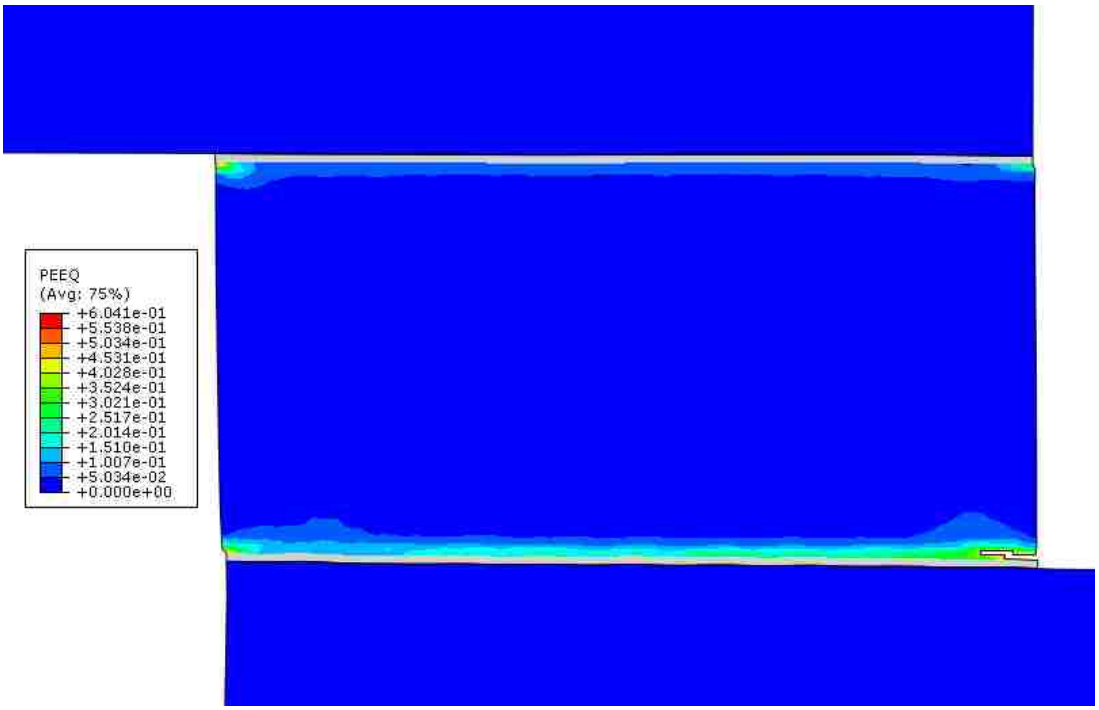
PEEQ
(Avg: 75%)
+6.041e-01
+5.538e-01
+5.034e-01
+4.531e-01
+4.028e-01
+3.524e-01
+3.021e-01
+2.517e-01
+2.014e-01
+1.510e-01
+1.007e-01
+5.034e-02
+0.000e+00

(b)

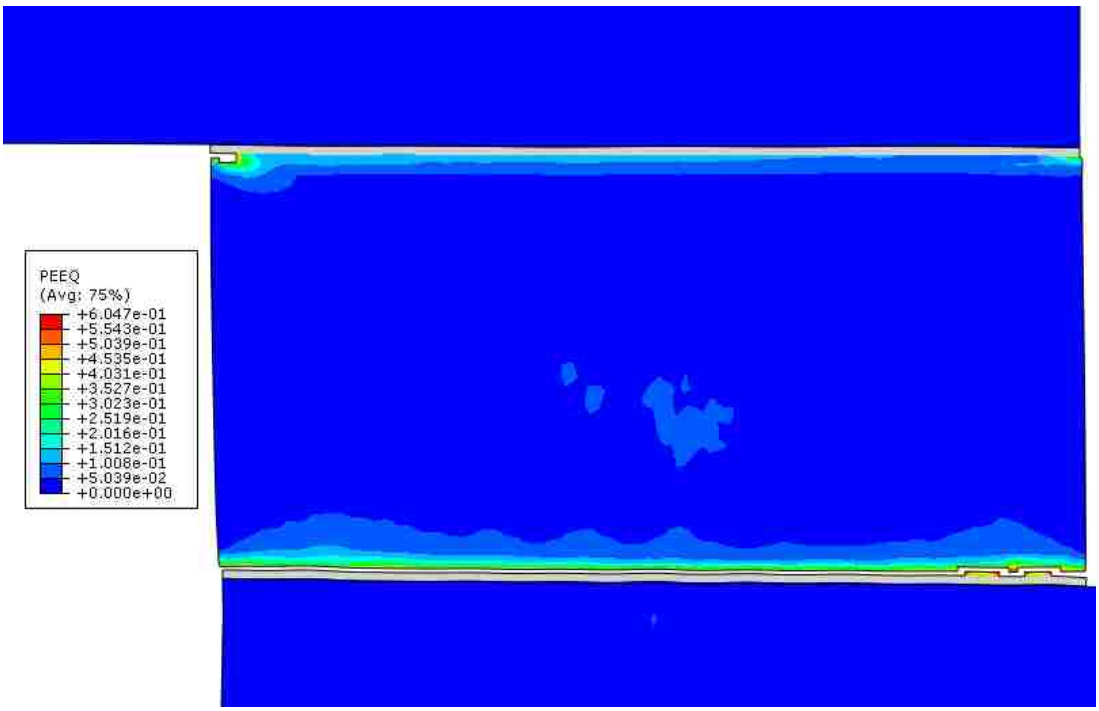

(c)

Fig. 6.5 Contour plots showing the equivalent plastic strain and crack profile for the case of $10s^{-1}$ strain rate at (a) 8.5 cycles, (b) 23 cycles, and (c) 37 cycles

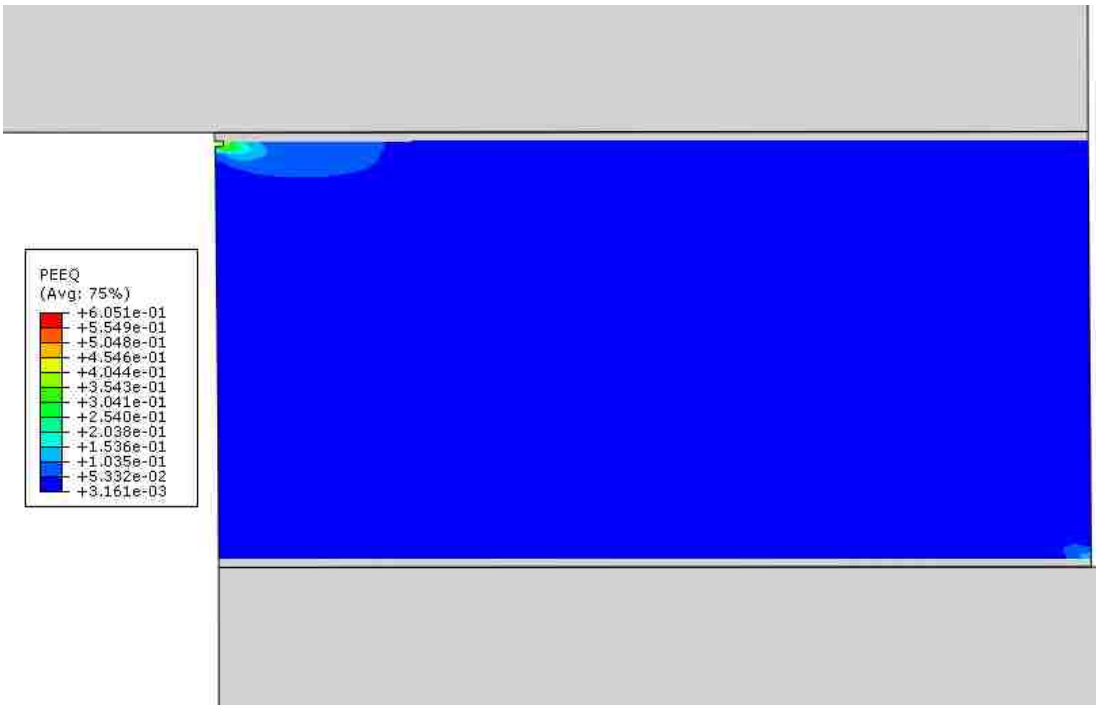
PEEQ
(Avg: 75%)
+6.051e-01
+5.549e-01
+5.048e-01
+4.546e-01
+4.044e-01
+3.543e-01
+3.041e-01
+2.540e-01
+2.038e-01
+1.536e-01
+1.035e-01
+5.332e-02
+3.161e-03

(a)

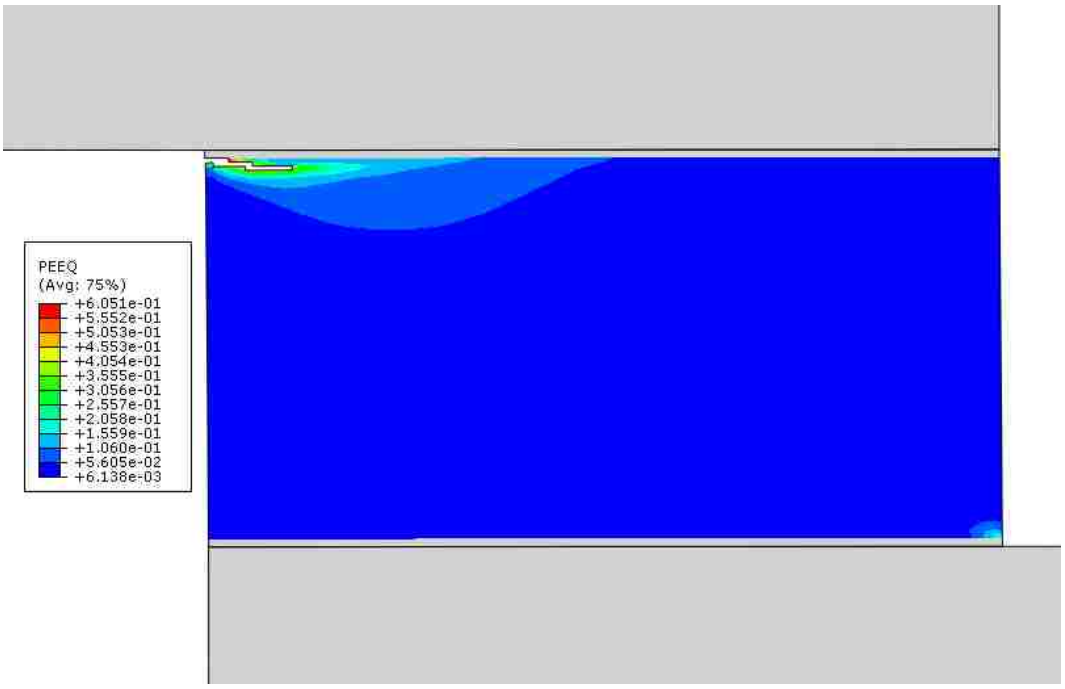
PEEQ
(Avg: 75%)
+6.051e-01
+5.552e-01
+5.053e-01
+4.553e-01
+4.054e-01
+3.555e-01
+3.056e-01
+2.557e-01
+2.058e-01
+1.559e-01
+1.060e-01
+5.605e-02
+6.138e-03

(b)

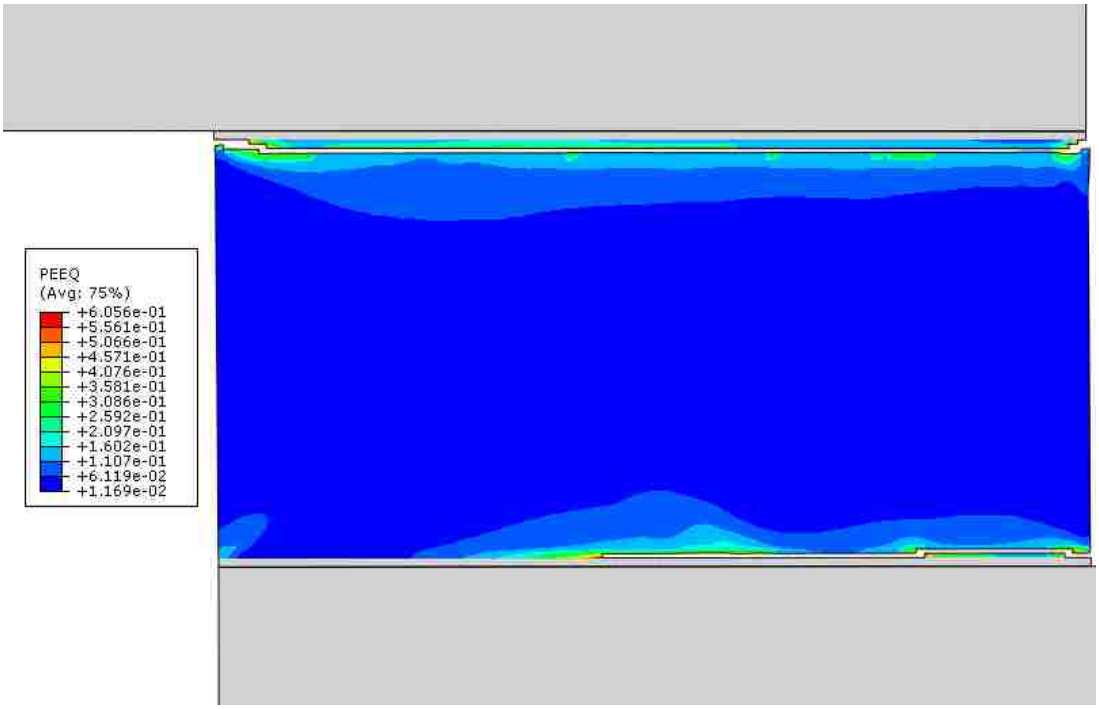

(c)

Fig. 6.6 Contour plots showing the equivalent plastic strain and crack profile for the case of 100s^{-1} strain rate at (a) 5.5 cycles, (b) 11.5 cycles, and (c) 16.5 cycles

It is also worth pointing out, from Figs. 6.4(b), 6.5(b) and 6.6(b), that at a stage halfway between the crack initiation and final failure, only the case of the slowest strain rate (Fig. 6.4(b)) showed long cracks near the two interfaces. This means that crack propagation is steadier in this case. For higher strain rates, crack propagation is initially relatively slow but becomes faster toward the late stages of the cycling history.

The final failure patterns observed in Figs. 6.4-6.6 are different from those observed in the monotonic loading in Chapter 3. In the case of 1 s^{-1} strain rate, the crack morphology in Fig. 6.4(c) is more complicated than in Fig. 3.5(b). In Figs. 6.5(c) (10 s^{-1} strain rate) and 6.6(c) (100 s^{-1} strain rate), the final cracks are much closer to the interface than what was observed in Figs. 3.6(b) (10 s^{-1} strain rate) and 3.7(b) (100 s^{-1} strain rate). In general, under fast cyclic shearing, ductile failure of the solder joint appears to be more localized in the near-interface region.

Figure 6.7 shows the number of cycles required for the initiation of fatigue cracks and final failure, as a function of the applied nominal shear strain rate. There is no simple trend found, except that crack propagation generally takes a longer time than that needed to initiate the first crack. In the case of 100 s^{-1}, the crack spends a much shorter time (in terms of cycles) in traversing the entire solder joint than the cases of slower rates.

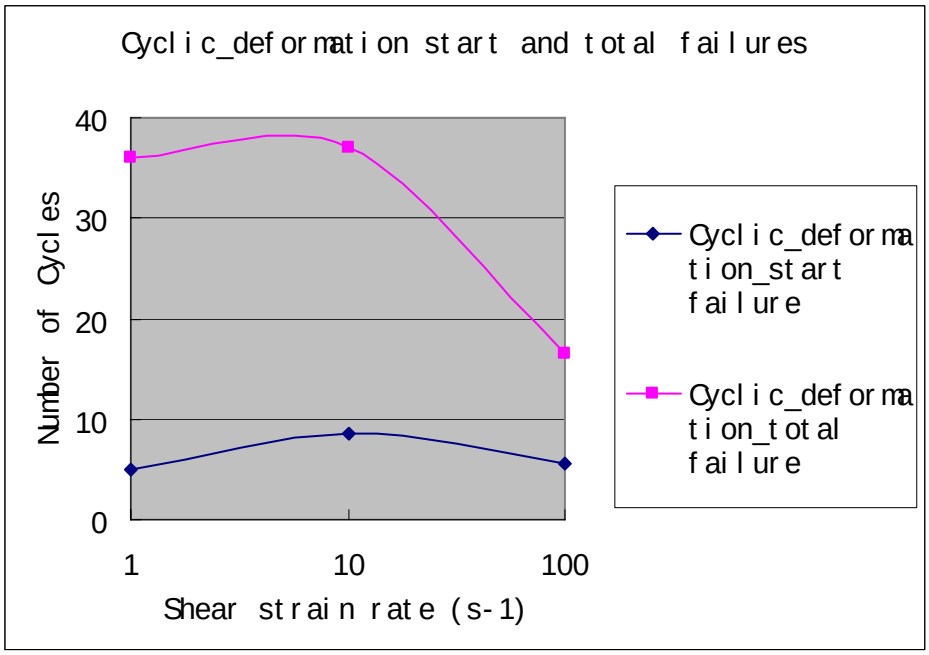

Fig. 6.7 Chart of Number of cycles for the initiation of fatigue cracks and final failure vs. applied nominal shear strain rate (s^{-1}).

6.3 Experimental Observations

Although there have been a large quantity of studies on shock and impact response of lead-free solder in recent years, we have not found clear cross-section micrographs in the literature showing the crack profile under controlled fast cyclic loading conditions. Again, the real failure pattern will depend on the alloy system, microstructure, detailed joint geometry, intermetallic morphology, peripheral structures, and the exact loading history etc. A direct comparison with the present modeling is therefore impossible. In Figure 6.8 representative experimental pictures, showing solder failure due to the "slow"

thermo-mechanical fatigue, are presented. We note that these solder joints all display the near-interface failure pattern.

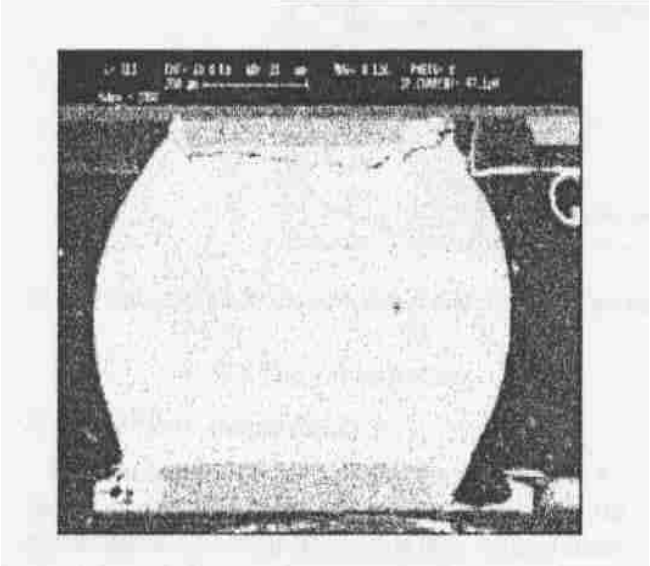

(a) SEM picture of solder joint fatigue failure by Mechanical Deflection System (MDS) test.

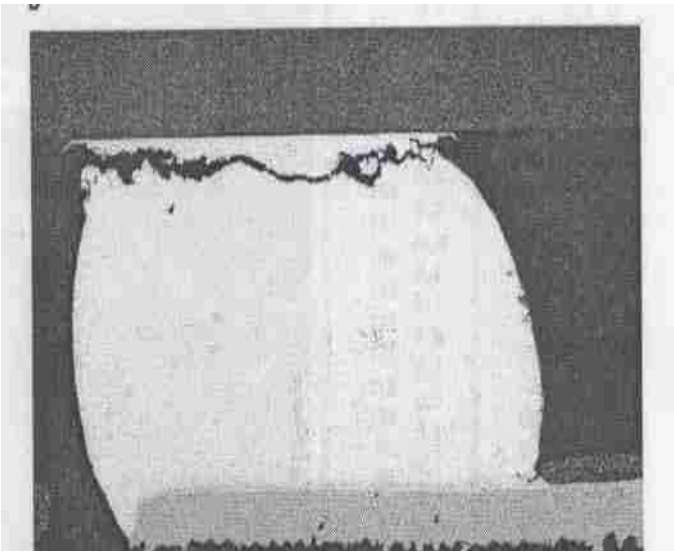

(b) SEM Micrographs of lead-free vehicles (Sn-3Ag-0.5Cu paste) for 500 cycles of Thermal Cycling Test (TCT).

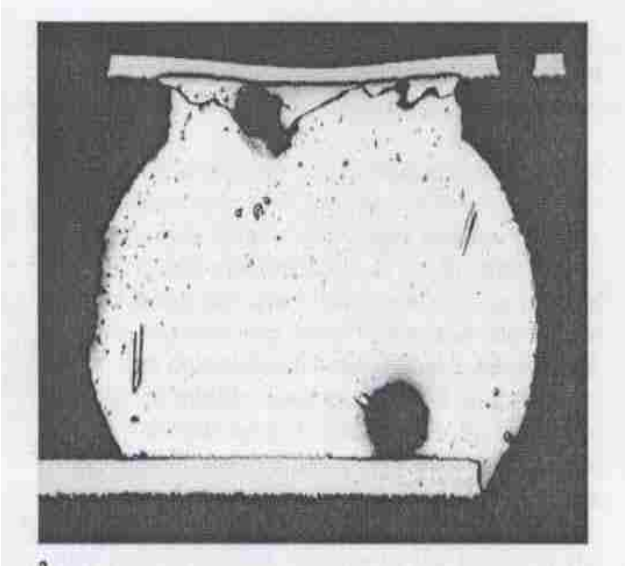

(c) Intergranular fracture through the bulk of the solder in thermally cycled interconnection

Fig. 6.8 Experimental photographs showing solder failure due to slow cyclic loading conditions. Parts (a), (b) and (c) are taken from References [13], [42] and [43], respectively.

6.4 Conclusions

Cyclic shearing results in different failure patterns from those of monotonic loading. The three different strain rates do not lead to fundamentally different fracture appearance, although the fatigue life (number of cycles to failure) for the case of fastest strain rate (100 s^{-1}) is significantly shorter than the other two due to the faster crack propagation. In all cases, the fatigue cracks are very close to the interface between the solder and the intermetallic. In addition to the main crack that is responsible for the final fracture, a second crack near the other interface of the joint has also grown to a significant length in all cases.

Chapter 7 Conclusions and Future Work

In this thesis research, numerical finite element analyses were carried out to study ductile damage in solder joints under fast loading conditions.The effects of applied strain rate (in the range of 1 to 100 s^{-1}) and loading mode (shear with possible superimposed tension/compression) on the failure pattern were investigated. Salient conclusions are summarized below.

1. Under the pure shear loading mode, the ductility of solder increases as the applied strain rate increases. Final cracking is predominantly along the interface when the strain rate is low (1 s^{-1}) but becomes away from the interface as the strain rate increases.
2. The shear-induced failure pattern can be strongly affected by the superimposed tension and compression on the solder joint. With the tension or compression strain rate being only a small fraction of the shear strain rate, the failure pattern can change from the "shear mode" (near-interface) to the "tension/compression mode" (near 45º direction). Both the superimposed tension and compression can lead to a decrease in overall ductility of the solder, thus showing a negative impact on the solder joint reliability.
3. If a different set of damage parameters, allowing higher ductility and delayed fracture initiation, is used, the fundamental failure features remain unchanged. The evolution of cracking, however, originates from one corner and propagates to the other side of the joint as opposed to the linking of two cracks initiating from different corners.

4. Cyclic shearing results in different fracture appearances from those of monotonic loading. In all strain rates the fatigue cracks are near the interface between the solder and intermetallic. The two cracks, one near each interface, have both grown to a significant distance after cycles, with one of them eventually severing the joint.

The present study has laid the groundwork for building up the predictive modeling capability which takes physical fracture into account in an explicit manner. The suggested future work is listed below.

1. The current model utilized only one joint geometry. It will be interesting to study the solder joint failure under fast loading conditions with different solder geometries (both 2D and 3D).The temperature effect may also be included.
2. For the same solder geometry, it is important to study the solder joint failure under slow loading conditions so a wider spectrum of applied strain rate can be covered. For facilitating a systematic comparison with experiments, actual physical tests correlating the shear strain rate and failure pattern in the solder need to be carried out.
3. Certain solder joint design features, such as the bond pad and more realistic joint-substrate geometries, may be incorporated into the numerical model, for a more comprehensive understanding of the effects of these material and geometric characteristics.
4. Material coefficients used in many life prediction models have not been fully developed for lead-free solder. Within the context of this study, the damage parameters and detailed functional form need to be further quantified through experimental studies.

5. The current numerical model does not include any true interface failure features. Adding the brittle failure model along the interface between solder and intermetallic, such as using the cohesive-element method, is expected to yield particularly interesting results. The “competition” between interface failure and ductile damage, under a variety of loading conditions, can then be explored.

References

[1] W.J.Plumbridge, "Review Solders in Electronics," *Journal of Materials Science*, Vol.31, pp.2501-2514, 1996.

[2] Milton Ohring, Reliability and Failure of Electronic Materials and Devices, United Kingdom Edition, *Academic Press Limited,* pp.435-447, 1998.

[3] Sung K.Kang, Amit K.Sarkhel, "Lead (Pb)-Free Solders for Electronic Packaging," *Journal of Electronic Materials*, Vol.23, No.8, pp.701-707, 1994.

[4] Sabine Nieland, Mario Baehr, Anja Boettger, Andreas Ostmann and Herbert Reichl, "Advantages of microelectronic packaging for low temperature lead free soldering of thin solar cells," *22nd European Photovoltaic Solar Energy Conference and Exhibition*, September 2007, *CiS Erfurt*, Germany.

[5] Hua Ye, Cemal Basaran, Douglas C.Hopkins, Darrel Frear, "Deformation of solder joints under current stressing and numerical simulation-I," *International Journal of Solids and Structures*, Vol.41, pp. 4939-4958, 2004.

[6] P.L. Tu, Y.C.Chan, Senior Member, IEEE, and Joseph K.L.Lai, "Effect of Intermetallic Compounds on vibration Fatigue of μBGA solder joint," *IEEE Transactions on Advanced Packaging*, Vol.24, No.2,pp.197-205,May 2001.

[7] Kiranmaye Aluru, Yu-Lin Shen, Department of Mechanical Engineering, UNM, "Ductility Enhancement of Rare-Earth Containing Pb-Free Solder," in *The 20th Annual Riogrande Symposium on Advanced Materials (RGSAM 20),* 2008.

[8] M.A.Dudek, R.S.Sidhu, N. Chawla, and M.Renavikar, "Microstructure and Mechanical Behavior of Novel Rare Earth-Containing Pb-Free Solders," *Journal of Electronic Materials*, Vol 35, No.12, pp. 2088-2097, 2006.

[9] Ning Bai, Xu Chen, and Zhou Fang, "Effect of strain rate and temperature on the tensile properties of tin-based lead-free solder alloys," *Journal of Electronic Materials*, Vol.37, No.7, pp.1012-1019, 2008.

[10] Qinong Zhu, Mei Sheng and Le Luo, "The effect of Pb contamination on the microstructure and mechanical properties of SnAg/Cu and SnSb/Cu solder joints in SMT," *Soldering and Surface Mount Technology*, Vol.12, No.3, pp.19-23, 2000.

[11] W.H.Moy, Y.-L.Shen, "On the failure path in shear-tested solder joints," *Microelectronics Reliability,* Vol.47, pp.1300-1305, 2007.

[12] Morris Jr JW, Freer Goldstein JL, Mei Z, "Microstructural influences on the mechanical properties of solder," In: Frear D, Morgan H, Burchett S, Lau J, editors. *The Mechanics of Solder Alloy Interconnects*. New York: Van Nostrand Reinhold, pp.7-41, 1994.

[13] Pang JHL, Ang KH, Shi XQ, Wang ZP, "Mechanical deflection system(MDS) test and methodology for PBGA solder joint reliability," *IEEE Transactions on Advanced Packaging,* Vol.24, pp.507-514, 2001.

[14] Liu XW, Plumbridge WJ, "Damage produced in model solder (Sn-37Pb) joints during thermomechanical cycling," *Journal of Electronic Materials*, Vol.32, pp.278-286, 2003.

[15] Lee JG, Telang A, Subramanian KN, Bieler TR, "Modeling thermo-mechanical fatigue behavior of Sn-Ag solder joints," *Journal of Electronic Materials*, Vol.31,pp.1152-1159, 2002.

[16] Frear DR. "The mechanical behavior of interconnect materials for electronic packaging," *JOM,* Vol. 48, No.5, pp.49-53, 1996.

[17] Kerr M,Chawla N, "Creep deformation behavior of Sn-3.5Ag solder /Cu couple at small length scales," *Acta Materialia*, Vol.52, pp.4527-4535, 2004.

[18] Shen YL, Abell KCR, Garrett SE, "Effects of grain boundary sliding on microstructural evolution and damage accumulation in tin-lead alloys," *Int. Journal of Damage Mechanics* ,Vol.13, pp.225-240, 2004.

[19] Pang JHL, Tan KH, Shi X, Wang ZP, "Thermal cycling aging effects on microstructural and mechanical properties of a single PBGA solder joint specimen," *IEEE Trans Comp Packag Technol,* Vol.24, pp.10-15, 2001

[20] Shen Y-L, Chawla N, Ege ES, Deng X, "Deformation analysis of lap-shear testing of solder joints", *Acta Materialia*, Vol.53, pp.2633-2642, 2005.

[21] Ochoa F, Williams J.J, Chawla N, "Effects of cooling rate on the microstructure and tensile behavior of a Sn-3.5 % wt.Ag solder," *Journal of Electronic Materials,* Vol.32, pp.1414-1420, 2003.

[22] J.Varghese, A. Dasgupta, "Failure site transition during drop testing of printed wiring assemblies," *ASME*, pp 1-4, 2005.

[23] F.X.Che and John H.L.Pang, "Modeling board-level four-point bend fatigue and impact drop tests," *Electronic Components and Technology Conference*, pp.443-448, 2006.

[24] Pradeep Lall, Sandeep Gupte, Prakriti Choudhary, Jeff Suhling, "Solder-joint reliability in electronics under shock and vibration using explicit finite-element sub-modeling," *Electronic Components and Technology Conference*,

pp.428-435, 2006.

[25] Junfeng Zhao and Luke J Garner, "Mechanical modeling and analysis of board level drop test of electronic package," *Electronic Components and Technology Conference*, pp.436-442, 2006.

[26] Masazumi Amagai, Yoshitaka Toyoda, Tsukasa Ohnishi, Satoru Akita, "High Drop Test Reliability: Lead-free Solders," *Electronic Components and Technology Conference*, pp.1304-1309, 2004.

[27] Ahmer Syed, Wei Lin, Eun-Sook Sohn, and Se-Woong Cha, "Plastic Deformation and Life Prediction of Solder Joints for Mechanical Shock and Drop/Impact Loading Conditions," *Electronic Components and Technology Conference*, pp.507-514, 2007.

[28] Chang-Lin Yeh, Yi-Shao Lai, Hsiao-Chuan Chang, Tsan-Hsein Chen, "Correlation Between Package-level Ball Impact Test and Board-level Drop Test," *Electronic Packaging Technology Conference*, pp.270-275, 2005.

[29] Chang-Lin Yeh, Yi-Shao Lai, Chin-Li Kao, "Prediction of Board-level Reliability of Chip-scale Packages under Consecutive Drops," *Electronic Packaging Technology Conference*, pp.73-80, 2005.

[30] Mikko Alajoki, Luv Nguyen and Jorma Kivilahti, "Drop Test Reliability of Wafer Level Chip Scale Packages," *Electronic Components and Technology Conference*, pp.637-644, 2005.

[31] E.H.Wong, Y-W.Mai, R.Rajoo, K.T.Tsai, F.Liu, S.K.W.Seah, C-L Yeh, "Micro Impact Characterisation of Solder Joint for Drop Impact Application," *Electronic Components and Technology Conference*, pp.64-71, 2006.

[32] John H.L.Pang and F.X.Che, "Drop Impact Analysis of Sn-Ag-Cu Solder Joints Using Dynamic High-Strain Rate Plastic Strain as the Impact Damage Driving Force," *Electronic Components and Technology Conference*, pp.49-54, 2006.

[33] E.H.Wong, C.S.Selvanayagam, S.K.W.Seah, W.D.Van.Driel, J.F.J.M.Caers, X.J.Zhao, N.Owens, L.C.Tan, D.R.Frear, M.Leoni, Y.-S.Lai, and C.-L.Yeh, "Stress-Strain Characteristics of Tin-Based Solder Alloys for Drop-Impact Modeling," *Journal of Electronic Materials*, Vol 37, No.6, pp.829-836, 2008.

[34] Y.-L.Shen, "Inelastic Deformation," *Course pack*: ME 561 Special Topic, 2008.

[35] A. Hillerborg, M. Modeer and P. E. Petersson, "Analysis of crack formation and crack growth in concrete by means of fracture mechanics and finite elements," *Cement and Concrete Research*, vol.6, pp.773-781, 1976.

[36] S. Chanthery, *M.S. Thesis*, University of New Mexico, 2004

[37] P. Adeva, G. Caruana, O. A. Ruano and M. Torralba, "Microstructure and high temperature mechanical properties of tin," *Materials Science and Engineering* A194, pp.17-23, 1995.

[38] Pradeep Lall, Sameep Gupte, Parkriti Choudhary, and Jeff Suhling, "Solder Joint Reliability in Electronics Under Shock and Vibration Using Explicit Finite-Element Submodeling," *IEEE Transactions on Electronics Packaging Manufacturing*, Vol.30, No.1, pp.74-83, January 2007.

[39] Desmond Y.R.Chong, F.X.Che, L.H.Xu, H.J.Toh, John H.L.Pang, B.S.Xiong, B.K.Lim, "Performance assessment on board-level drop reliability for chip scale packages (fine-pitch BGA)," *Electronic Components and Technology Conference*, pp.356-363, 2006.

[40] Andrew Farris, Jianbiao Pan, Albert Liddicoat, Brian J.Toleno,Dan Maslyk,Donkai Shangguan,Jasbir Bath, Dennis Willie,David A.Geiger , "Drop test reliability of lead-free chip scale packages," *Electronic Components and Technology Conference*, pp.1173-1180, 2008.

[41] Pradeep Lall, Dhananjay R.Panchagade, Prakriti Choudhary, Sameep Gupte, and Jeffrey C.Suhling, "Failure-Envelope Approach to Modeling Shock and Vibration Survivability of Electronic and MEMS Packaging," *IEEE Transactions on Components and Packaging Technologies*, Vol.31, No.1, pp.104-113, March 2008.

[42] Huann-Wu Chiang, Jun-Yuan Chen, Ming-Chuan Chen, Jeffrey C. B. Lee, and Gary Shiau, "Reliability Testing of WLCSP Lead-Free Solder Joints," *Journal of Electronic Materials*, Vol.35, No.5, pp.1032-1040, 2006.

[43] T. T. Mattila and J. K. Kivilahti, "Reliability of Lead-Free Interconnections under Consecutive Thermal and Mechanical Loadings," *Journal of Electronic Materials*, Vol.35, No.2, pp.250-256, 2006.